NASA Contractor Report **178189**



# SAGE II Satellite Data Set Validation

**Geoffrey S. Kent**
**Pi-Huan Wang**

Science and Technology Corporation
Hampton, Virginia 23666

**Contract NAS1-17959**
**November 1986**

National Aeronautics and
Space Administration

**Langley Research Center**
Hampton, Virginia 23665-5225

## FOREWORD

The Science and Technology Corporation (STC) is pleased to submit the final report on NASA Contract NAS1-17959. We are pleased to acknowledge the assistance of M. P. McCormick, L. R. McMaster, and W. P. Chu of NASA, Langley Research Center, who provided many useful discussions on the various aspects of this work.

TABLE OF CONTENTS

TABLE OF CONTENTS (Cont'd)

LIST OF FIGURES

LIST OF FIGURES (cont'd)

LIST OF FIGURES (cont'd)

LIST OF FIGURES (cont'd)

LIST OF FIGURES (cont'd)

LIST OF TABLES

## ABSTRACT

This report presents the results of a validation study of data obtained by the Stratospheric Aerosol and Gas Experiment II satellite experiment (SAGE II). Preliminary SAGE II data have been available for the period October, 1984 to May, 1985. In addition, the results of two correlative experimental measurement series have been studied in detail, as well as climatological data obtained by other techniques, including ground-based and airborne lidar. The study shows the SAGE II data to be of great potential value to studies of the microphysics of stratospheric aerosols, the chemistry of trace gases and stratospheric dynamics. A small number of unidentified errors in the current preliminary data set are described. These will be removed from the next version of the data set which is anticipated to be of archival quality.

# 1. INTRODUCTION

## 1.1 Background

The Stratospheric Aerosol and Gas Experiment II (SAGE II) was launched aboard the Earth Radiation Budget Satellite (ERBS) in October 1984 (McMaster, 1986). It is the fourth in a series of satellite-borne stratospheric aerosol monitoring instruments flown by NASA. The SAGE II instrument is a seven-channel solar radiometer which measures solar ocultation at the chosen wavelengths for 30 events on each day. The specific objectives of the SAGE II experiment are to:

1. map vertical profiles of stratospheric aerosols, ozone, nitrogen dioxide and water vapor with a 1 km vertical resolution and determine high altitude cloud coverage from $80^{o}$N to $80^{o}$S;

2. study the seasonal and global variations in these constituents so as to improve our understanding of the Earth's radiation budget and climate;

3. utilize the measurements to study global circulation, transient stratospheric phenomena (such as volcanic injection) and sources and sinks of the individual species; and

4. utilize the measurements to study the atmospheric chemistry of the gaseous species and the microphysics relating to the aerosols.

Before data from SAGE II or other similar experiments may be used for the scientific objectives listed above, it is necessary that they undergo a

validation process. During this process, the data are compared with preexisting models of stratospheric aerosols and gaseous constituents, as well as compared with correlative data sets obtained by other means. The statistical nature of the data product must be examined both for internal consistency and for external agreement. This report describes work carried out on the available SAGE II and related data sets as part of this validation process.

### 1.2 SAGE II and Associated Data Sets

The basic SAGE II measurement is of solar radiance in the seven channels listed in Table 1.1 (McMaster, 1986; Mauldin et al., 1985) made during the spacecraft sunrise and sunset periods. The location of the measurements is determined by the spacecraft orbit. This provides 15 sunrise and 15 sunset events on each day. On a specific day, the sunrise events occur at approximately the same latitude as do the sunset events, the latitude of the sunrise events normally being different from that of the sunset events. Successive sunrise or sunset events are separated by approximately $24^{\circ}$ of longitude. The event latitudes cycle from one extreme of latitude to another, a cycle covering about $120^{\circ}$ of latitude and taking about 5 weeks to complete. The extremes of latitude vary somewhat with season but lie between about $80^{\circ}$N and $80^{\circ}$S.

In the routine data processing (Chu, 1986), the radiance data are first converted into a slant path transmission. They are then inverted to obtain vertical profiles of the aerosol extinction at each wavelength as well as the concentration of the gaseous constituents. The first step in the inversion

TABLE 1.1. SAGE II. Spectrometer Characteristics (McMaster, 1986).

| Channel Number | Primary Constituent Detected | Center Wavelength (nm) | Bandwidth (nm) |
|---|---|---|---|
| 1 | Aerosol | 1019.7 | 19.6 |
| 2 | $H_2O$ | 935.5 | 20.0 |
| 3 | $O_3$ | 599.9 | 14.5 |
| 4 | Aerosol | 525.0 | 14.8 |
| 5 | $NO_2$, Aerosol | 454.4 | 1.9 |
| 6 | $NO_2$ | 447.5 | 3.2 |
| 7 | Neutral Density, Aerosol | 384.6 | 19.8 |

procedure is to separate the contribution to the slant path transmission from each specie, as well as that due to the molecular atmosphere at each of the 7 wavelength bands. Following this, the individual vertical profiles for each specie is obtained. Separation of contributions from each specie is complex and troublesome since for all channels there is a contribution to the optical depth from not only the main species but also from the other species. When one species has a large signature which extends across a wide wavelength range, as for example occurs when a high altitude cloud is present, there may be considerable uncertainty associated with the inverted product for other species. An estimate of this uncertainty is made along with the inversion and forms part of the data product.

A major part of the total post-launch data validation process is the operation of field experiments in which correlative data are collected on the aerosols and gaseous constituents. These measurements have been made from both ground based and airborne platforms. The former includes lidar measurements; the latter includes balloon and aircraft in situ particle counters and lidar, rocket and balloon-borne ozone measurements and balloon-borne nitrogen dioxide and water vapor measurements. In the present study, we have made use of such measurements, as well as data available from the SAM II satellite and the historic data set available from the SAGE I satellite (McCormick et al., 1979). The present data validation process also involves the screening of the SAGE II data product, both by examination of tables and plots of the inverted data and by actual data use. A final aspect of the data validation is the analysis of associated but not necessarily correlative data sets, collected by many different techniques, to provide a framework or climatology against which the SAGE II product may be assessed.

## 1.3 Data and Validation Status

The process of data validation for SAGE II has been to a large extent an iterative one. Initially, only a small quantity of SAGE II data was available. As a preliminary data product, this contained many errors and omissions of varying significance. The more obvious of these were quickly found by the authors of this report, and co-workers, resulting in new improved versions of the SAGE II data product. The data product on which the majority of the work described in this report is based, covers the SAGE II measurements from October 1984 (launch) to May 1985 and two correlative experiments, one performed in Laramie, Wyoming in November 1984, and a field experiment performed in Alaska in August 1985. It should be noted that the current data set is not final. While, as a result of the feedback process of data validation, this data set is vastly improved as compared to the original verion, some errors and areas of uncertainty still exist. A new corrected version of the data set will be ready in the near future. It is anticipated that this will be acceptable for scientific use and that it will be the first data set with archival status.

In this report, we have not attempted to list the many minor errors found in the initial data product. Some major errors which still exist, e.g., the sunrise-sunset effect which is still present in the current data product, are described. There is also an indepth discussion of analysis of some of the correlative data, notably the aerosol size distribution measurements and comparison with the SAGE II multiwavelength extinction

data. This report also contains the results of scientific analyses of the SAGE II data, associated data sets and related theoretical studies. It should be emphasized that such studies, based on the current preliminary SAGE II data set, are not final. While the qualitative aspects of the results obtained are not expected to be in error, quantitative values will be subject to change when the analyses are repeated on the revised data set.

### 1.4 Tasks and Organization of Report

The statement of work specifies seven task areas. Work has been carried out under each of these areas and this work is reported in sequence in Sections 2 through 8 of this report. The title given to each main section is the same as the work statement for the corresponding task. Although work has been carried out under each task area, the division is not necessarily uniform. This division represents the results of discussions between the contractors and the NASA Technical Monitor as to the work areas requiring major attention. Subsections under each section correspond to separate studies within the task area.

Some of the work carried out has been presented at scientific meetings and a small part has been accepted for publication. That the latter is not larger is attributed to the fact that to date all current analyses of SAGE II data are based, as explained in the previous section, on a preliminary data set. As such, it is not yet suitable for formal publication. Where material has been presented or published, the corresponding abstract or paper is included in the Appendix to the report. To avoid duplication, a brief outline is made in the body of the report and reference is made to the appropriate Appendix.

## 2. TASK 1--INVESTIGATE THE GLOBAL CLIMATOLOGY OF STRATOSPHERIC AEROSOLS, $O_3$, WATER VAPOR AND $NO_2$, INCLUDING SPATIAL AND TEMPORAL VARIABILITY

### 2.1 Stratospheric Aerosol Climatology

As part of the work associated with the validation of SAGE II data, the stratospheric global aerosol climatology from 1979-1985 has been reviewed. This period has included many volcanic eruptions that have affected the stratosphere. The stratospheric aerosol has been intensely studied by ground-based, airborne, and satellite techniques with a resulting increase in our understanding of its climatology. This work has been summarized and presented as an invited review paper at the Symposium on Radiation in the Middle Atmosphere at the IAGA-IAMAP meeting in Prague, Czechoslovakia, held on August 5-17, 1985. A copy of the abstract for this paper is included in this report as Appendix 1 (Kent & McCormick 1985a).

As part of the same study, the aerosol climatology, as shown by SAGE II, has also been examined for compatibility with the results established from SAM II, SAGE I, and airborne lidar. Some of the more detailed results of this study will be shown elsewhere (Sections 2.2 and 7.1); here, it may be noted that the preliminary SAGE II data shows many expected characteristics. The most prominent among these are:

1. the high aerosol concentrations still present in 1984 and 1985, following the eruption of El Chichon in 1982,

2. a decrease in concentration between October 1984 and May 1985 (Limits of SAGE II data currently available for study).

3. A zonal structure to the aerosol concentration similar to that seen after earlier volcanic eruptions (Kent and McCormick, 1984).

## 2.2 Software for SAGE II Global Plots

As part of work carried out under a separate contract (NAS1-17032), software has been developed to enable global maps of SAGE I 1 μm optical depth to be produced. At first sight, this appears to be a relatively simple matter as the satellite data systematically sweeps in location from one extreme of latitude to another. In practice, difficulties arise because of the following:

1. The satellite data points do not fall on a regular grid. Although the longitudinal interval is fairly regular ( ~ $24^{o}$ intervals), the latitude interval varies greatly between high and low latitudes. Moreover, there is a longitudinal shift in data location on successive days.

2. Missing data are not infrequent, either requiring an interpolation routine or resulting in areas of missing data on the final map. The latter almost certainly means that contouring routines cannot be used on the map.

The SAGE I software has been converted for use with the SAGE II data product. The purpose of this conversion was (1) to obtain a useful tool for scientific investigation of global aerosol climatology, and (2) to obtain a display which permits rapid detection and screening of anomalies in the data itself. The algorithm for production of these maps involves the following steps.

1. Selection of a suitable portion of SAGE II data for mapping, e.g., a latitudinal sweep between chosen dates--this should be either a sunrise or a sunset sequence.

2. Production of the variable to be plotted at each data location (in the present case, 1 μm optical depth).

3. Determination of the limits of the latitude sweep and the locations of any missing data within that sweep.

4. Interpolation of missing data, provided the data gaps do not exceed a certain predetermined size. The interpolation involves the data points neighboring the data gaps.

5. Interpolation of the filled data sequence to a $1^{o}$ x $1^{o}$ global latitude-longitude grid. This is a fairly complex procedure involving definition of quadrilateral data cells within the SAGE II data product, followed by a projection onto a retangular grid and finally a standard interpolation to the $1^{o}$ unit cell structure.

6. Use of the $1^{o}$ x $1^{o}$ data matrix to produce either a shaded or a contoured data product, or one containing both. The data matrix may also be used to produce color-coded maps.

User friendly control procedures have been written for use with the above programming sequence. Although these are, at present, confined to the production of 1 μm optical depth maps, their extension to other data products

appears to be a relatively simple matter. This could include, for example, optical depth and extinction at other wavelengths, or water vapor and ozone concentrations. The procedure then becomes a very useful and powerful tool for displaying and screening the data product.

An example of the data product is shown in Figure 2.1. This figure shows the 1 μm optical depth, measured from 2 km above the tropopause, for the period October 24 - November 20, 1984. The data shown are for sunset events only.

Six levels of shading are available and contours have been added to delineate the shaded regions. The high latitude resolution and quality of the data product are apparent. In scientific terms, this figure shows the very strong banded structure apparent in the stratospheric aerosol. At this time, the aerosol is a well-dispersed and partially decayed aerosol derived mainly from the El Chichon eruptions of April/May, 1982. The zonal structure has been observed previously both in early post-volcanic aerosol (during 1981) and in pre-volcanic aerosol (during 1979).

### 2.3 Analyses of Error Bars on 1 μm Aerosol Data

An important SAGE II data product is the error bar which is supplied for each data point. Much subsequent scientific analysis will involve screening the data using not only the quality factor which is representative of a complete vertical profile, but also the individual error bars for each altitude. As part of our examination of the preliminary data set, an analysis was made of the error bars associated with the SAGE II 1 μm

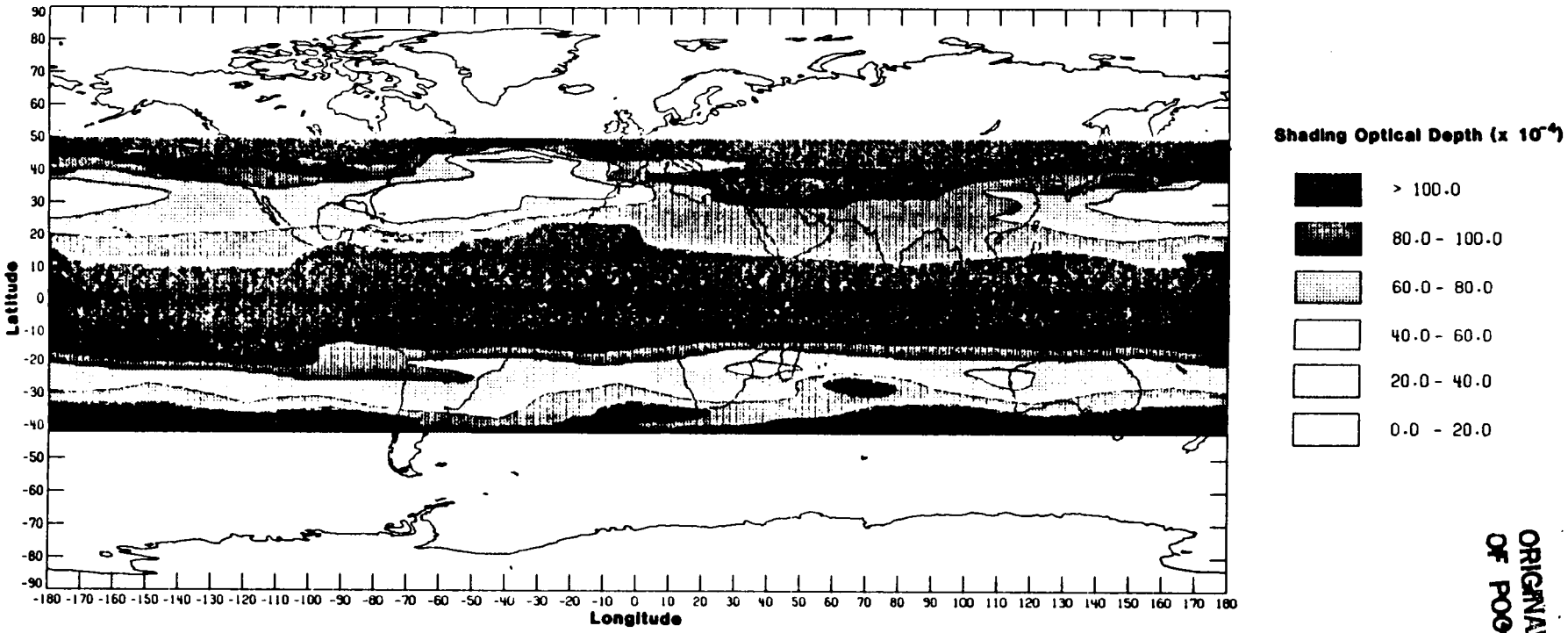


Figure 2.1. SAGE II measurements of 1 μm optical depth from 2 km above the tropopause, October 24 - November 20, 1984.

extinction data. Two aspects of the data were examined: (1) Did the error bars appear to give a reasonable representation of the statistical fluctuations in the data set and (2) How did the SAGE II error bars compare with those given in the SAGE I and SAM II data sets? Programs were written for all three satellite data sets which (1) divided the measured data in $10^{o}$ latitude bands and (2) calculated the mean 1 μm extinction and extinction ratios within each band, the root mean square variation of these quantities within the band, and the mean error bar. Assuming little or no systematic error exists within the data set, the error bar is expected to be less than, or approximately equal to, the rms variation within the data set. This follows from the fact that the latter includes both data errors and actual geophysical variations. The expected inequality is not found to be always true for either the SAGE I or the SAGE II data set. For the SAM II data set, which is inverted by a different scheme, the rule is generally true.

Figure 2.2 shows typical results for SAGE I and SAGE II taken for identical months (in different years) and for the same latitude band. The extinction ratio profiles for the two periods are significantly different below an altitude of 25 km, due to the presence of aerosol from the eruption of El Chichon in 1982, which produced an increased extinction ratio as shown in Figure 2.2(b). There is also a significant difference in the extinction ratios above 25 km which is not due to the volcano. Part of this difference may be due to the use of a slightly incorrect molecular atmosphere for SAGE I. (W. Chu, 1986 private communication.)

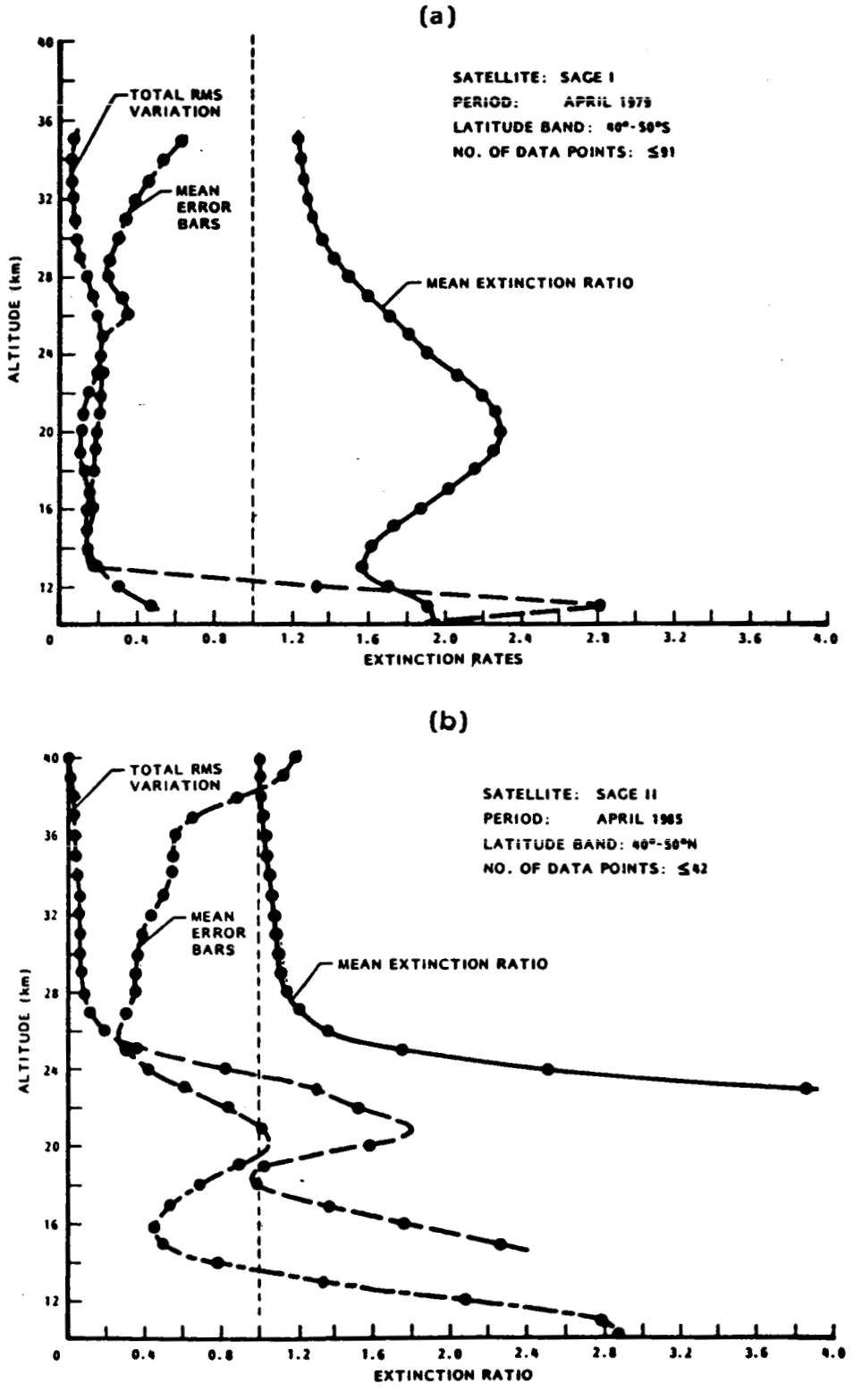


Figure 2.2. Altitude variation of mean 1 μm extinction ratio, extinction ratio error and RMS variation within a 10° latitude band for (a) SAGE I data, April 1979; (b) SAGE II data, April 1985. Both data sets are for latitude bands 40° - 50°N.

Below 25 km, the mean error bar for both SAGE I and SAGE II data is of the same order or less than the observed rms variation within the data set and no serious discrepancy exists. Above 25 km, the error bars increase rapidly for both satellite data sets; in contrast, the rms variation decreases. A major part of this behavior difference is due to the introduction of vertical smoothing into the data inversion process when the extinction falls below a certain predetermined value. This smoothing is carried out over a vertical height interval of 5 km; the error bars are not smoothed and would thus be expected to be larger (relative to those at a lower altitude) by a factor of $\sqrt{5}$. This factor is probably sufficient to account for the relative growth in the error bars (for both SAGE I and SAGE II) up to an altitude of about 30 km. Above this altitude the error bars appear to be an overgenerous estimate of the errors within the data set. In the case of the SAM II where a different inversion scheme was used, no comparable height variation in the significance of the error bar was found. This vertical variation in the significance of the SAGE I and SAGE II error bars indicates that care must be taken in any analysis that depends upon them, particularly as it relates to the altitude range 20-30 km.

## 2.4 Ozone and $NO_2$ Diurnal Variations

In this section, we report the results of validating the available preliminary SAGE II data set in terms of examining the diurnal variability of the mesospheric $O_3$ and stratospheric $NO_2$. There are three occasions in the first eight-month sampling period of the SAGE II instrument at which the sunrise and sunset measurements cross each other at certain latitudes. Figure 2.3 shows the location and the time of the occurrence of these

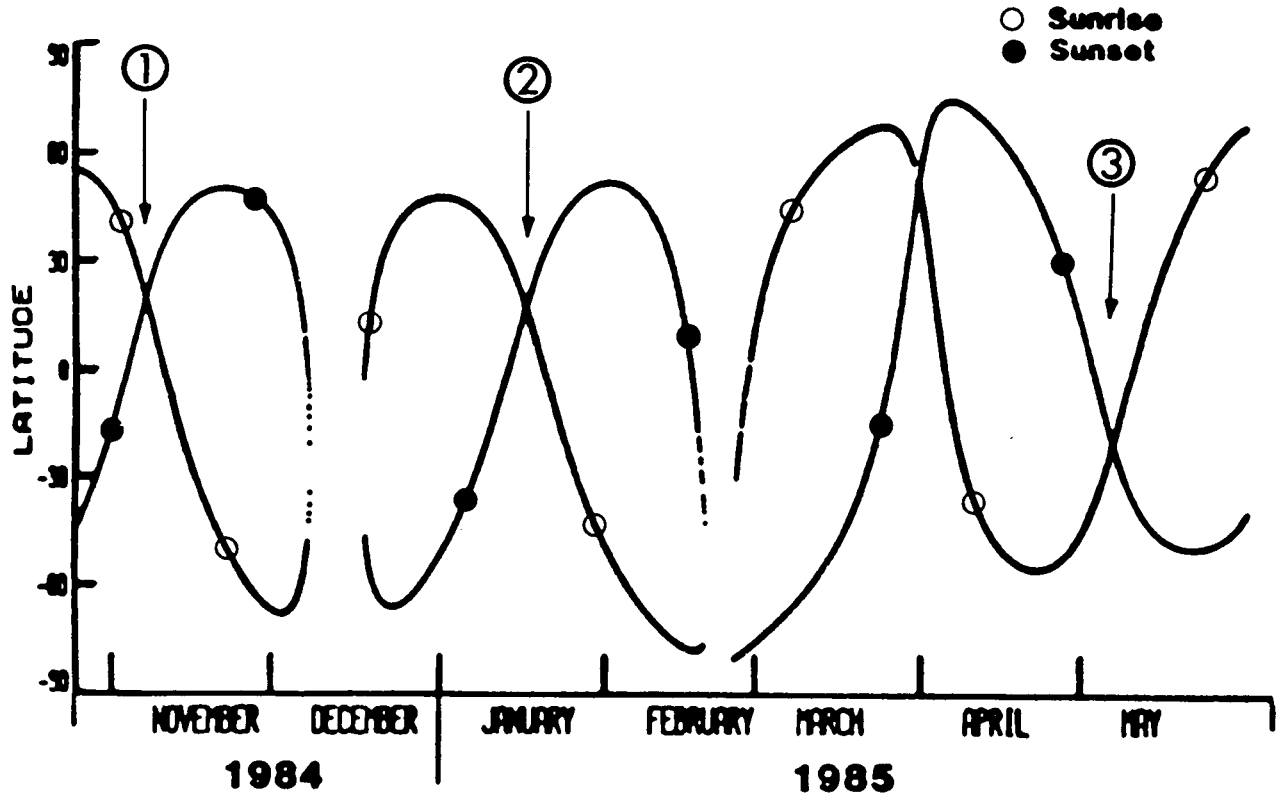


Figure 2.3. Latitudinal coverage of SAGE II measurements, October 1984 to May 1985. The circled numbers show the three occasions when sunrises and sunsets were observed at the same latitudes.

occasions (the circled numbers). Figure 2.4 shows the averaged profile for the sunrise events (solid line), and also that of the sunset events (dashed line) for such an occasion which happened in May 1985. Only those sunrise and sunset measurements for which the differences in latitude are less than $5^{o}$ are included in the analysis. As indicated in Figure 2.4, the averaged sunrise profiles show about a 6% higher $O_3$ concentration than that of the sunset profiles in the altitude range between the lower limit of the figure (30 km) and approximately 60 km. Since in the stratosphere the $O_3$ diurnal variation is negligibly small (e.g., Wang et al., 1980), Figure 2.4 indicates a bias in the SAGE II $O_3$ data set.

The corresponding averaged sunrise and sunset profiles for $NO_2$ are displayed in Figure 2.5. The cross behavior of the $NO_2$ profiles at altitudes ~25 km and 37 km is less anticipated and is difficult to interpret. In general, the stratospheric photochemistry suggests a similar vertical distribution of $NO_2$ concentration with the sunset $NO_2$ higher than that of sunrise (Chu and McCormick, 1986). As a result, further investigation on the preliminary SAGE II $NO_2$ data set is required.

Because of the unexpected behavior difference between the sunrise and sunset $O_3$ and $NO_2$, derived from preliminary SAGE II data set, this type of data comparison has been extended to all the other SAGE II measurements, including $H_2O$ and the four aerosol channels. The results of this comparison are given in Figures 2.6a to e, respectively. As can be seen, the results also indicate a systematic bias with the sunrise measurements at a higher altitude than the corresponding sunset values.

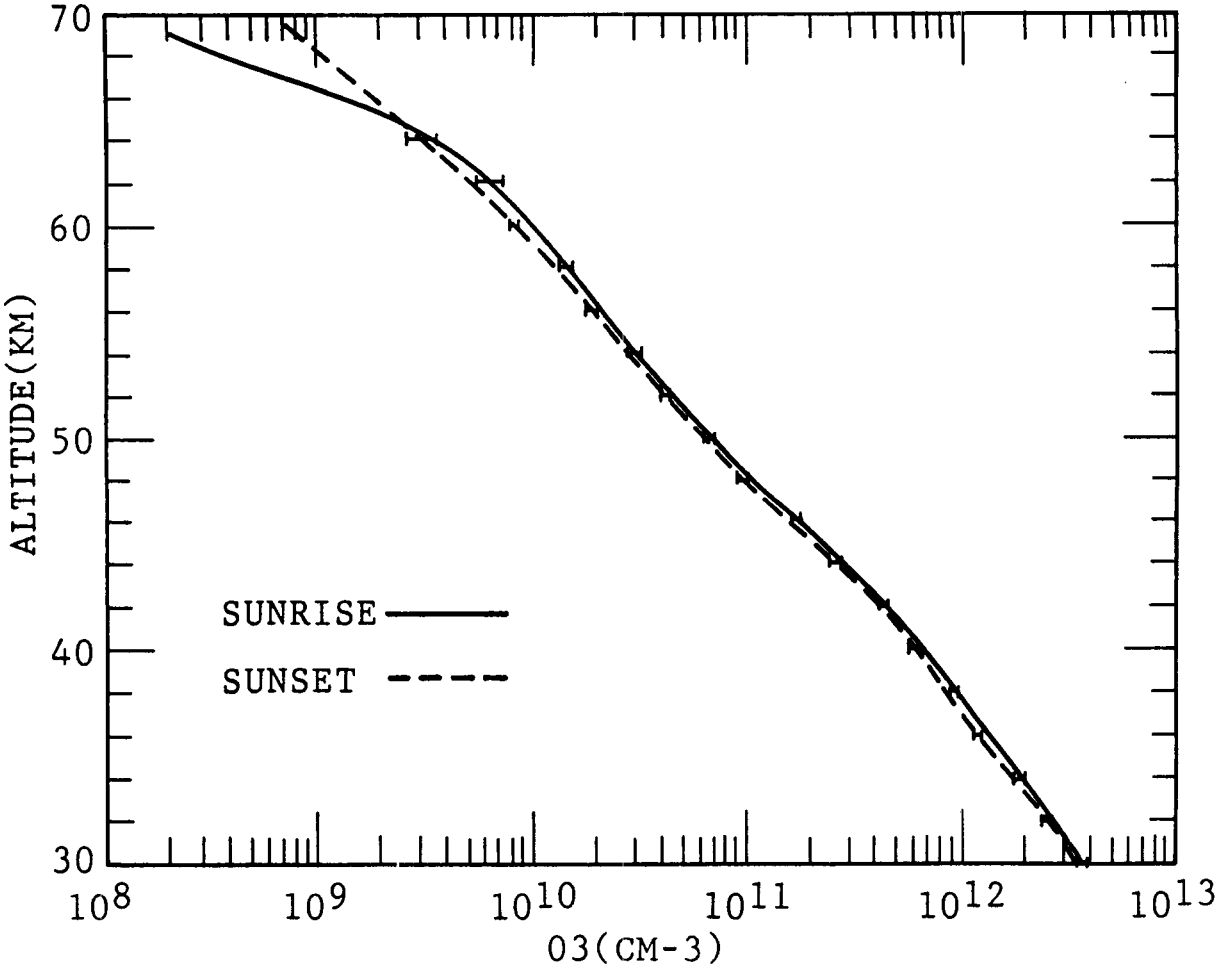


Figure 2.4. Comparison of preliminary SAGE II ozone profiles for sunrise and sunset measurements. Data are for May 1985 and averaged over several events.

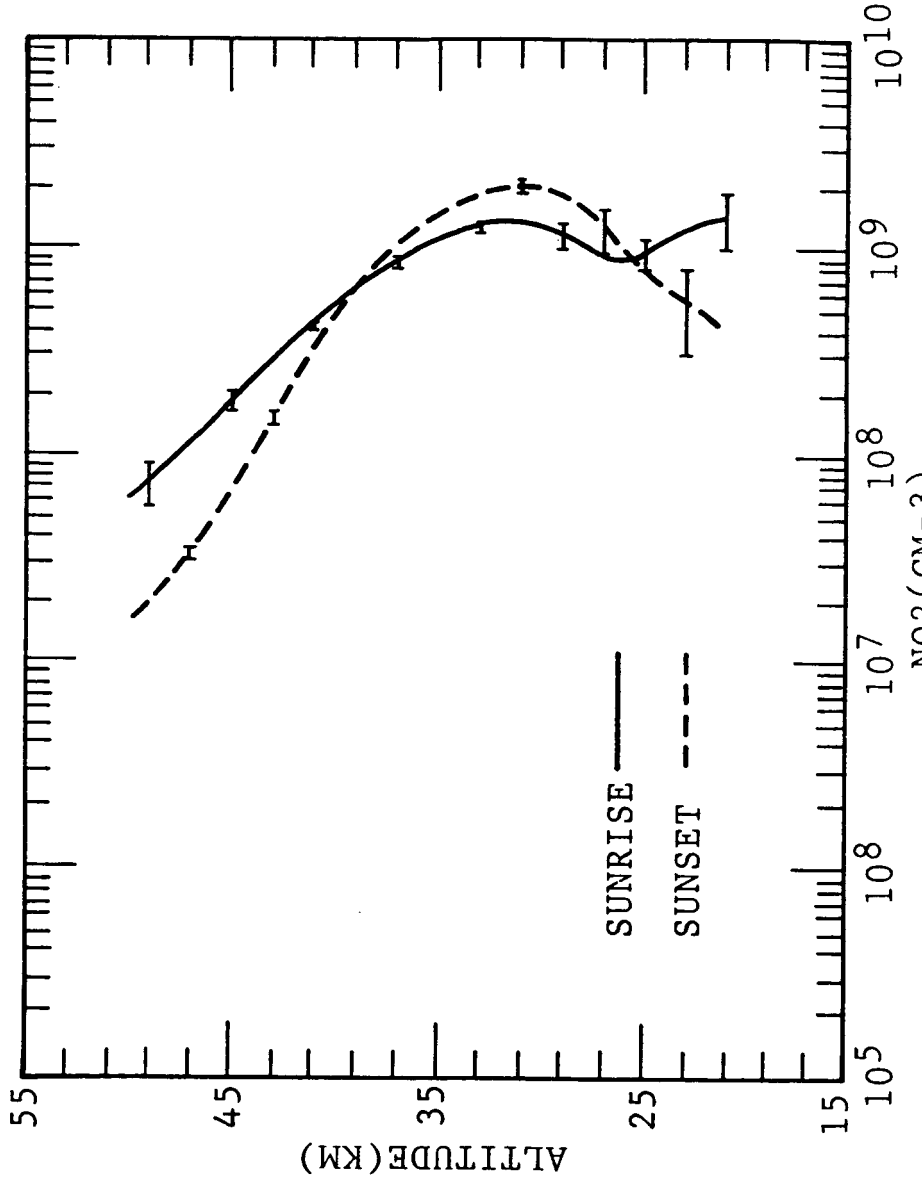


Figure 2.5. Comparison of preliminary SAGE II $NO_2$ profiles for sunrise and sunset measurements. Data are for May 1985 and averaged over several events.

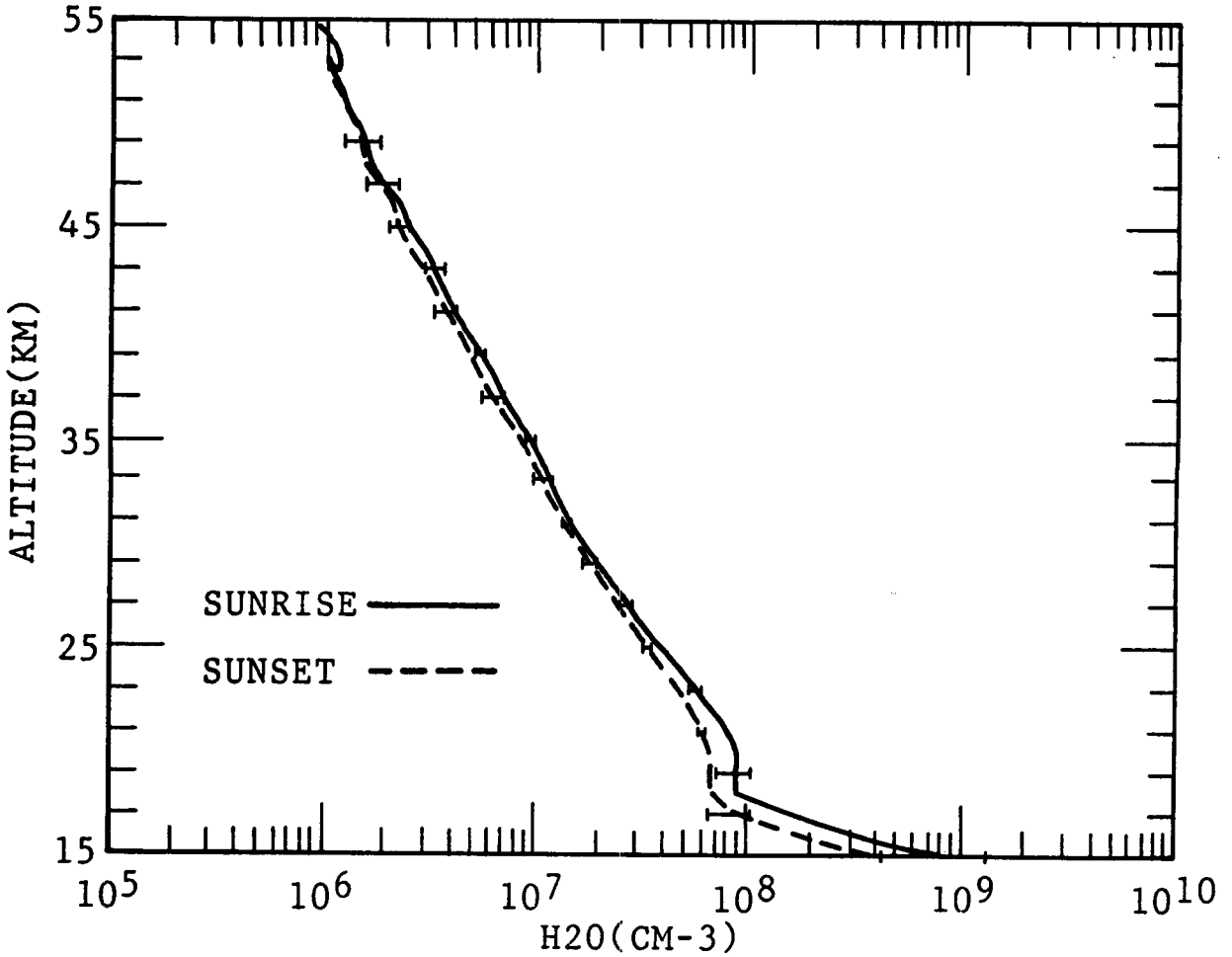


Figure 2.6(a). Comparison of preliminary SAGE II $H_2O$ profiles for sunrise and sunset measurements. Data are for May 1985 and averaged over several events.

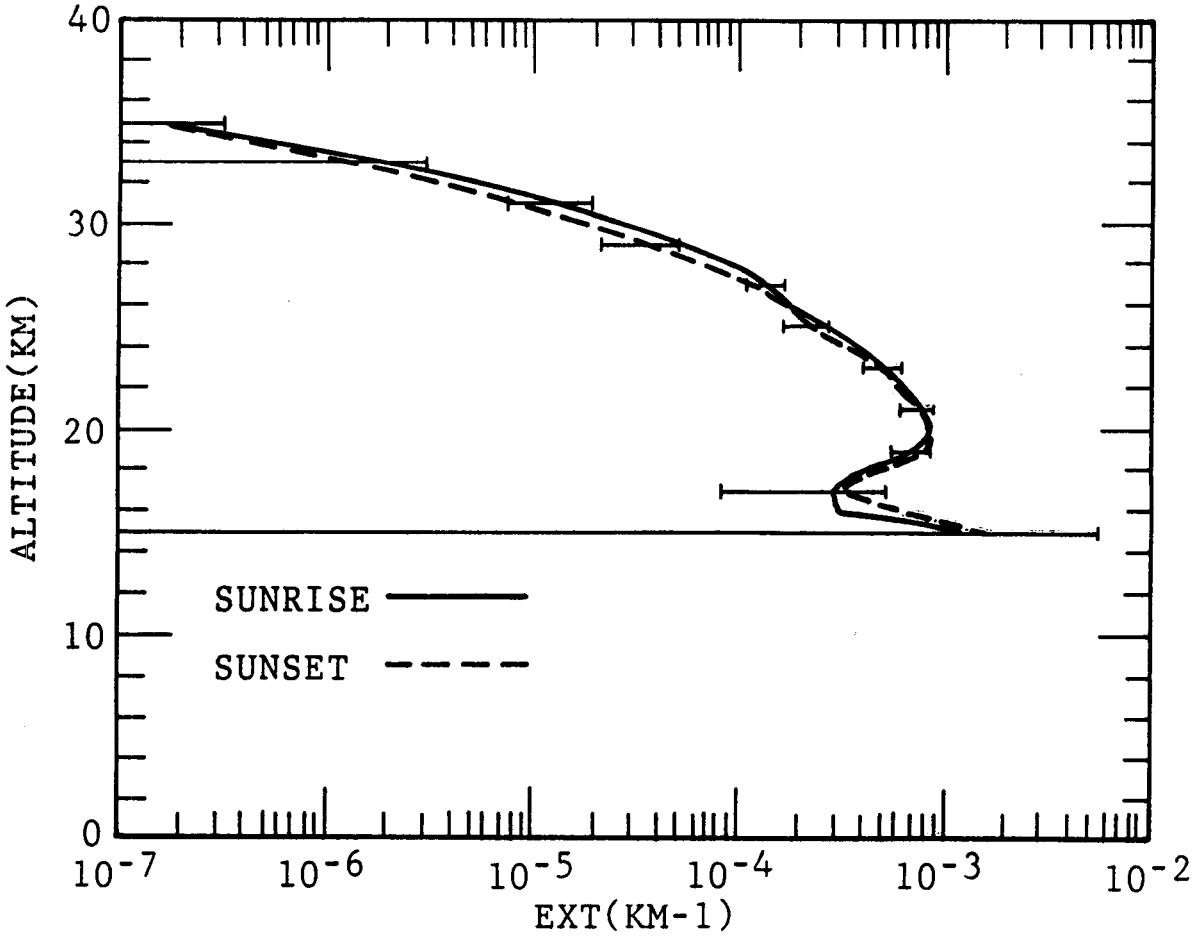


Figure 2.6(b). Comparison of preliminary SAGE II 1.02 μm aerosol extinction profiles for sunrise and sunset measurements. Data are for May 1985 and averaged over several events.

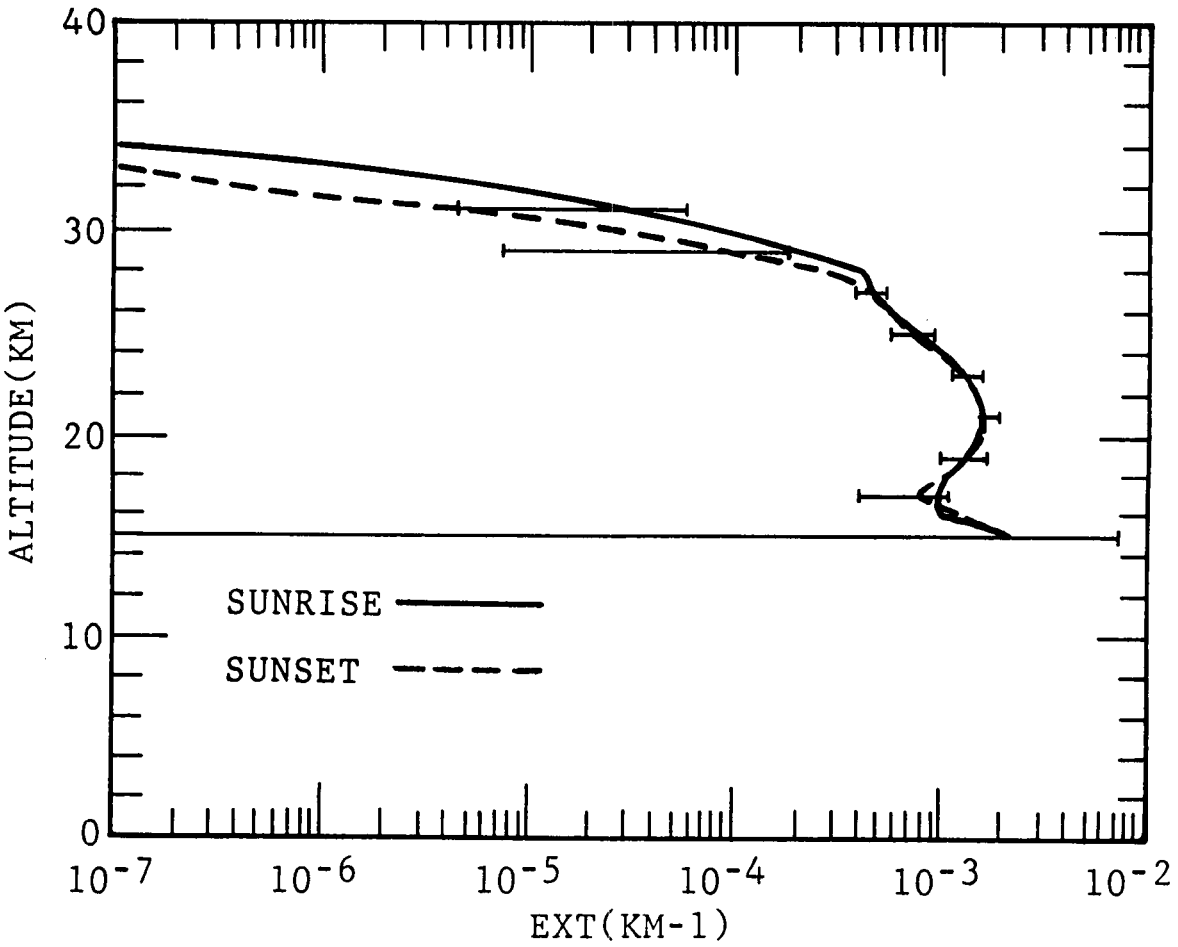


Figure 2.6(c). Comparison of preliminary SAGE II 0.525 μm aerosol extinction profiles for sunrise and sunset measurements. Data are for May 1985 and averaged over several events.

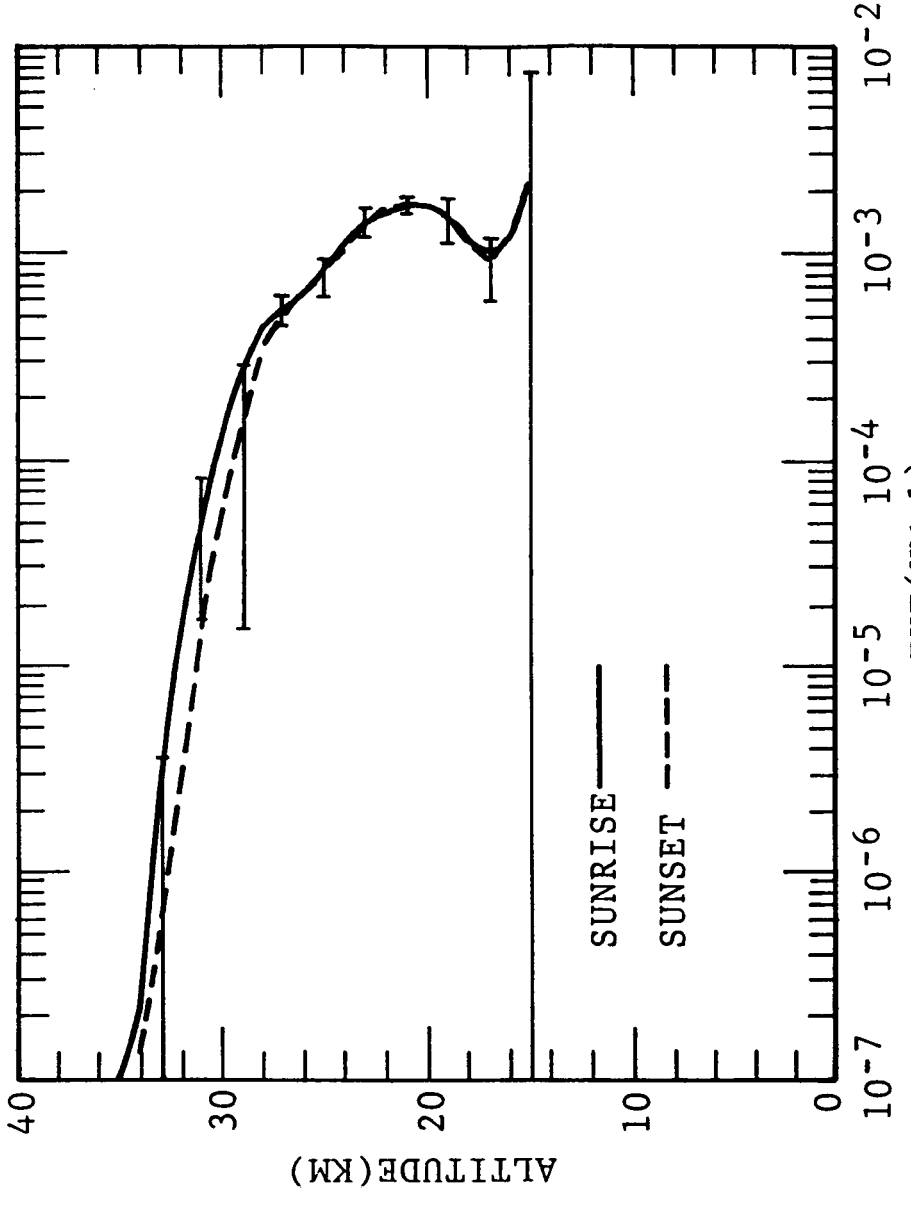


Figure 2.6(d). Comparison of preliminary SAGE II 0.45 μm aerosol extinction profiles for sunrise and sunset measurements. Data are for May 1985 and averaged over several events.

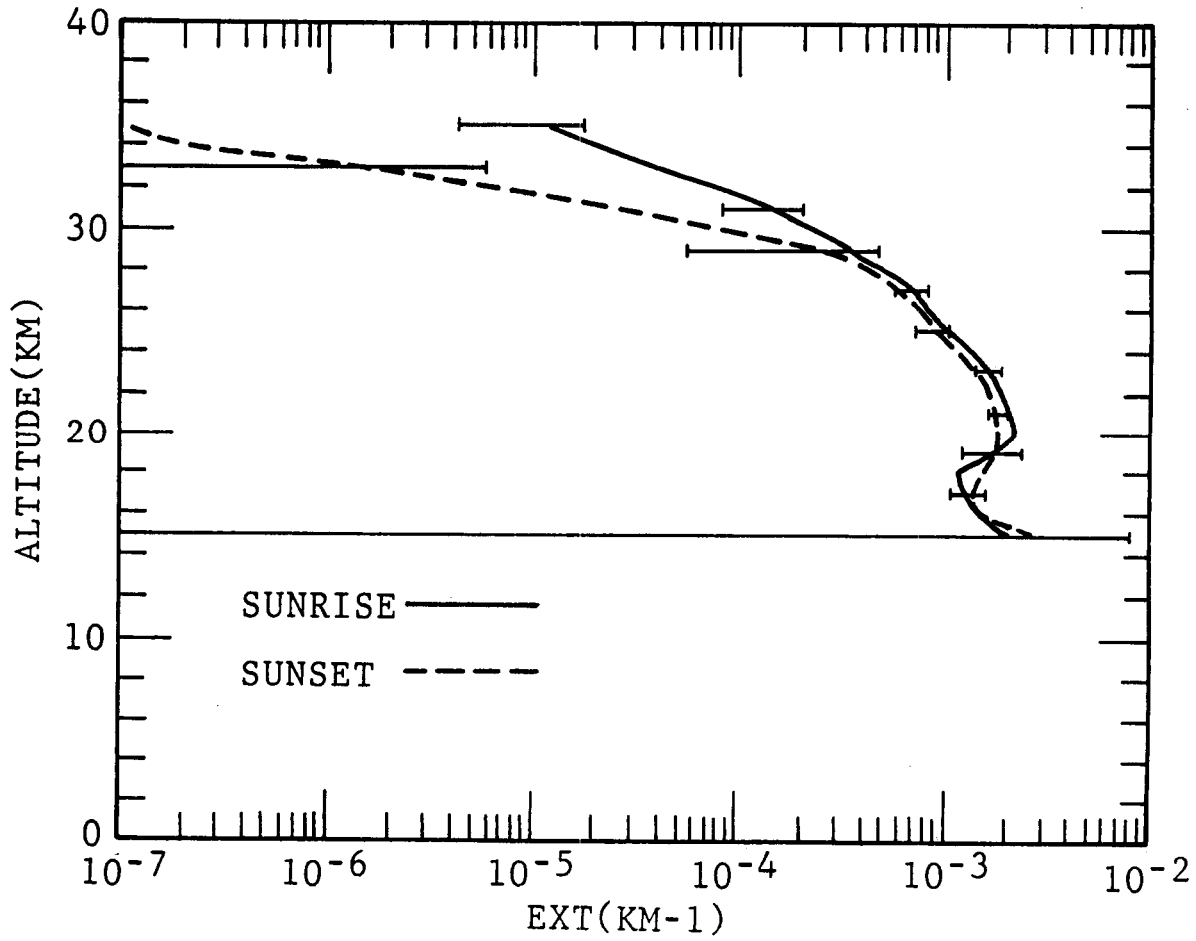


Figure 2.6(e). Comparison of preliminary SAGE II 0.385 μm aerosol extinction profiles for sunrise and sunset measurements. Data are for May 1985 and averaged over several events.

In order to further confirm the above findings in this preliminary May, 1985 SAGE II data set, the profiles obtained at the other two adjacent sunrise and sunset crossings, as shown in Figure 2.3, have also been examined. Again, a similar unexpected behavior of the sunrise and sunset profiles of this preliminary SAGE II measurement is shown in the averaged profiles for these two occasions.

Relevant to the above findings of the bias in the current SAGE II data set, G. Yue of NASA-LaRC and M. T. Osborn of SASC Technologies Inc. have found, independently, that good agreement exists between the 1 μm aerosol extinction profiles of individual SAGE II sunset events and SAM II events that occurred close together in space and time. This is not true for similarly collected SAGE II sunrise and SAM II observations. In their analyses, the SAGE II sunrise 1 μm aerosol extinction profiles are systematically shifted to a higher altitude as compared to those for SAM II. Thus, from their results, and that of the sunrise and sunset analysis mentioned earlier, it is most likely that the bias exists in the preliminary SAGE II sunrise data set.

## 2.5 Anomalous Values of the 0.525/1.0 μm Extinction ratio

As part of the development of an aerosol climatology for the stratosphere and upper troposphere, a study has been made of the wavelength extinction ratio (Extinction ( $\lambda$ = 0.525 μm)/Extinction ( $\lambda$ = 1.02 μm)). This ratio is related to the particle size distribution (see Section 3.1.1.). For small particles such as exist in the statosphere, a ratio in the range 2-5 is to be expected. For cloud particles, which are much larger, the ratio should

be about unity. It is very difficult to construct a realistic particle size distribution for which this ratio is substantially less than unity, although values slightly less than unity are possible (Yue, Private Communication, 1986). In the current study, SAGE II aerosol data have been divided into $20^{o}$ latitude bands and then binned, according to altitude from 0 to 30 km, and according to 1 μm extinction ratio from 0.01 and 1000.0. The data have been filtered to remove unreliable data points using both the quality factor supplied with the inverted profiles, as well as individual error bars at each altitude. Most of the 0.525 μm/1.02 μm extinction ratio values are as expected, but some anomalies have appeared. The results may be summarized as follows:

1. In the stratosphere, most wavelength extinction ratio values lie between 2 and 6; the higher values, associated with smaller particles, occur at the greatest altitudes.

2. In the free troposphere, more than one aerosol mode is apparent.

   a. Cloud Mode. Wavelength extinction ratio values are close to unity as expected.

   b. Coarse Aerosol Mode (Northern hemisphere). Wavelength extinction ratio values are about 2.

   c. Fine Aerosol Mode (Southern hemisphere). Wavelength extinction ratio values are in the range 3-4.

In addition, however, many values substantially less than unity are found (as low as 0.1). These cannot be true values (private communication

with W. P. Chu). These values probably arise during the inversion process. They only occur at the lower altitudes and are associated with the occurrence of high extinction or optical depth values. Their origin is being examined and it is anticipated that they will be eliminated from the next version of the SAGE II data set.

# 3. TASK 2--INVESTIGATE THE CORRELATION OF STRATOSPHERIC AEROSOLS, $O_3$, WATER VAPOR AND $NO_2$ WITH EACH OTHER AND VARIOUS METEOROLOGICAL PARAMETERS

## 3.1 Modeling the Stratospheric Aerosol Extinctions at 1.0 and 0.45 μm

### 3.1.1 Introduction

Since satellite instruments, such as SAGE II, provide aerosol extinction information at several wavelengths, model calculations are useful in interpreting the observed results. Furthermore, model analyses are also essential to the retrieval of aerosol properties from these multiwavelength extinction measurements (e.g., Yue and Deepak, 1983; see also Section 6.1). More specifically, one needs to know clearly the dependence of the multiwavelength extinction on the aerosol properties including aerosol size distribution, number concentration, refractive index, etc.

In the stratosphere, several different models of the aerosol size distribution have been introduced (e.g., Russell et al., 1981). Perhaps the most widely used one is the log-normal representation introduced by Pinnick et al. (1976) which is given by

$$n(r) = \frac{N_o}{\sqrt{2\pi}\ \ell n\sigma}\ \frac{1}{r}\ \exp\left[\frac{\ell n^2(r/r_g)}{2\ell n^2\sigma}\right] \qquad (3.1)$$

where $n(r)$ is the number of particles per $cm^3$ for particles whose radii are between r and r + dr, $N_o$ is the total number concentrations ($cm^{-3}$), $\sigma$ is the width of the log normal curve, and $r_g$ is the mode radius. The values 1.86 and 0.0725 μm have been used commonly in the literature for $\sigma$ and $r_g$,

respectively. The aerosol refractive index, on the other hand, depends on the composition of the sulfate droplets (Gmitro and Vermeulen, 1964). Furthermore, it is also temperature dependent, following the Lorentz-Lorenz relationship (Longhurst, 1964). For example, the value 1.43 corresponds to the composition of 75% of $H_2SO_4$ and 25% of $H_2O$ at about 218°K (Pinnick et al., 1976).

For stratospheric sulfate droplets, the particles will absorb (or evaporate) water rapidly in response to changes in the ambient temperature such that the equilibrium will be reestablished between the environmental water vapor and the vapor pressure under the new composition of the sulfate droplets. The net result is a change in both the composition and the size of the particles (e.g., Steele and Hamill, 1981).

Recently, Steele and Hamill (1981) have developed a theoretical model for determining the effect of changes in temperature and water vapor on the aerosol particle size. In addition, this model has been applied in conjunction with the Mie scattering theory to determine the dependence of the aerosol extinction at 1.0 μm and the aerosol backscatter at 0.6943 μm on the temperature and humidity in the stratosphere. The log-normal size distribution given by Eq. (3.1) is used in the calculation of aerosol optical properties with $N_o = 10\ cm^{-3}$, $\sigma = 1.86$ and $r_g = 0.0725$ μm. They have further extended their model to investigate the formation of Polar Stratospheric Clouds (PSCs) based on SAM II 1.0 μm extinction observations (Steele et al., 1984).

On the other hand, Yue and Deepak (1983) have developed an effective method for retrieval of stratospheric aerosol size from satellite extinction

measurements at two wavelengths, e.g., 1.0 μm and 0.45 μm. This method has been applied to the aerosol extinction data set derived from the SAGE I measurements (Yue and Deepak, 1984). The development of their method is mainly based on some observed stratospheric features. More specifically, it is assumed that the overall stratospheric temperature and the aerosol particle composition ($W_S$, weight percentage of $H_2SO_4$) and the width of the log-normal curve are 200°K, 75%, and 1.86, respectively. It should be noted that, with the above specified values of these relevant parameters, the interpretation of the different retrieved aerosol sizes would be due to the different gaseous concentrations of ambient water vapor and the mass content of sulphuric acid in the droplet according to the theoretical model of Steele and Hamill (1981). It is important to keep in mind that, in their model, the aerosol droplets are assumed to be in equilibrium with respect to water vapor. The condition for droplets to be in equilibrium with respect to sulphuric acid is not necessary. This is because the time taken for the droplet to undergo a mass increase of 1/e by water absorption is of the order of seconds, whereas it is at least $10^7$ times larger for the sulphuric acid absorption. Thus, the growth by sulphuric acid absorption becomes important only for processes occurring over long time periods. Furthermore, since the vapor pressure of water over a flat solution of a given solute weight percentage ($W_S$) is a function of temperature only, and since the Kelvin effect in the vapor pressure is important only for very small aerosol particles, all the droplets would be characterized by a specific $W_S$ if they are at the same ambient temperature and water vapor concentration. This

implies that a large particle would contain more sulphuric acid for a given ambient water vapor concentration (W).

As mentioned earlier, Steele and Hamill (1981) have used $\sigma$ = 1.86 and $r_g$ = 0.0725 μm in their calculation of the aeorsol extinction at 1 μm. These constants are also introduced into their study of the formation of Polar Stratospheric Clouds. Yue and Deepak (1984) have assumed T = 200°K, W = 75%, and $\sigma$ = 1.86 in their development of the aerosol size retrieval method from measurements at two wavelengths. In reality, however, the stratospheric temperature may have a range from 185°K to 230°K. Similarly, the values of $\sigma$ and $r_g$ may change from place to place and time to time. For example, a mode radius $r_g$ of 0.097 μm and a spread $\sigma$ of 2.02 are considered to be appropriate for the stratosphere following a moderate volcanic event (Chu and McCormick, 1979). Furthermore, in the free troposphere, a value for $\sigma$ of 2.985 is considered appropriate for background aerosol (McClatchey et al., 1980).

In this section, we shall examine the variations of aerosol extinctions at 1.0 μm and 0.45 μm for different values of $\sigma$ and $r_g$ at various ambient temperatures and water vapor. In addition, this study also examines the dependence of the aerosol size on the extinction ratio (0.45 μm to 1.0 μm) under various conditions of atmospheric temperature, water vapor, and the width of the aerosol size distribution ($\sigma$) values. It serves as a sensitivity analysis for retrieval studies of the stratospheric aerosol size distributions using SAGE II multiwavelength aerosol extinctions. As shown in Section 6.1, the retrieved aerosol size distributions from SAGE II measurements can be further used for SAGE II data validation purposes.

### 3.1.2 Computation and results

Since the intention of this analysis is to examine the sensitivities of the calculated aerosol extinction at 1.0 μm and 0.45 μm wavelengths, at given temperatures, with respect to changes in water vapor concentration and aerosol size distribution, consideration of the influence of dynamics is not necessary. In the analysis, the theoretical model developed by Steele and Hamill (1981) is employed for computation. The log-normal representation of Eq. 3.1 is used to determine the aerosol optical properties according to the Mie scattering theory. In addition, we discuss only the case of supercooled droplets at sufficient low temperature, although Steele and Hamill (1981) have concluded that, in the case of PSCs, the particles are more likely to be frozen ones.

Figures 3.1a to 3.1c show the calculated results of aerosol extinction at 1.0 μm for fixed $\sigma$ values of 1.674, 1.86, and 2.064, respectively. The value 1.86 is the most widely used value for describing the background stratospheric aerosol. The lower and higher values of $\sigma$ differ from this value by -10% and +10%, respectively. For each fixed $\sigma$, the extinction is calculated for mode radius ($r_g$) with values 0.05, 0.07, 0.09, 0.11, and 0.13 μm and water vapor mixing ratios of 2, 4, and 6 ppmv. These water vapor concentrations correspond to the vapor pressure of $2 \times 10^{-4}$, $4 \times 10^{-4}$, and $6 \times 10^{-4}$ mb, respectively, at the 100 mb atmospheric pressure level. Figures 3.1a to 3.1c show many interesting features. First of all, the extinction for temperatures greater than about 210°K is not sensitive to changes in ambient water vapor pressure but is to the mode radius ($r_g$). This condition

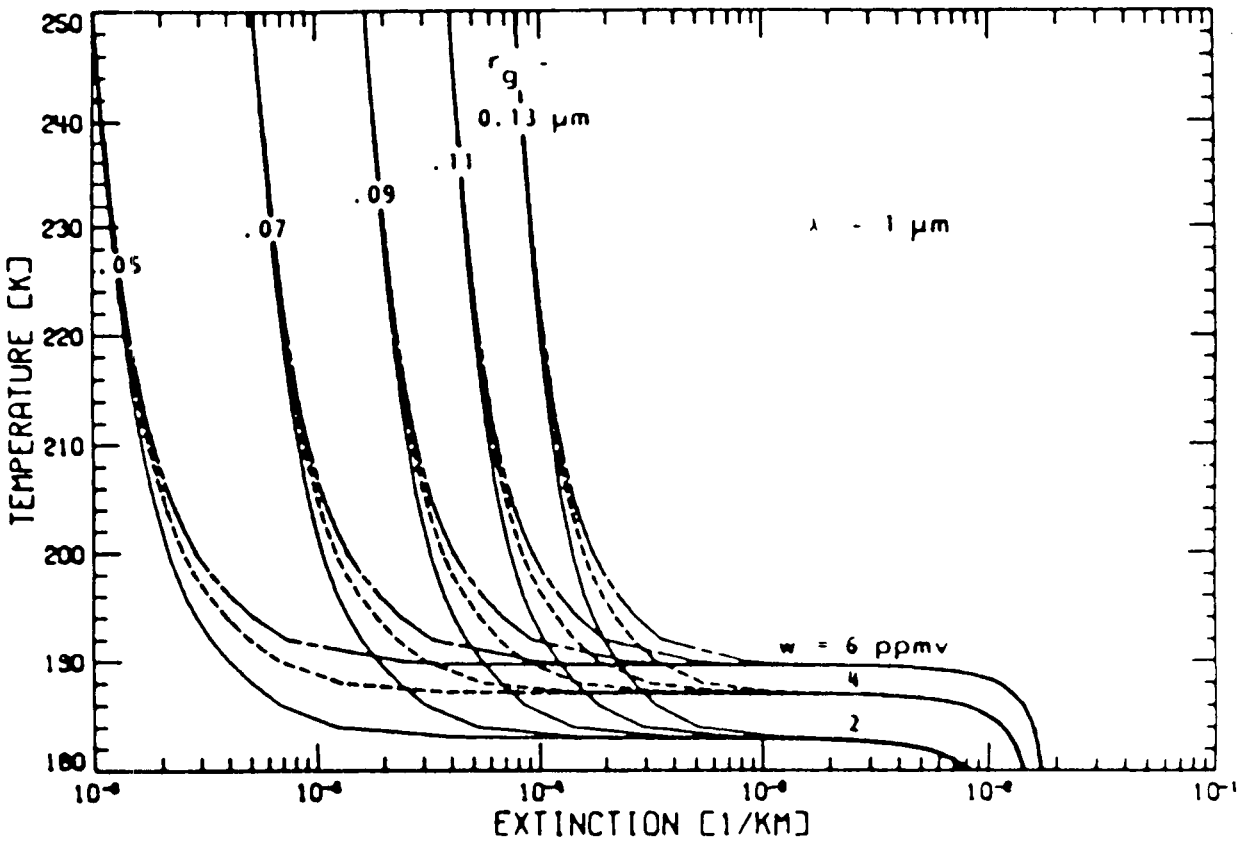


Figure 3.1a. The aerosol extinction at 1 μm as a function of temperature for water vapor mixing ratios of 2, 4, and 6 ppmv at 100 mb for mode radius $r_g$ = 0.05, 0.07, 0.09, 0.11, and 0.13 μm, with fixed values of $\sigma$ in the lognormal aerosol size distribution: (a) $\sigma$ = 1.674.

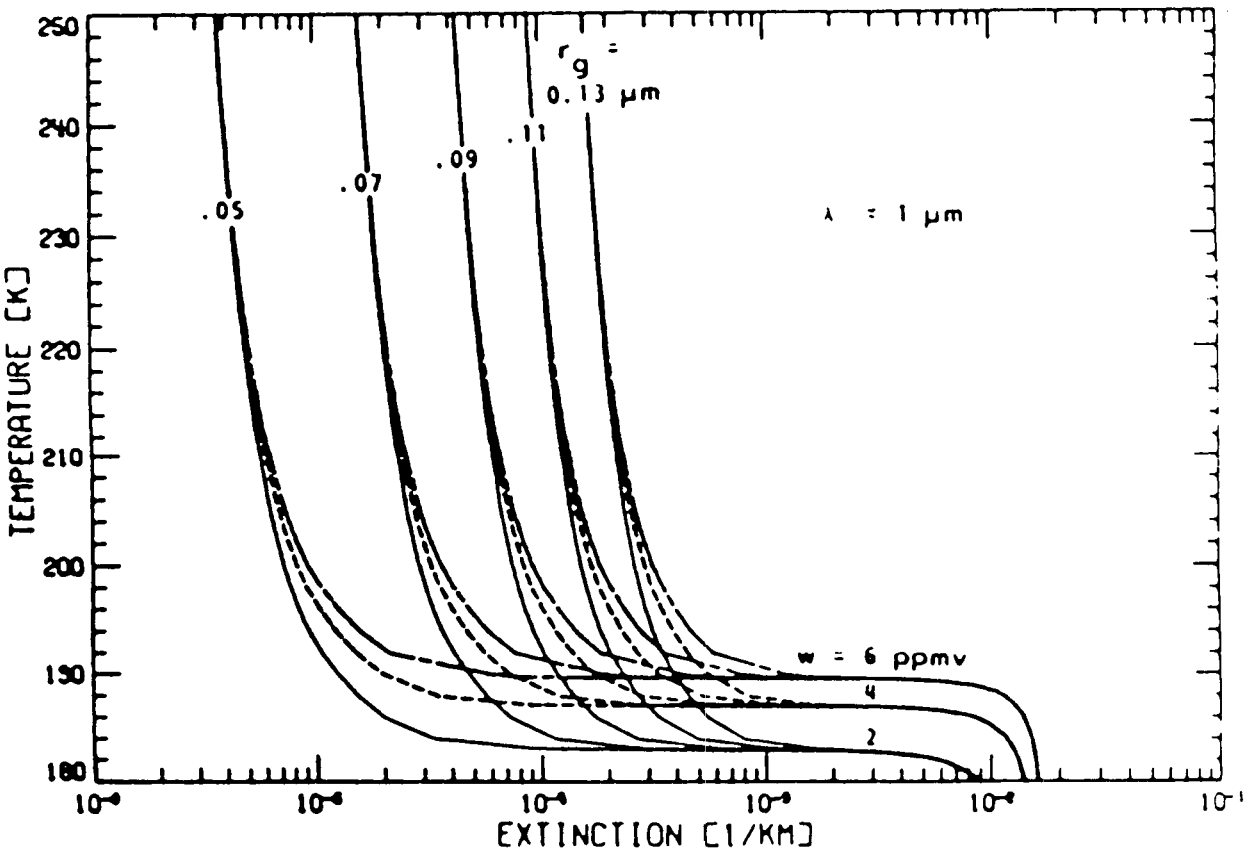


Figure 3.1b. The aerosol extinction at 1 μm as a function of temperature for water vapor mixing ratios of 2, 4, and 6 ppmv at 100 mb for mode radius $r_g$ = 0.05, 0.07, 0.09, 0.11, and 0.13 μm, with fixed values of σ in the lognormal aerosol size distribution: (b) σ = 1.86.

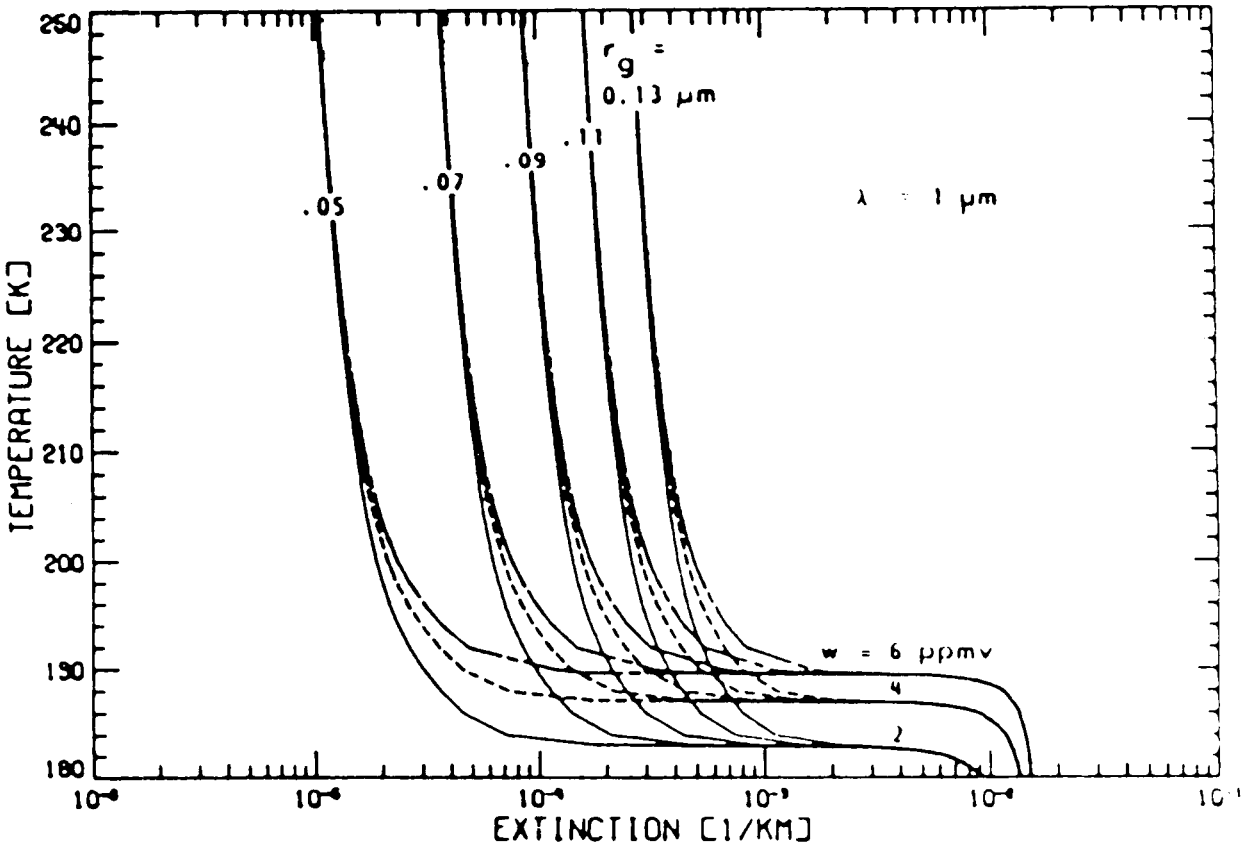


Figure 3.1c. The aerosol extinction at 1 μm as a function of temperature for water vapor mixing ratios of 2, 4, and 6 ppmv at 100 mb for mode radius $r_g$ = 0.05, 0.07, 0.09, 0.11, and 0.13 μm, with fixed values of σ in the lognormal aerosol size distribution: (c) σ = 2.064.

becomes reversed at sufficiently low temperatures as the aerosol particles have grown by absorbing large amounts of water molecules so that they become almost pure water droplets. These features have been noted by Steele et al. (1984). Figure 3.1 also depicts the sensitivity of the extinction to changes in $\sigma$. This sensitivity is better described in Fig. 3.2. Figure 3.2 shows the variation of the 1.0 μm extinction with temperature for a fixed mode radius $r_g$ (= 0.0725 μm) at the three constant $\sigma$ values mentioned earlier, i.e., 1.674, 1.86, and 2.046. For each of the $\sigma$ values, computations are carried out again for water vapor concentrations of 2, 4, 6 ppmv. Figure 3.2 shows that a 10% change in $\sigma$ may lead approximately to a factor of 3 change in the extinction for temperatures above a certain threshold value, below which the droplet becomes a supercooled particle.

The results of the corresponding analysis for wavelength 0.45 μm are given in Figures 3.3(a-c) and 3.4 in terms of the wavelength extinction ratio (defined as the ratio of extinction at 0.45 μm to that at 1.0 μm). One may notice from Figure 3.3, that for a fixed $\sigma$, a doubling of the value of $r_g$ leads to a reduction of this ratio by a factor of approximately 3, where $\sigma$ = 1.674, for a given water vapor concentration and a given temperature above 210°K. Figure 3.3 also shows that this reduction decreases as $\sigma$ increases. Figure 3.4 is the same as Figure 3.2, except that it is for the wavelength extinction ratio. It indicates that the sensitivity of the extinction ratio to changes in $\sigma$ for fixed values of $r_g$, temperature, and water vapor concentration depends on the value of $\sigma$ itself. A decrease of $\sigma$ from 1.86 to 1.674 leads to an increase of the ratio by a factor of approximately 2 in the case of $r_g$ = 0.0725 μm.

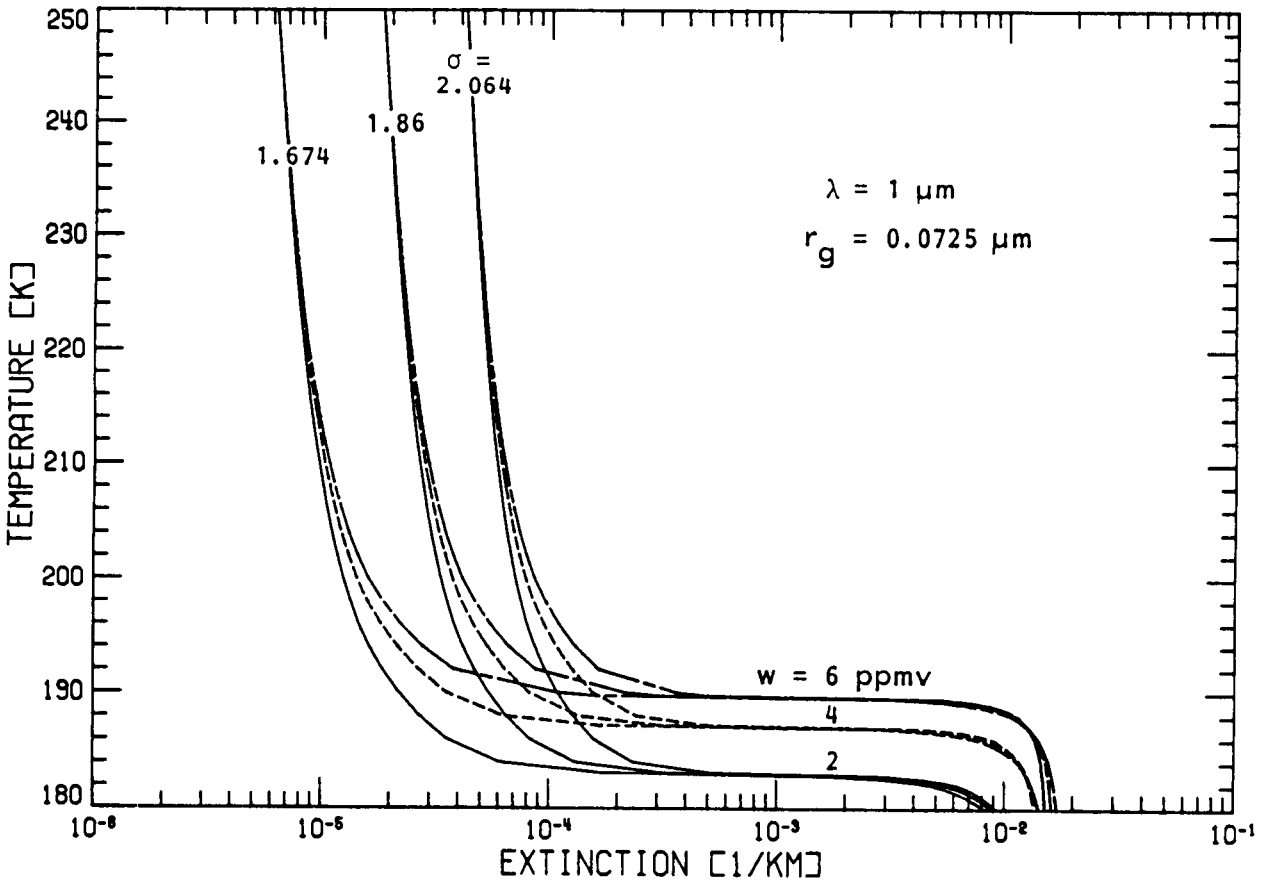


Figure 3.2. The aerosol extinction at 1 μm as a function of temperature for water vapor mixing ratios of 2, 4, and 6 ppmv at 100 mb for $r_g$ = 0.725 μm and σ = 1.674, 1,86, and 2.064 in the lognormal aerosol size distribution.

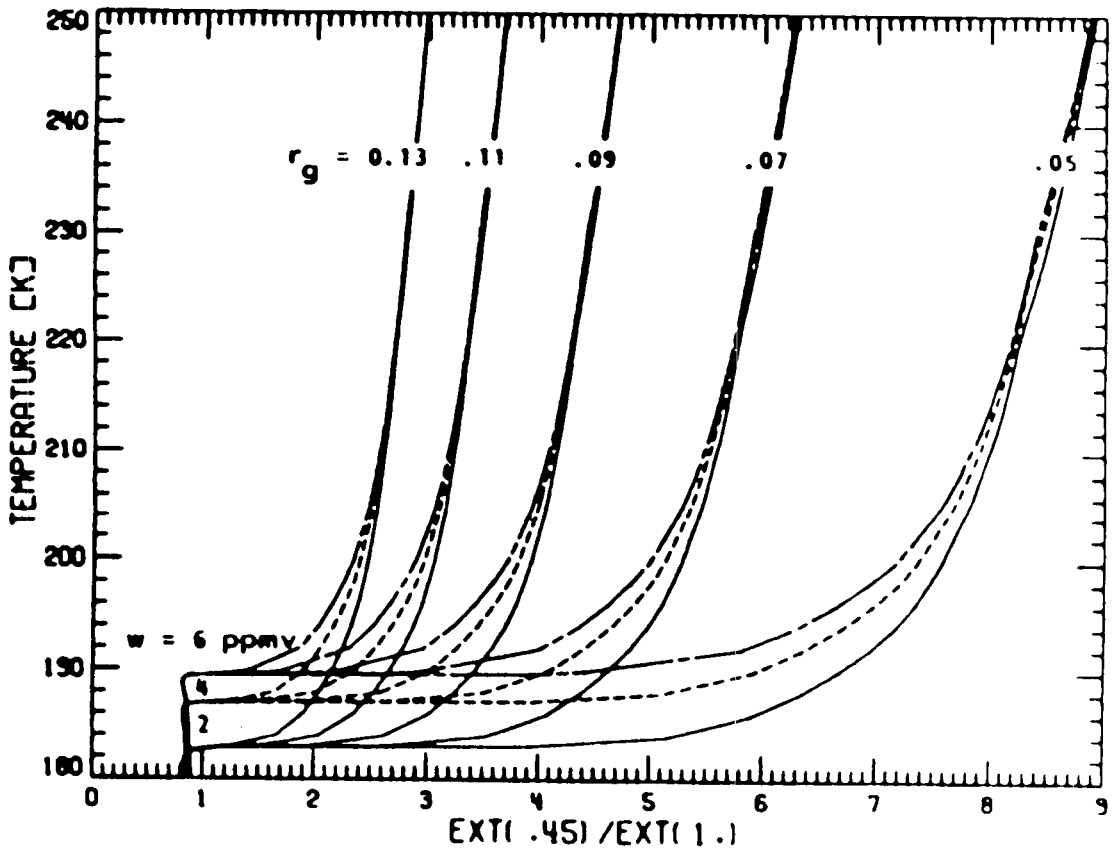


Figure 3.3a. The aerosol extinction ratio (aerosol extinction at 0.45 μm to that at 1.0 μm) as a function of temperature for water vapor mixing ratios of 2, 4, and 6 ppmv at 100 mb for mode radius $r_g$ = 0.05, 0.07, 0.09, 0.11, and 0.13 μm with fixed values of σ in the lognormal aerosol size distribution: (a) σ = 1.674.

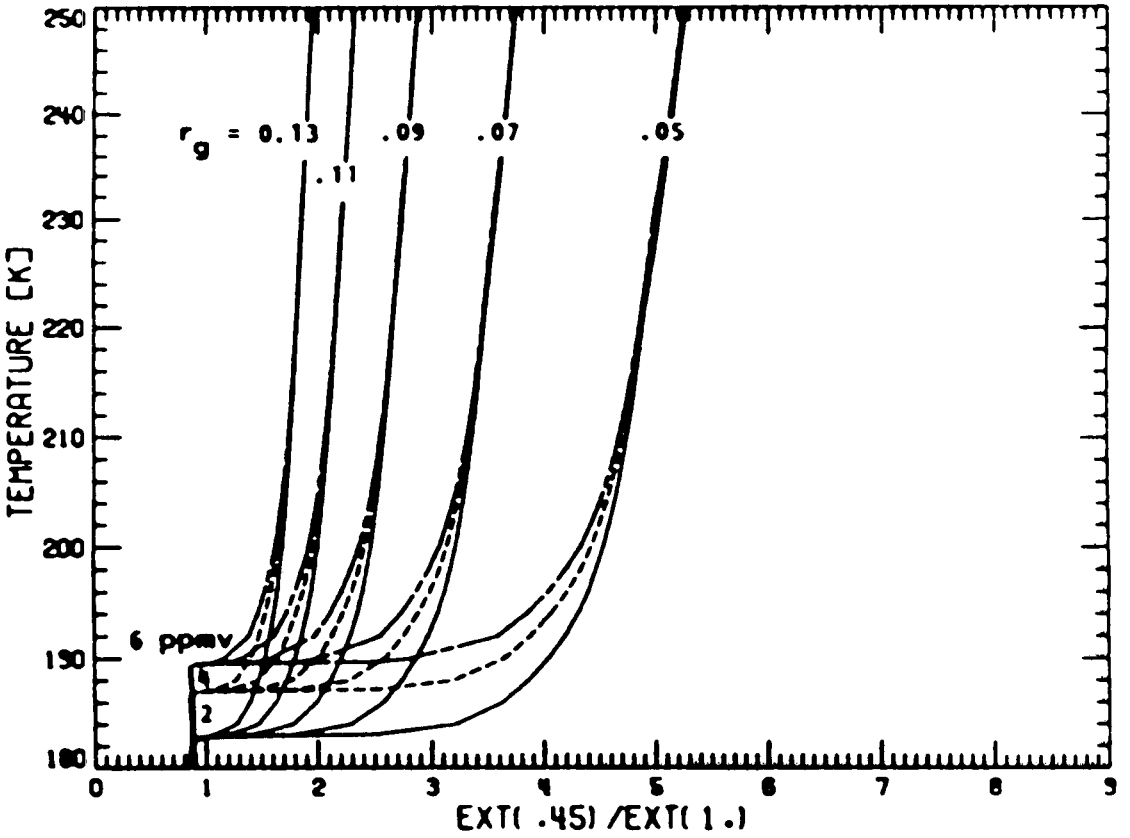


Figure 3.3b. The aerosol extinction ratio (aerosol extinction at 0.45 μm to that at 1.0 μm) as a function of temperature for water vapor mixing ratios of 2, 4, and 6 ppmv at 100 mb for mode radius $r_g$ = 0.05, 0.07, 0.09, 0.11, and 0.13 μm with fixed values of σ in the lognormal aerosol size distribution: (b) σ = 1.86.

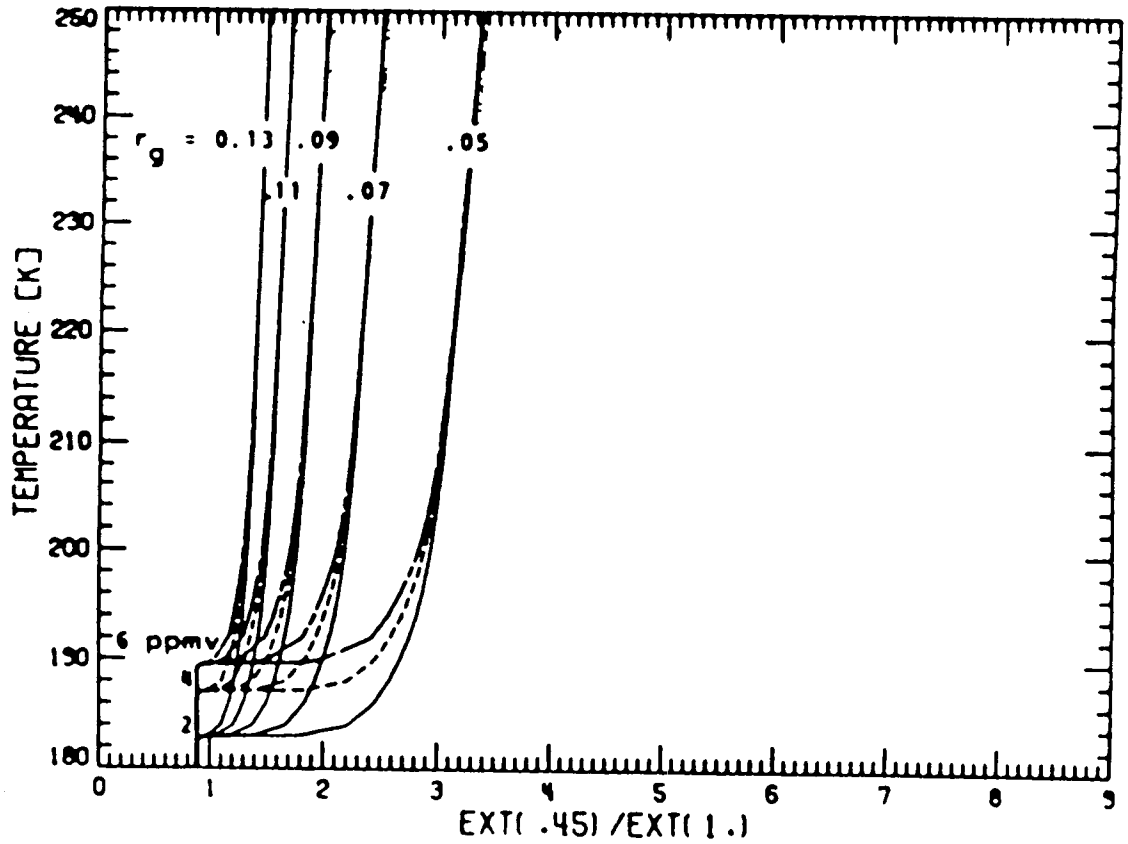


Figure 3.3c. The aerosol extinction ratio (aerosol extinction at 0.45 μm to that at 1.0 μm) as a function of temeprature for water vapor mixing ratios of 2, 4, and 6 ppmv at 100 mb for mode radius $r_g$ = 0.05, 0.07, 0.09, 0.11, and 0.13 μm with fixed values of σ in the lognormal aerosol size distribution: (c) σ = 2.064.

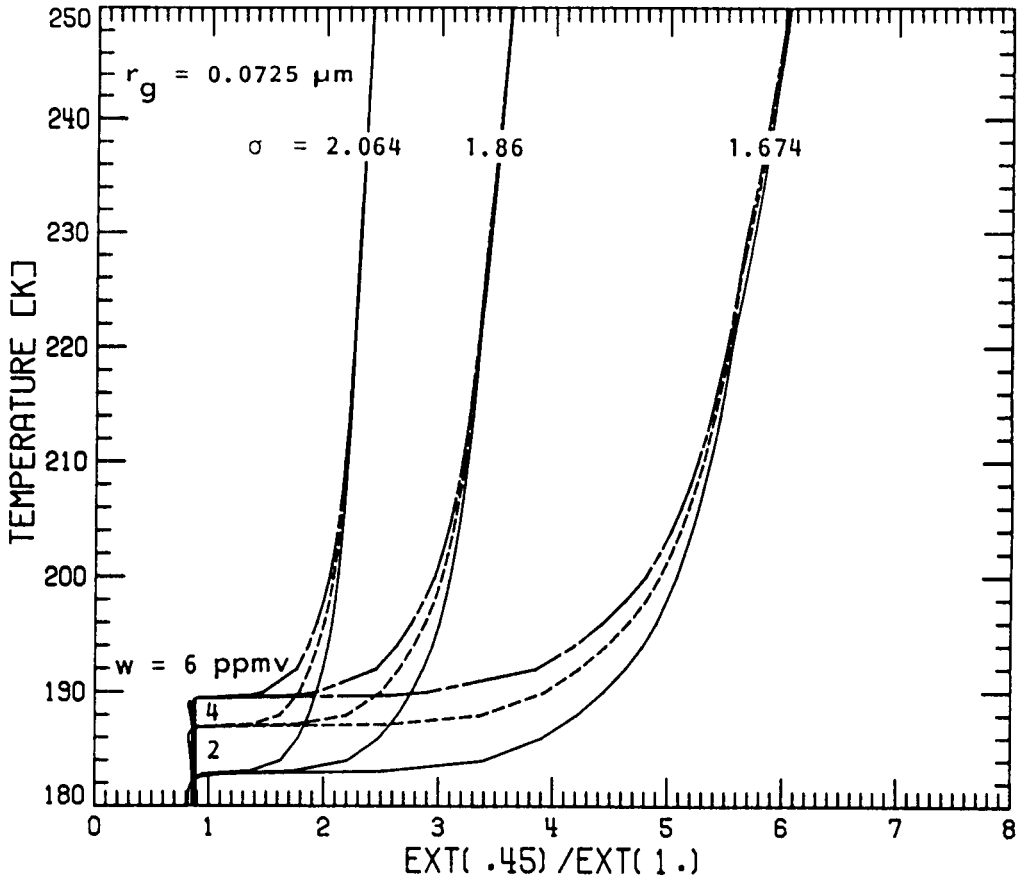


Figure 3.4. The aerosol extinction ratio (aerosol extinction at 0.45 μm to that at 1.0 μm) as a function of temperature for water vapor mixing ratios of 2, 4, and 6 ppmv at 100 mb for $r_g$ = 0.0725 μm and σ = 1.674, 1.86, and 2.064 in the lognormal aerosol size distribution.

To further examine the relationship between the mode radius $r_g$, and the wavelength extinction ratio under various values of water vapor concentration, $\sigma$, and temperature, the aerosol extinction ratio has been determined for a range of values of $r_g$ from 0.01 μm to 0.30 μm. The results of this calculation for a temperature 190°K are shown in Figure 3.5. Like the study given in Figure 3.2, the analysis involves three values of $\sigma$, i.e., 1.674, 1.86, and 2.046. For each of these values, the sensitivity study is carried out with respect to four different values of water vapor concentrations (from 2 ppmv to 8 ppmv). In Fig. 3.5, the results for 2 ppmv are given by the solid lines. The dashed lines correspond to 4 ppmv, and the solid-dashed lines are for 6 ppmv and 8 ppmv. First of all, the extinction ratio shows a monotonic increase with the decrease of the mode radius. Similar features can be found in the analysis by Yue and Deepak (1983, Figure 3.1a). Figure 3.5 also shows that the extinction ratio is sensitive to the value of $\sigma$, especially when the mode radius is small (e.g., less than 0.1 μm). As to the influence of the water vapor concentration, the ratio does not seem to be sensitive to its variation in the range from 2 ppmv to 8 ppmv. The reason that the two higher water vapor concentration cases, in particular, show very similar values for the extinction ratios is that, for the given $r_g$, temperature (190°K) and $\sigma$, the aerosol particles are supercooled droplets in this model calculation. As a result, they have very similar optical properties. From Figure 3.5, it is clear that the extinction ratio is rather insensitive to the water vapor concentration in the range from 2 ppmv to 8 ppmv at a given temperature. Similar computations have been made for temperature at 200°K and 210°K. The results of these computations

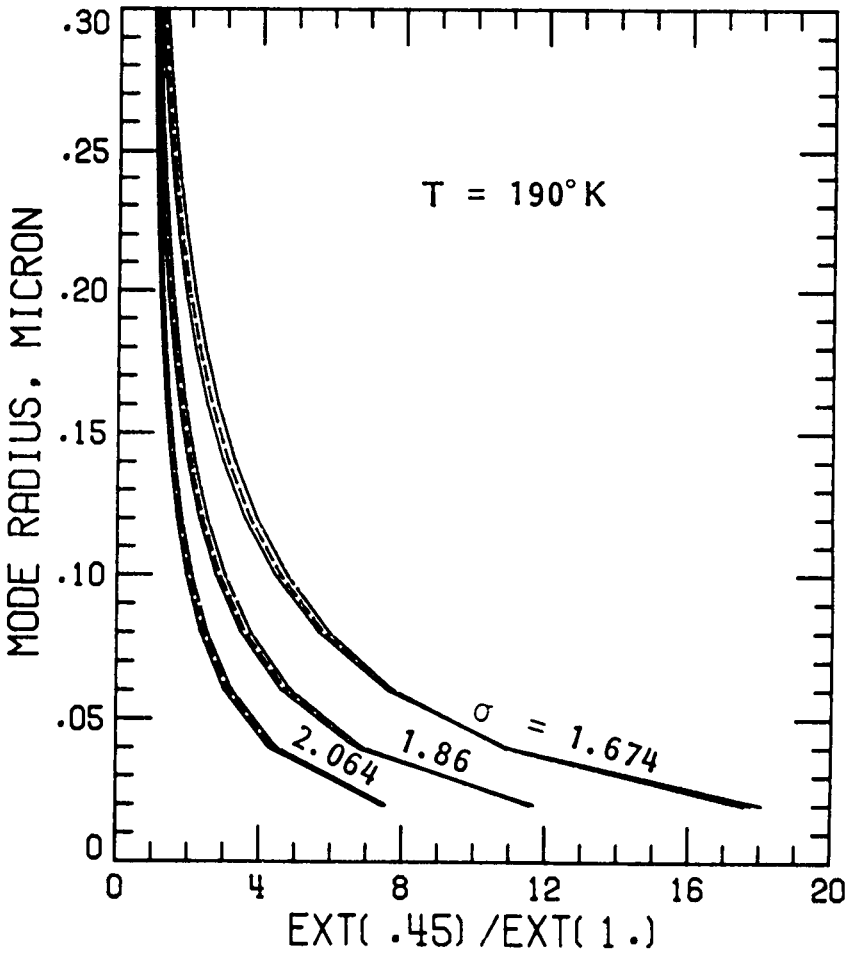


Figure 3.5. The aerosol extinction ratio (aerosol extinction at 0.45 μm to that at 1.0 μm) as a function of mode radius $r_g$ for $\sigma$ = 1.674, 1.86, and 2.064 in the log-normal aerosol size distribution. The temeprature is fixed at 190°K.

differ only slightly from those shown in Fig. 3.5. In other words, the extinction ratio is not very sensitive to changes in temperature.

### 3.1.3 Discussion.

Satellite technology gives us an effective means of studying stratospheric aerosols with global scale coverage. These measurements are accomplished through determination of the optical properties of aerosol particles. The interpretation of the measured optical properties, as well as the retrieval from satellite extinction measurements of the essential parameters of these particles, such as size distribution, composition etc., rely on detailed model analyses. In this section, we have examined the effect of temperature, water vapor, and aerosol size distribution on the aerosol extinctions at 0.45 μm and 1.0 μm wavelengths, and their ratio (0.45 μm to 1.0 μm). It is concluded that the extinctions at these two wavelengths are not sensitive to changes in ambient water vapor pressure but to the mode radius ($r_g$) for temperatures greater than about 210$^{o}$K. This condition becomes reversed at sufficiently low temperatures. If we vary the width of the size distribution $\sigma$, it is found that a 10% change in $\sigma$ may lead approximately to a factor of 3 change in the extinctions. As to dependence of the wavelength extinction ratio on ambient temperature, water vapor concentration, and the size distribution, it is shown that, for sufficiently small mode radius ($r_g$ < 0.1 μm), the extinction ratio is sensitive to changes in mode radius. This sensitivity increases with the decrease of the mode radius. It is also found that the wavelength extinction ratio is not sensitive to changes in ambient temperature and water vapor concentration but to the width of the size

distribution ($\sigma$), especially when the mode radius is less than 0.1 μm. As a result of this sensitivity, one can only derive an equivalent mode radius from the extinction information at two wavelengths (i.e., 0.45 μm and 1.0 μm). This feature has been noted in the study by Lenoble et al. (1984). They mentioned that, roughly, an increase of $\sigma$ from 1.6 to 1.92 gives results equivalent to an approximate reduction of radius ($r_g$) by a factor of 2. Obviously, to resolve this problem, it is necessary to incorporate at least a third independent extinction measurement. With this additional information, it is possible to determine $\sigma$ appeared in Eq. 3.1. As shown in Section 6.1, the SAGE II multiwavelength aerosol extinction measurements allow us to derive $\sigma$ as well as $r_g$ in the retrieval analysis. Furthermore, the measurement from the SAGE II water vapor channel will also lead to information about the composition of the stratospheric aerosols.

### 3.2 Dependence of Aerosol Composition on Water Vapor and Temperature

The preliminary results of the SAGE II water vapor measurements during April 1985 are being used in conjunction with the temperature profiles provided by NOAA to investigate the chemical composition of stratospheric aerosols. This investigation also serves as an additional data validation analysis for the SAGE II water vapor measurement. In this analysis, the water vapor partial pressures at a given standard pressure level in the lower stratosphere are obtained from the SAGE II measurements using an interpolation scheme. The interpolated results are set in a 2-dimensional space, (i.e., water vapor pressure against temperature). The results of a typical example of the analysis at 100 mb pressure level are given in Figure

3.6. Figure 3.6 shows also the distribution curves of equilibrium water vapor pressure as a function of temperature for pure water, pure ice, and six different $H_2SO_4$ weight percentages of sulphuric acid-water solutions. As one can see, the majority of the April observations show an equilibrium water vapor pressure of about $3 \times 10^{-4}$mb, and indicate a $H_2SO_4$ weight percentage of 70% or so for aerosol droplets. In Figure 3.6, several SAGE II measurements of water vapor pressure show values lower than $3 \times 10^{-5}$mb. These values are unlikely to be real for the reason that the associated air parcels would have to go through an environment with temperatures below 180°K to have most of the water removed. These low SAGE II water vapor results may have occurred due to over-correction for the aerosol effects on the water vapor channel measurements (private communication with W. P. Chu).

Figure 3.6 also indicates that many SAGE II water vapor measurements suggest relatively low values of $H_2SO_4$ weight percentage of the aerosol droplets. These aerosol particles may be of tropospheric origin and are located in the tropics. In order to see the vertical variations of the aerosol composition, the preliminary SAGE II water vapor information and the associated temperature profile have been used to estimate the percentage weight of $H_2SO_4$ in the aerosol droplets. We have plotted each vertical profile sampled in the tropical region separately from that of northern high latitudes (> 50°N) to gain some understanding of the latitudinal variation. These results are displayed in Figures 3.7a and 3.7b, respectively. As shown in Figure 3.7a, all the typical profiles are featured generally by a down-slope from the upper right of the figure, corresponding to high

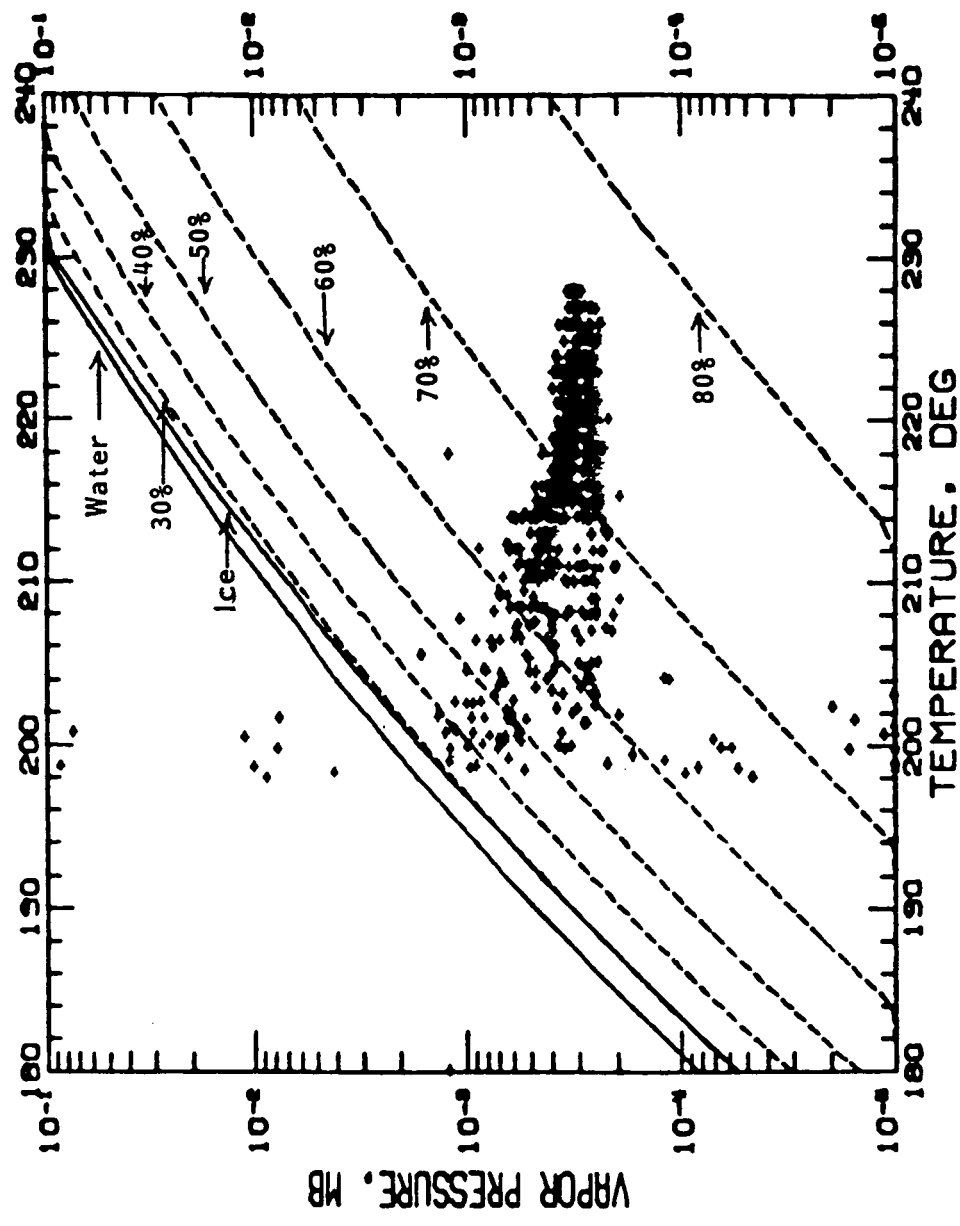


Figure 3.6. The vapor pressure as a function of temperature over water, ice, and six different $H_2SO_4$ weight percentages of sulphuric acid-water solutions. The crosses correspond to the SAGE II water vapor measurements and the associated temperatures.

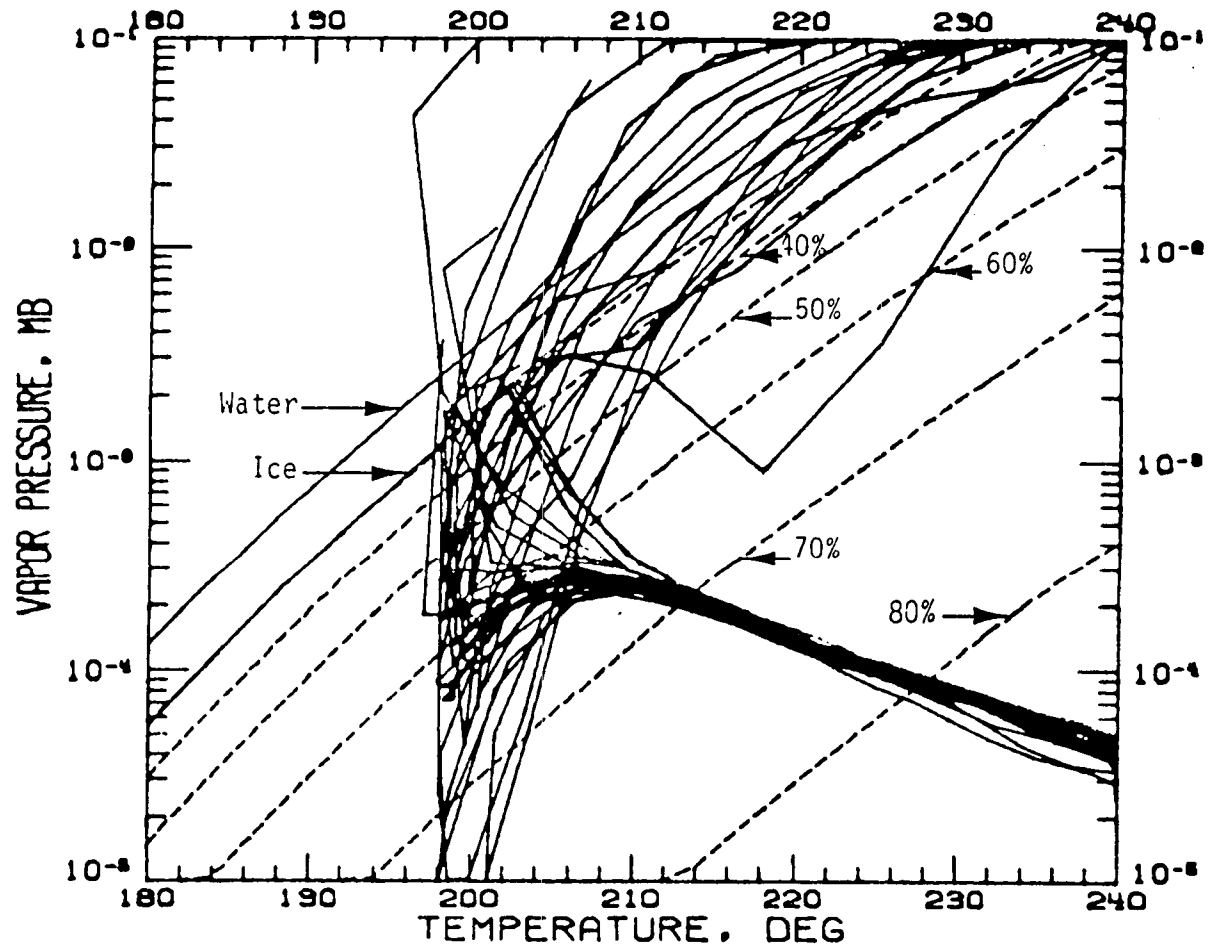


Figure 3.7a. Distributions of the preliminary SAGE II water vapor measurements between ± 10° latitude and associated temperature (provided from NOAA), April 1985 in the 2-dimensional space of temperature and vapor pressure. Shown also in the figure are the saturation vapor pressure of pure water, ice, and six different percentages of $H_2SO_4$ (by weight) of sulphuric acid-water solutions.

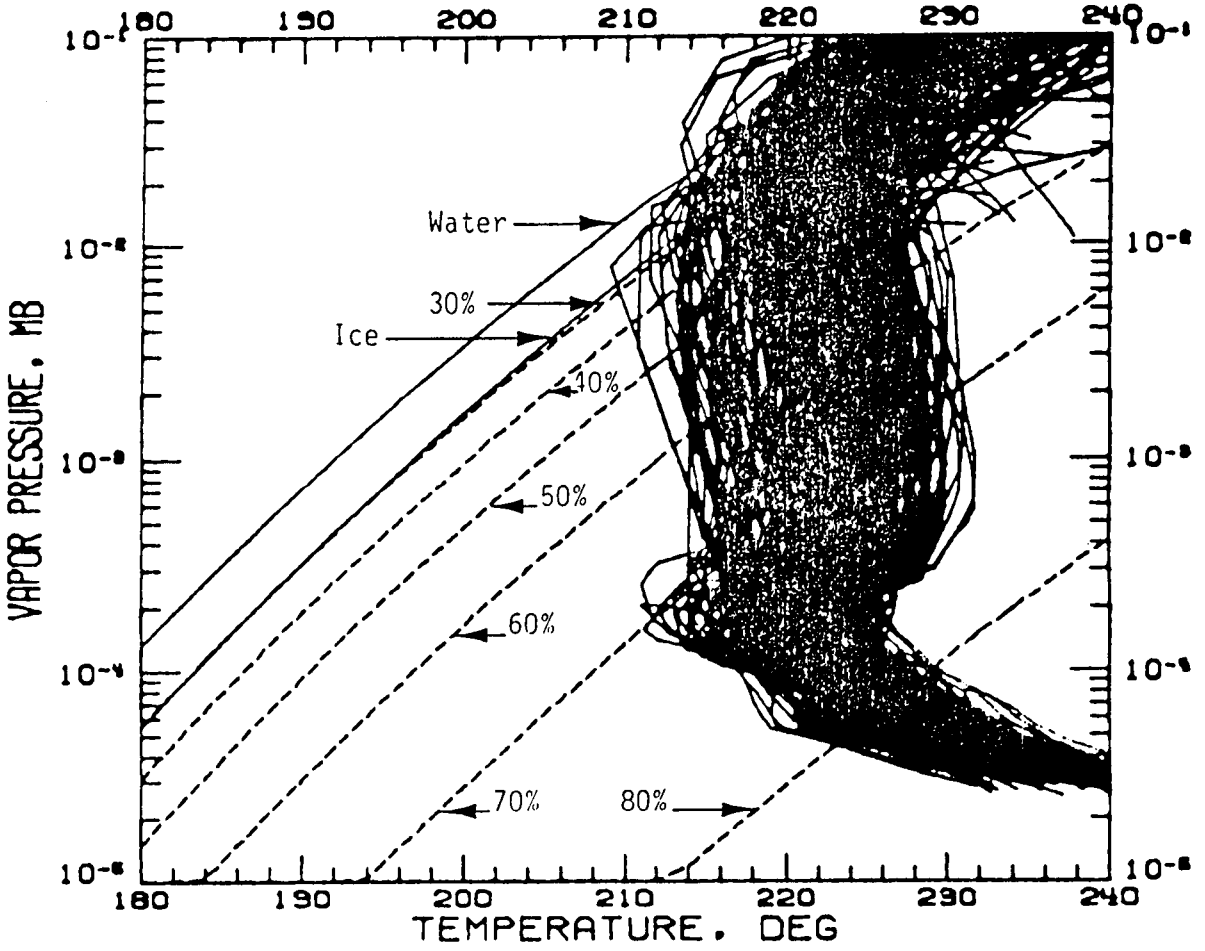


Figure 3.7b. Same as for Figure 3.7a. except for SAGE II high latitude measurements ( >50°N).

temperature and high pressure, to the low temperatures ($\sim 200^{o}K$) as the altitude increases. As the altitude increases futher, all the profiles become merged together at a location specified approximately by $T=210^{o}K$ and $V=2.5x10^{-4}mb$. These profiles then slope down toward the right as the altitude continues to increase. It must be pointed out that the part of the profile which shows higher water vapor pressure than that for the pure water is unlikely to be real. Similarly, the portion of the data with the water vapor pressure below $\sim 10^{-4}mb$ near $T=200^{o}K$ is probably questionable.

In the case of April 1985 SAGE II water vapor at northern high latitudes ($> 50^{o}N$), Figure 3.7b indicates generally that the temperature and water vapor pressure decreases first as the altitude increases until a temperature $\sim 200^{o}K$ is reached. This characteristic temperature must correspond to the tropopause temperature at this high latitude region. Since the altitude of this temperature extends up several kilometers, the vertical profiles of the water vapor on T-V diagram show a drop of water vapor pressure with relatively less temperature changes as the altitude increases in this particular altitude region. The further increase in altitude results in further decreases in water vapor pressure and increases in temperature. Thus, the profiles on the T-V plot show a sloping down towards the lower right corner similar to that in the tropics (Figure 3.7a).

In conclusion, we have found that the behavior of the water vapor and temperature in the tropics for the month of April is generally different from that at high latitudes. In addition, the existing SAGE II preliminary water vapor data set at high latitudes looks more reasonable than that in the

tropics. However, since the lower water vapor values may be the result of an aerosol correction problem and since the aerosol loading from El Chichon seems to be decaying (see Section 4.1), the SAGE II water vapor data should become more reasonable with time than exhibited in the April 1985 data set.

# 4. TASK 3--INVESTIGATE THE INJECTION OF VOLCANIC MATERIAL INTO THE STRATOSPHERE INCLUDING GLOBAL LOADING AND TRANSPORT

## 4.1 Stratospheric Effects of the El Chichon Volcanic Eruption

The most significant event affecting the stratospheric aerosol that has occurred within the past twenty years was the series of eruptions of the El Chichon volcano in March/April 1982. These eruptions unfortunately occurred after the failure of the SAGE I Application Explorer Mission Satellite power supply and before the launch of SAGE II. The stratospheric injection by these eruptions has been such as to dominate the stratospheric aerosol for several years after the eruptions. It is only recently that the aerosol level, still several times that existing at its lowest value in 1979, has dropped enough for the effects of other smaller eruptions to be detectable (e.g., that of Ruiz in November, 1985). In spite of the fact that global satellite extinction data were not available for the earlier phases of the El Chichon period, the effects have been well studied. Methods of study have included use of data gathered by the SAM II satellite and NASA-LaRC airborne lidar system, as well as by numerous other experimental techniques. In view of the importance of these eruptions and the relatively strong effects still remaining at the time of launch of SAGE II, a review has been prepared on the observations of the effects between April 1982 to July 1985. This review has included data from SAM II, the NASA-LaRC airborne lidar, as well as early data from SAGE II. Where appropriate and necessary, data from other sensor systems have been integrated. The review was presented as an invited paper at the Workshop on Ozone Variations on Climatological Time Scales:

Observations and Theory and Perturbations by UV Flux Variations and the Eruption of El Chichon, held in Salzburg, Austria, August 19-22, 1985. A copy of the abstract of the review paper is attached to this report as Appendix 2. The paper is scheduled to be published as part of a Middle Atmosphere Program (MAP) Handbook (Kent and McCormick, 1985b).

## 5. TASK 4--INCLUDING THE STUDY OF PHYSICAL AND CHEMICAL PROCESSES

### 5.1 Analysis of SAGE II and Correlative Measurements on August 7, 1985 at Fairbanks, Alaska

The presence of aerosols in the lower stratosphere and the upper troposphere affects the retrieval of SAGE II water vapor measurements. This is also particularly true when there are occurrences of subvisible or visible cirrus clouds (Woodbury and McCormick, 1983, 1986). It is found that during the SAGE II ground correlative measurements conducted on August 7, 1985 at Fairbanks, Alaska, the aerosol extinction measurements from the SAGE II instrument revealed the presence of clouds. This situation is illustrated in Figure 5.1. In this section, we discuss the analysis of the formation and evolution of aerosols including their physical and chemical properties using this SAGE II and correlative data set. Since the satellite instrument is viewing the atmosphere from space, it is possible to locate the cloud top height within $\approx$ 0.5km which is the accuracy of the vertical resolution of the SAGE II instrument. Figure 5.1 indicates clearly the cloud top is located somewhere between altitudes 11 and 12 km. This result is further confimred by the correlative dustsonde observations. Figure 5.2 shows the vertical profiles of the dustsonde measurements for the $N_{1.2}$ and $N_{1.8}$ channels. The distinct peaks of these two channels, which appeared at altitude 12 km, are remarkable. These two profiles further indicate that the vertical extent of the subvisible cloud is a little over 1 km.

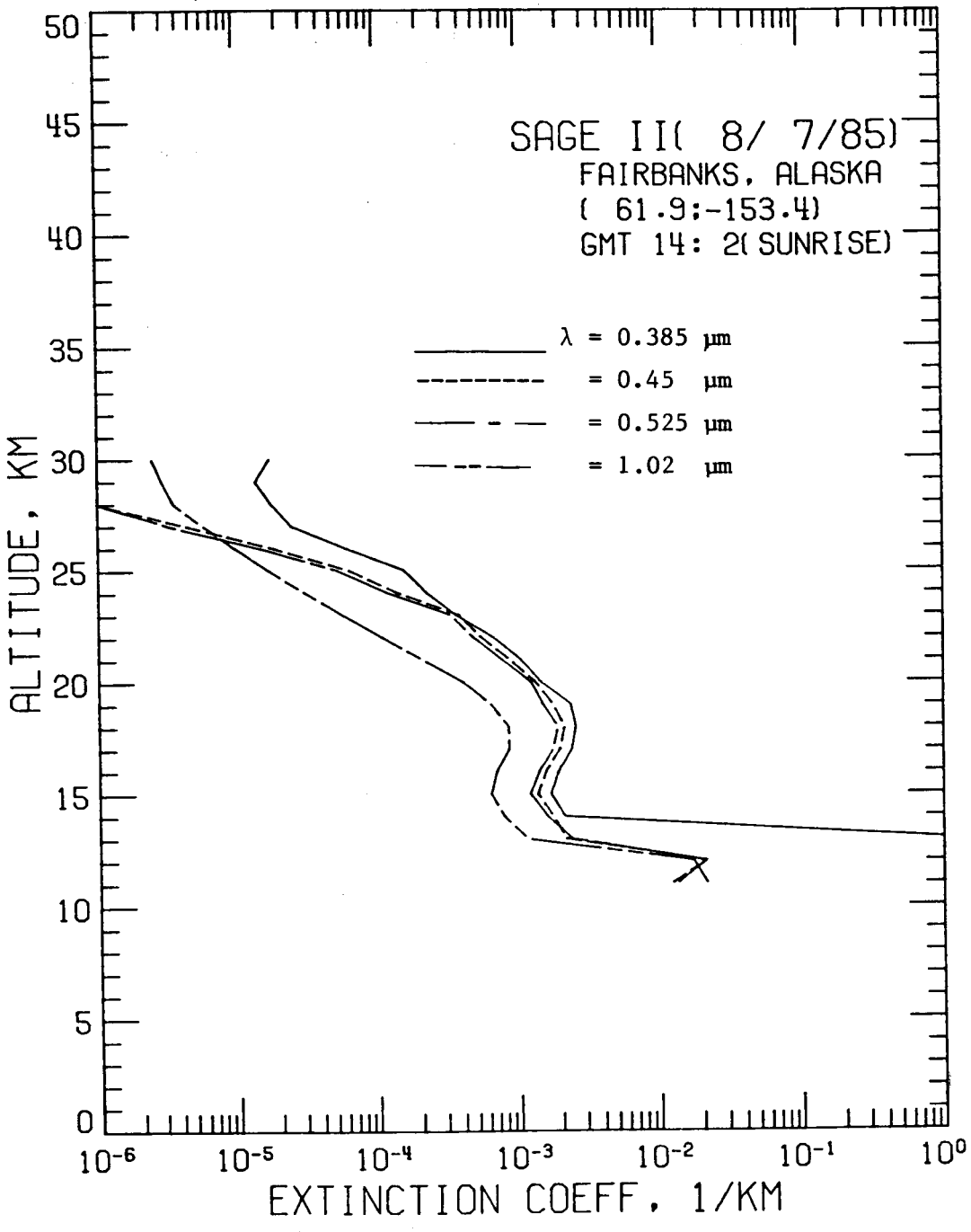


Figure 5.1. Preliminary SAGE II aerosol extinction profiles obtained on August 7, 1985, at Fairbanks, Alaska.

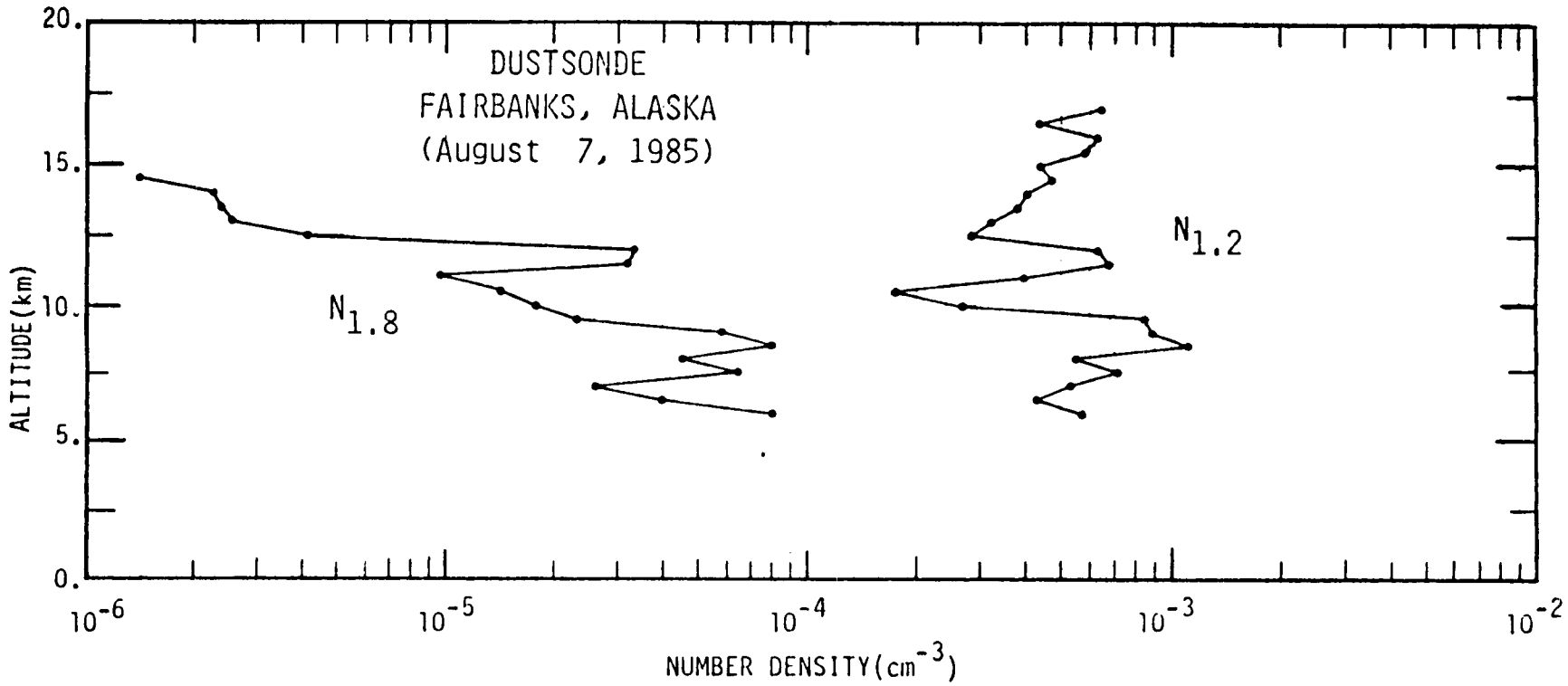


Figure 5.2. Vertical profiles of total number density for aerosol particles with radii greater than 1.2 and 1.8 μm, respectively, from dustsonde observations made at Fairbanks, Alaska, August 7, 1985.

The associated temperature profile for the dustsonde measurements is displayed in Figure 5.3 by the dots. Figure 5.3 also shows the temperature profile obtained by Oltmans of NOAA/ARL, and that of the SAGE II preliminary data set provided by NOAA. Although there is some difference in temperature between the one associated with dustsonde measurements and that obtained by Oltmans, they both indicate a layer of coldest air located approximately at an altitude of 12 km. They also suggest that the vertical extent of this coldest layer is about 1 km. Since this is at summer season, it is possible that the convective activity leads to upward air motion, and the formation of clouds through adiabatic cooling processes. It is also possible that this cloud is developed by associating with a frontal system. In order to see the details of the development, we have examined the available correlative water vapor profiles. The water vapor pressure and the corresponding temperature from Oltmans' measurements and that provided on the SAGE II profile tape is plotted on a T-V diagram (i.e., temperature against vapor pressure). This is given in Figure 5.4. The advantage of using a T-V diagram is that it provides an estimate of the weight percentage of $H_2SO_4$ for the stratospheric aerosol droplets, and also indicates possible formation of water or ice clouds. In Figure 5.4, the five numbers in the parentheses by the symbols indicate the altitudes in kilometers of Oltmans' measurements. The location of the corresponding data point of the SAGE II observations at the same altitude can be identified by the corresponding symbol in this T-V diagram.

In Figure 5.4, the results of Oltmans' in situ measurements are different in two aspects from those inferred from the SAGE II data set. In

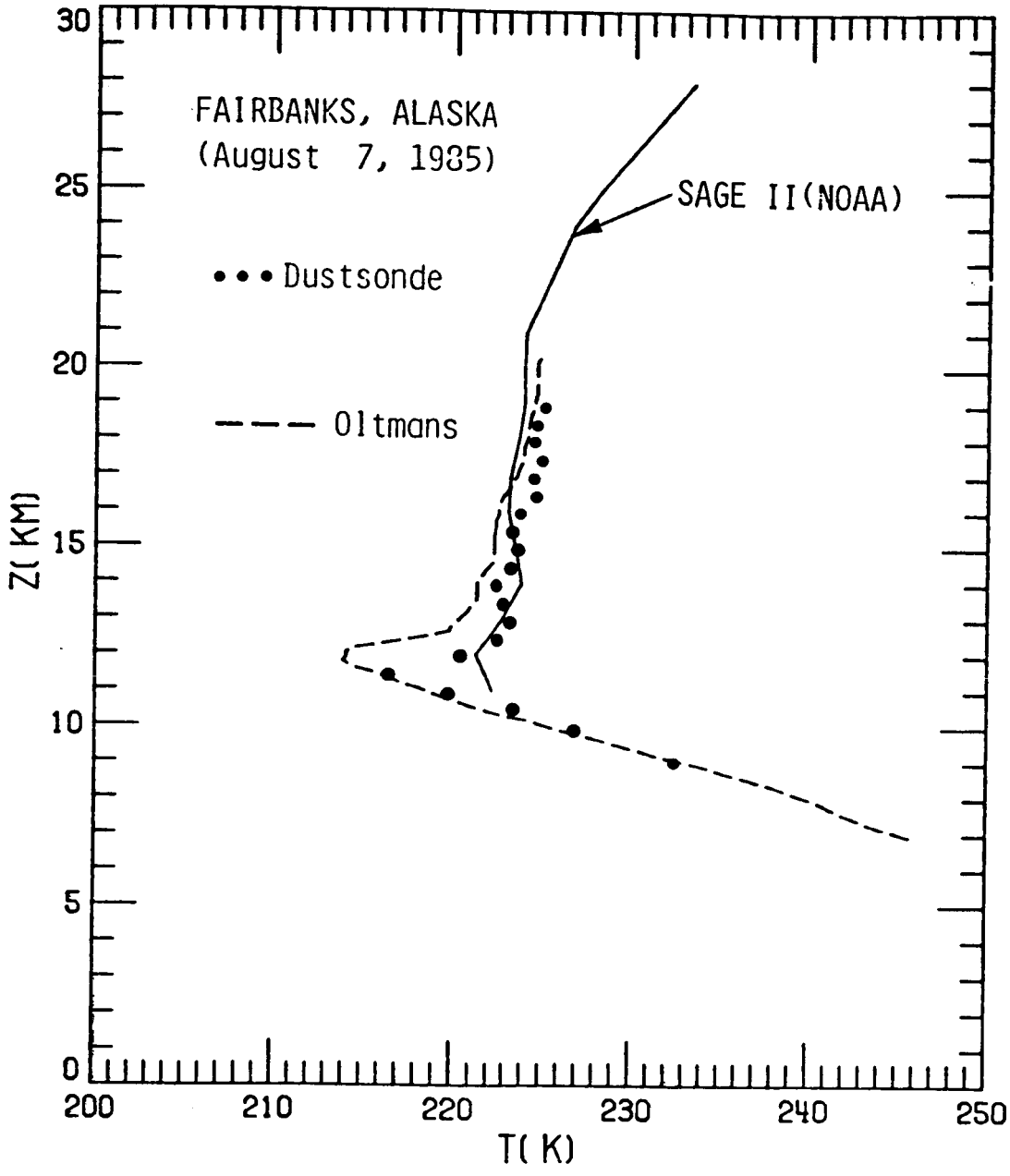


Figure 5.3. Comparison of temperature profiles associated with dustsonde observation, Oltmans' water vapor measurements, and SAGE II (NOAA).

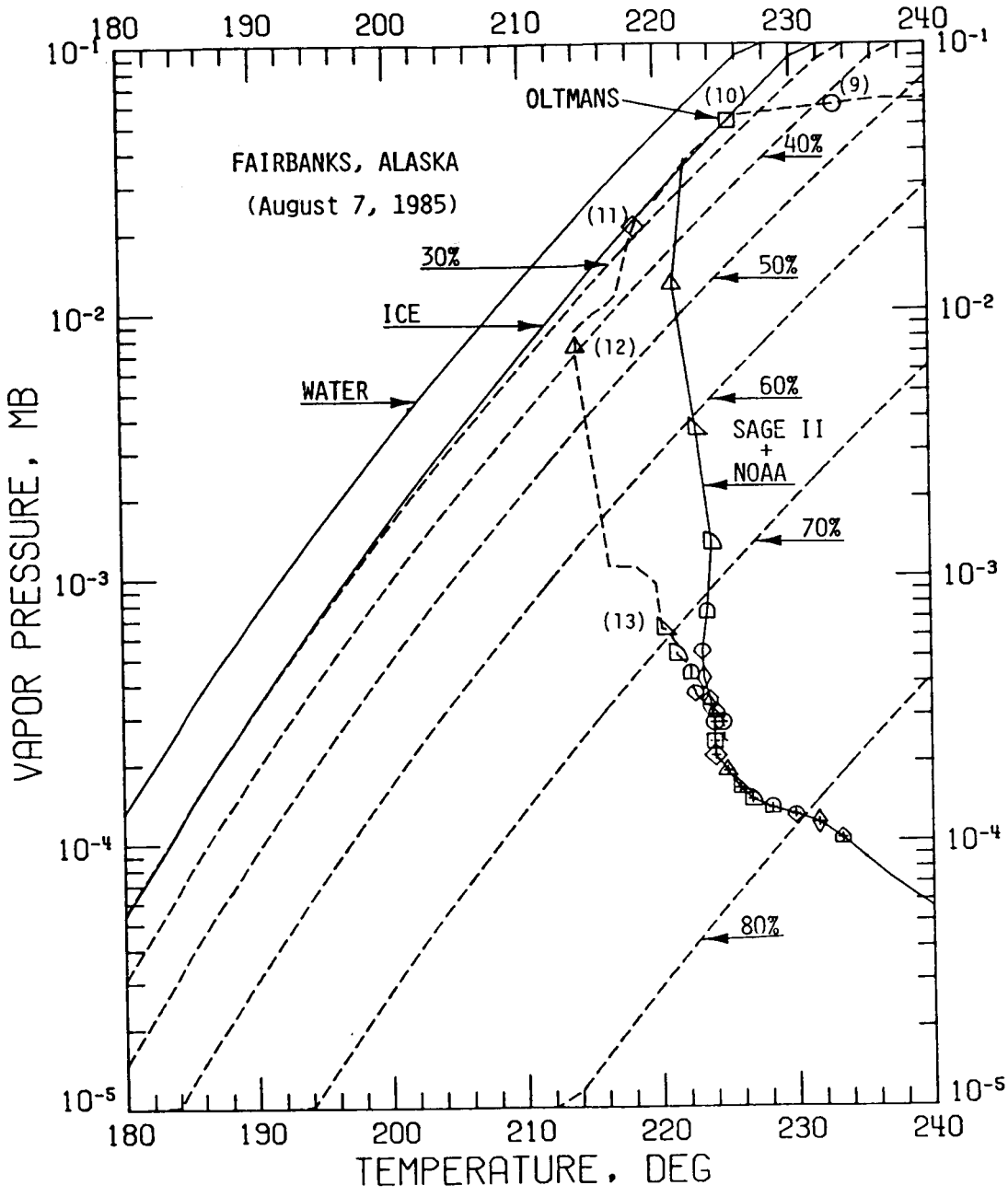


Figure 5.4. The vapor pressure as a function of temperature over water, ice and six different $H_2SO_4$ weight percentages of sulphuric-water solutions. The two profiles with symbols are obtained from Oltmans' observations and from SAGE II water vapor and NOAA temperature data. The numbers in the brackets indicate the altitude in km of associated data points (symbols).

the first place, NOAA satellite derived temperature data on SAGE II profile tapes is about 5°C higher than Oltmans' balloon data. Secondly, the preliminary SAGE II water vapor data below altitude 15 km are about a factor 2 greater than Oltmans'. For this reason, the following discussion is based on Oltmans' results. It is interesting to note that his data at 10 km are located right on the saturation vapor pressure curve for pure ice. This feature indicates that the bottom of the cloud layer is about at this level. At altitude 11 km, the data point is still very close to the pure ice curve. As the altitude increases from 11 km, the observed vapor pressure departs from the pure ice curve. The data at 12 km, as one can see, correspond approximately to the level of the coldest temperature (also shown in Figure 5.3). Figure 5.4 further indicates that at 12 km, the aerosol droplets are possibly composed of 40% of $H_2SO_4$ and 60% of $H_2O$ by weight. At 13 km, on the other hand, the corresponding composition is about 70% $H_2SO_4$ and 30% of $H_2O$. In view of the above discussion, based on Figure 5.4, the cloud layer appears to extend approximately from 10 km to 11 km. This cloud top location is consistent with the results of SAGE II aerosol extinction data set within the accuracy of the SAGE II vertical resolution.

In conclusion, both the SAGE II satellite instrument and the correlative measurements, including that made by the dustsonde and Oltmans' water vapor sounding, observed the cloud layer during this ground truth event. This cloud layer appears to consist of ice particles generated by adiabatic cooling processes associated with the upward air motion. Further detailed analyses on this cloud development and studies of the aerosol corrections to the SAGE II water vapor measurements are recommended.

# 6. TASK 5--INVESTIGATE THE DETERMINATION OF STRATOSPHERIC MOLECULAR AND AEROSOL OPTICAL PROPERTIES USING MULTIWAVELENGTH EXTINCTION AND BACKSCATTER DATA AND TECHNIQUES

## 6.1 Aerosol Data Validation in Terms of Retrieved Aerosol Size Distribution from SAGE II Multiwavelength Aerosol Extinctions

As mentioned in Section 3.1, model aerosol size distributions can be determined from SAGE II multiwavelength aerosol extinctions. To determine the model parameters, we have used a nonlinear least squares approach. Single mode lognormal as well as modified-gamma functions have been used in the size distribution analysis. In addition, a bi-lognormal size distribution can be determined by using both multiwavelength SAGE II aerosol extinction data and lidar backscatter data at ruby and green wavelengths. The retrieved size distributions can then be used to determine the optical properties of the aerosol particles and to calculate the total number density of aerosol droplets corresponding to dustsonde measurements. These derived results from retrieved size distributions can be used for data validation by comparison with correlative measurements. In the following analysis, we discuss first the information content of SAGE II aerosol extinctions with respect to aerosol size distribution. This is important, since it helps us to understand the quality of the retrieved aerosol size distribution. With this information, we then discuss the data validation for SAGE II observations on two particular days, when correlative measurements were available. Part of this analysis in this section has been presented in the sixth conference of Atmospheric Radiation at Williamsburg, Virginia on May 13-16, 1986 (Wang et al., 1986).

### 6.1.1 SAGE II aerosol size distribution information content

The aerosol size distribution information content associated with a given optical measurement can be described approximately in terms of the corresponding efficiency factor Q ($\lambda$, m, r). The distribution of the efficiency factors at SAGE II aerosol wavelengths are displayed in Figure 6.1. As can be seen, Figure 6.1 indicates that the best information of aerosol size distribution in the SAGE II aerosol extinction measurements is within the radius range between approximately 0.28 and 0.80 μm. A second source of the limits of the retrievable size range of a set of optical measurements is governed by the so-called ratio-criterion. According to this criterion, there is no information about aerosol size distribution that can be extracted from optical measurements at any two wavelengths in a radius range where the ratio of the two corresponding efficiency factors is a constant. The calculated results of the ratio of $Q_e^{.525}/Q_e^{1.02}$ and $Q_e^{.385}/Q_e^{1.02}$ are given in Figure 6.2. Figure 6.2 also shows the ratio of $Q_s^{.532}/Q_e^{1.02}$. As one can see from Figure 6.2, the nonretrievable radius range lies below the radius of 0.1 μm and above about 1.0 μm. In addition, as one would expect, the information content near these limits becomes relatively poor as revealed by the distributions of the efficiency factor in Figure 6.1.

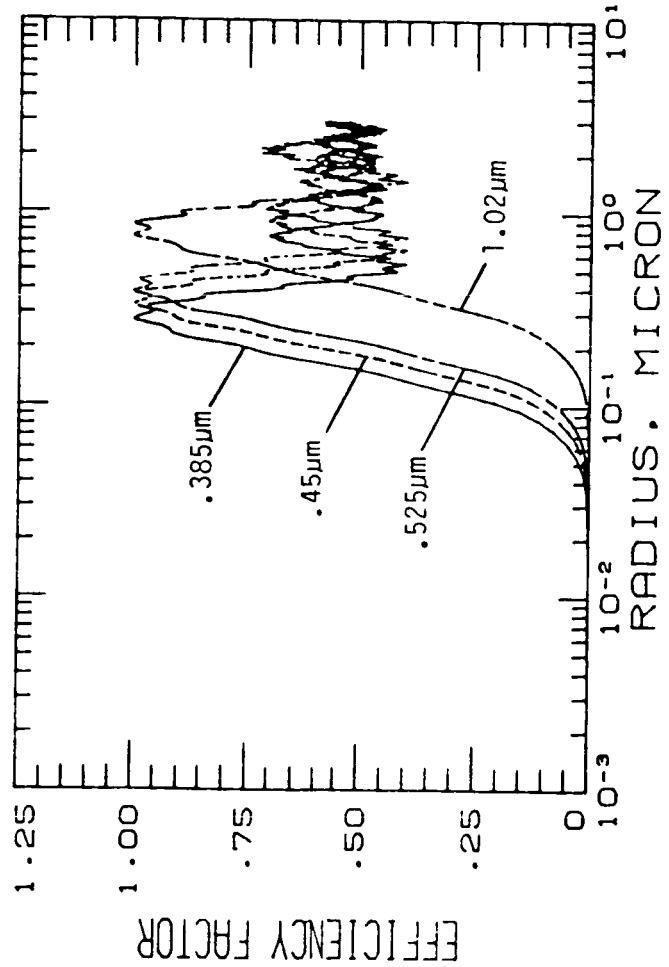


Figure 6.1. Efficiency factors at SAGE II aerosol wavelengths for background atmospheric aerosols.

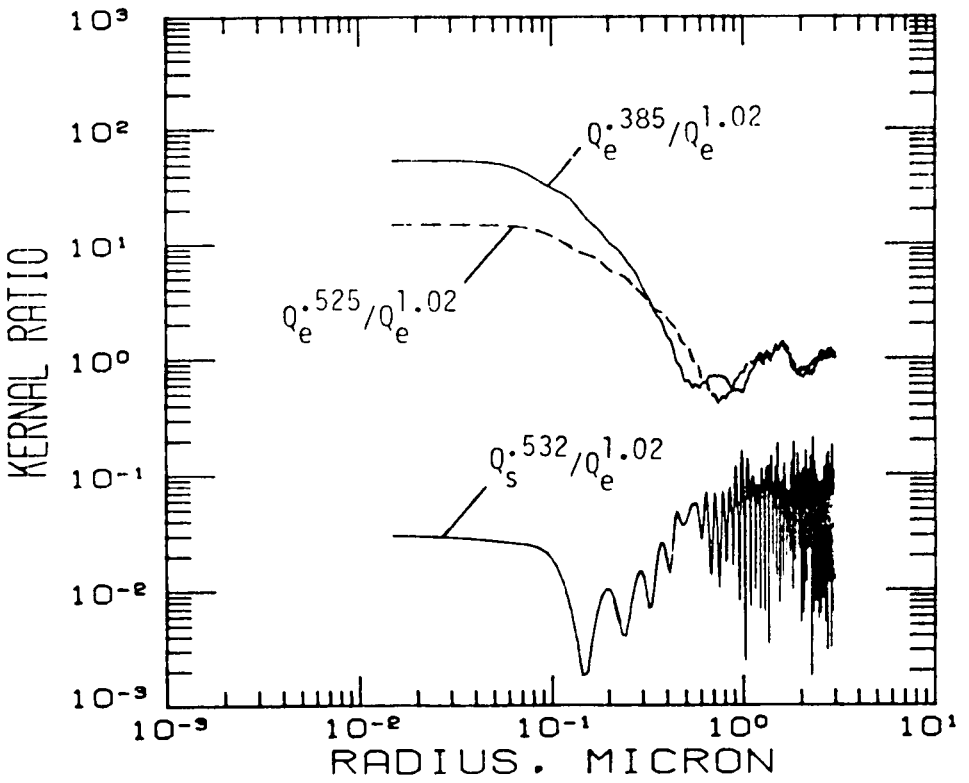


Figure 6.2. Ratios of efficient factors at different wavelengths for background stratospheric aerosols.

### 6.1.2 Data comparison

November 30, 1984 (Laramie, Wyoming)

Figure 6.3 shows the stratospheric aerosol size distribution at altitudes (a) 15 km; (b) 18 km; (c) 21 km; and (d) 24 km. The two single mode aerosol size distributions are derived from SAGE II aerosol extinction measurements alone. The bi-mode model distribution is retrieved using both SAGE II and lidar aerosol optical measurements. Figure 6.3 indicates the close agreement among the three model distributions in the radius range between approximately 0.2 and 0.7 μm. Large variations are shown outside this range. This feature is consistent with the conclusions mentioned in Section 6.1.1.

Figure 6.4 shows the comparison of the backscatter coefficients obtained from lidar observations and from calculations based on aerosol size distributions retrieved from SAGE II aerosol extinctions. In general, there is a reasonable agreement between the observations and the derived results based on retrieved model size distributions, except near the altitude of 24 km.

A comparison of $N_{.15}$ and $N_{.25}$ between dustsonde observations and calculations based on aerosol size distributions retrieved from SAGE II and correlative lidar observations is provided in Figure 6.5. Figure 6.5 indicates that the retrieved model size distributions yield values of $N_{.15}$ which are greater than those of dustsonde observations for all three analytic models. On the other hand, substantial improvement is found in the results of $N_{.25}$ calculated using the bi-lognormal representation.

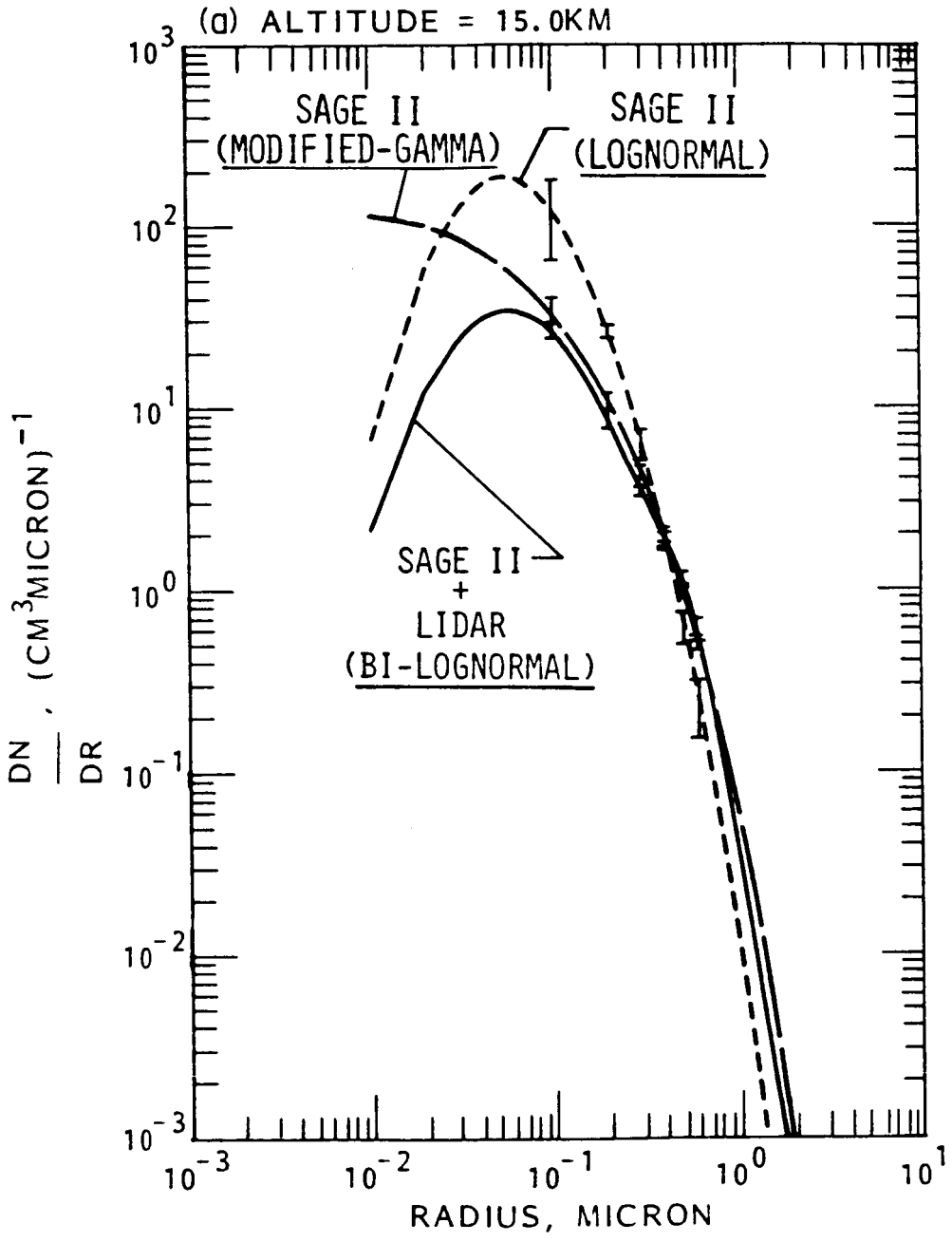


Figure 6.3a. Stratospheric aerosol size distributions derived from SAGE II aerosol extinctions at 15 km altitude.

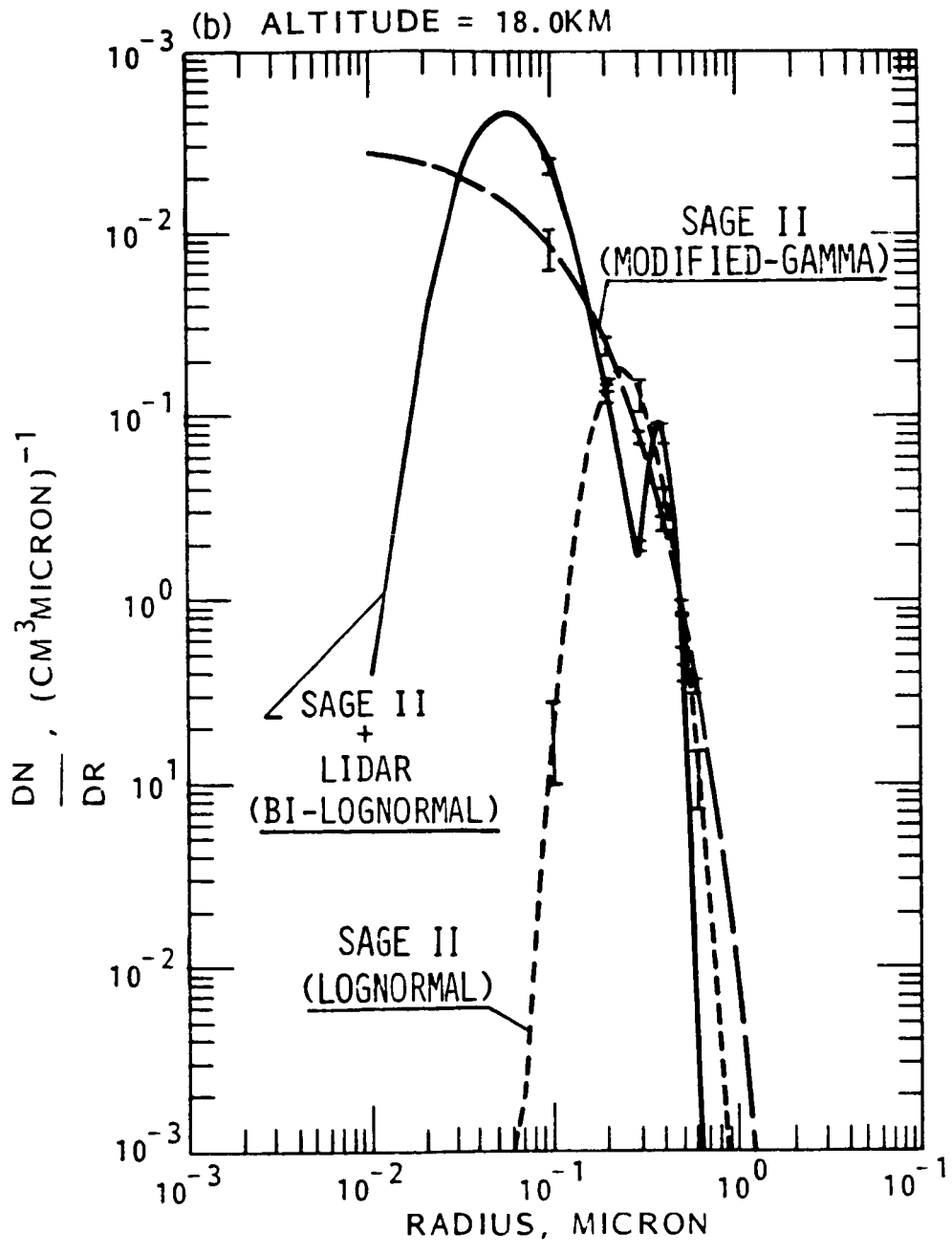


Figure 6.3b. Stratospheric aerosol size distributions derived from SAGE II aerosol extinctions at 18 km altitude.

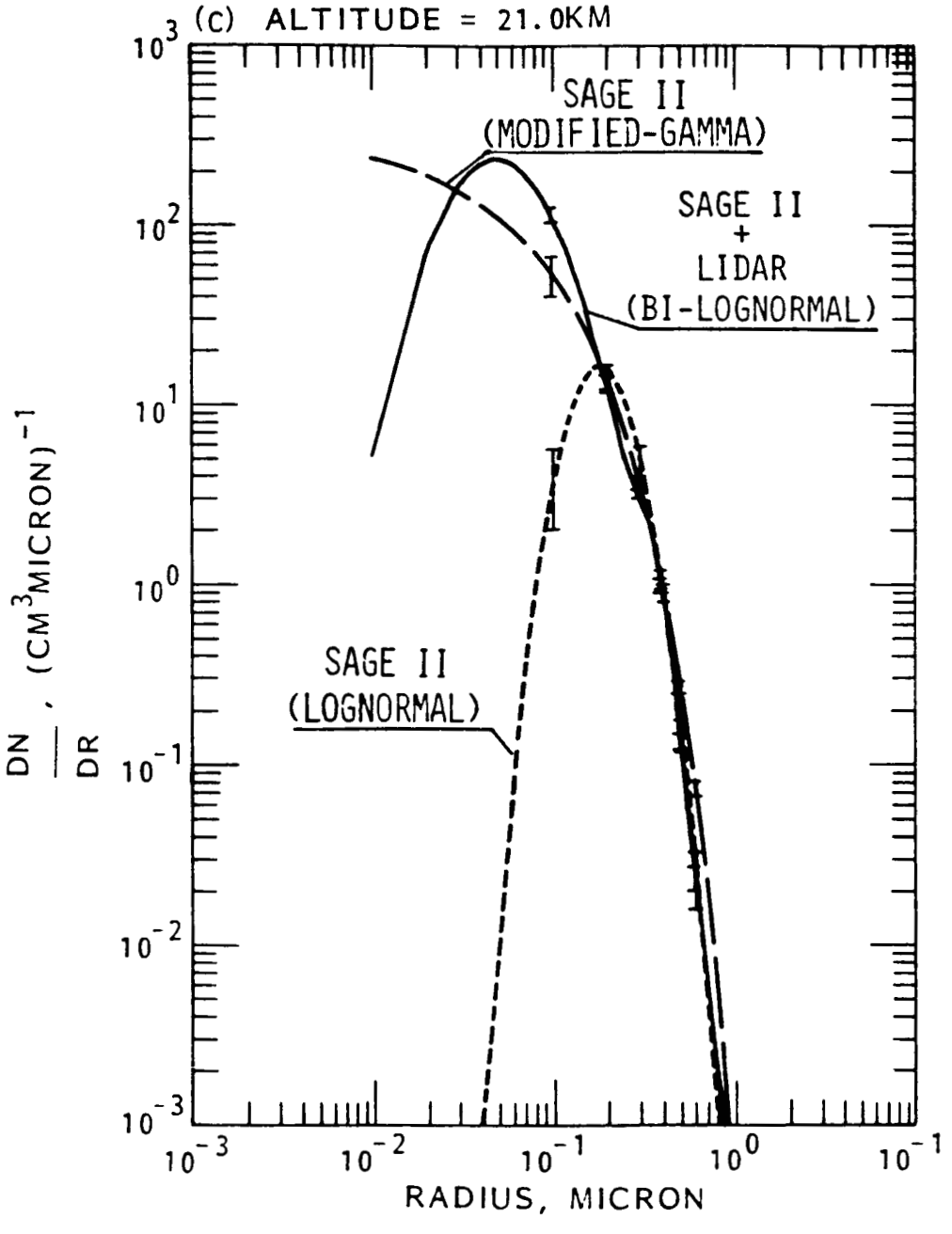


Figure 6.3c. Stratospheric aerosol size distributions derived from SAGE II aerosol extinctions at 21 km altitude.

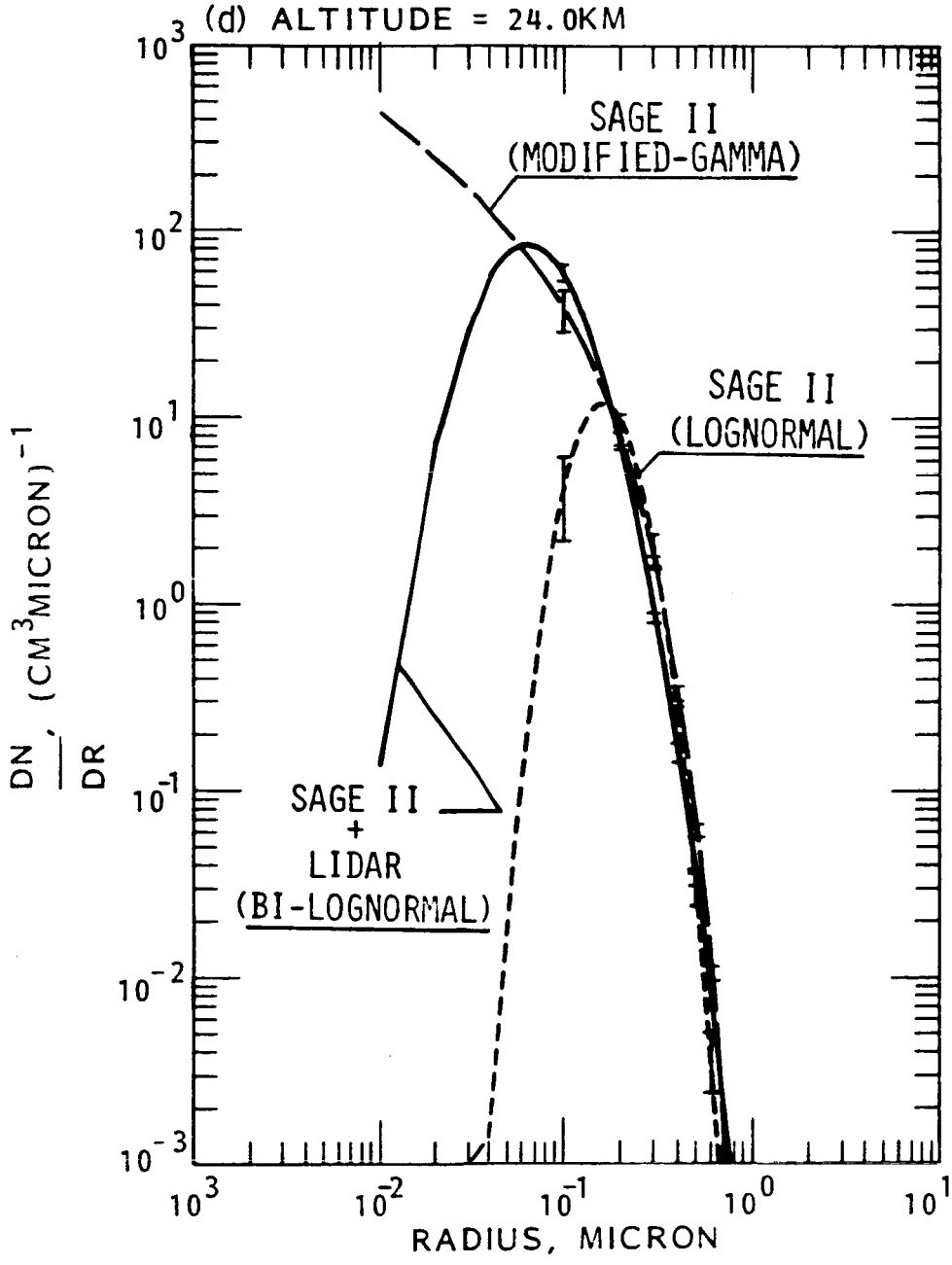


Figure 6.3d. Stratospheric aerosol size distributions derived from SAGE II aerosol extinctions at 24 km altitude.

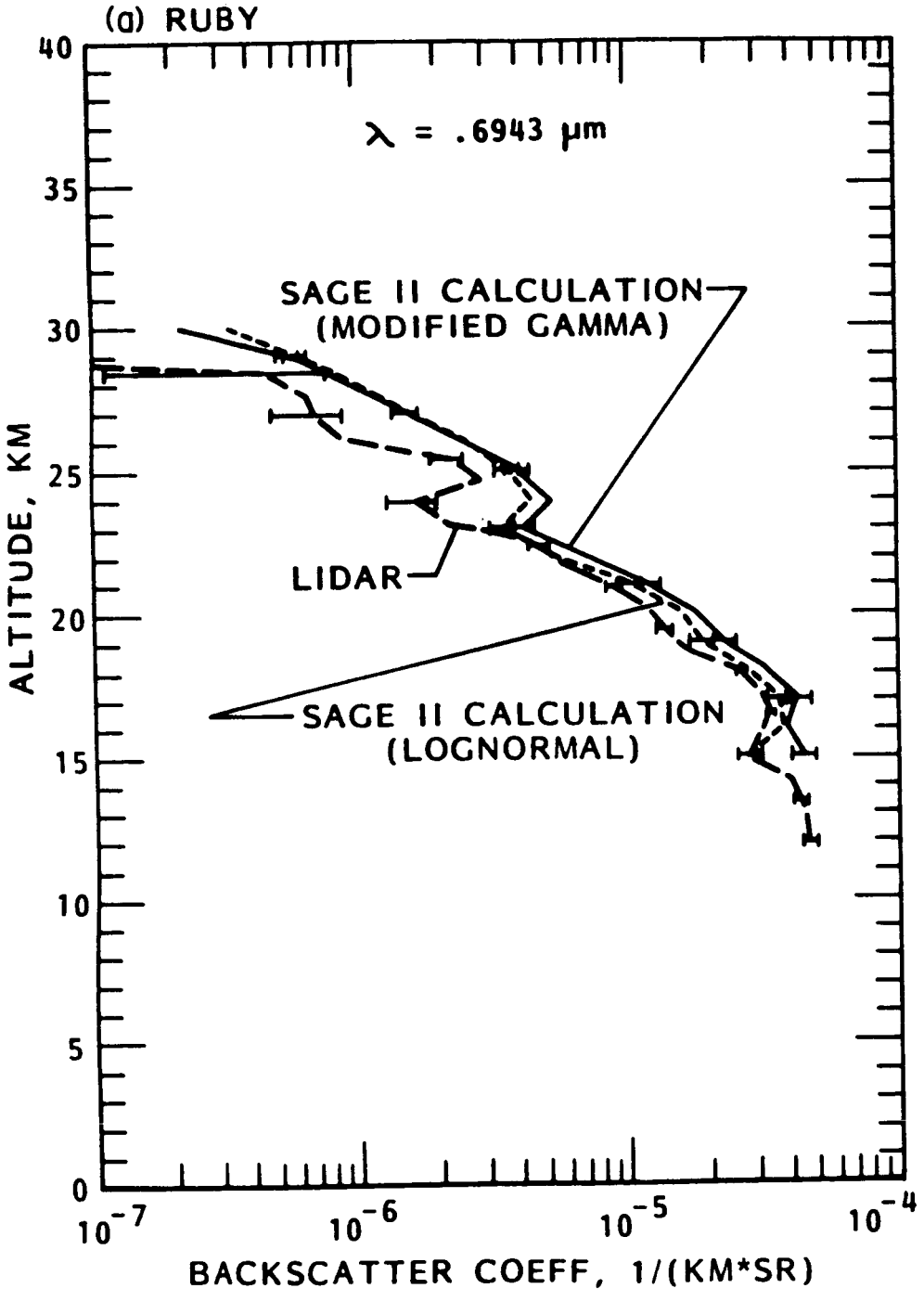


Figure 6.4a. Comparison of the backscatter coefficients obtained from lidar observations and from calculations based on aerosol size distributions retrieved from SAGE II aerosol extinctions.

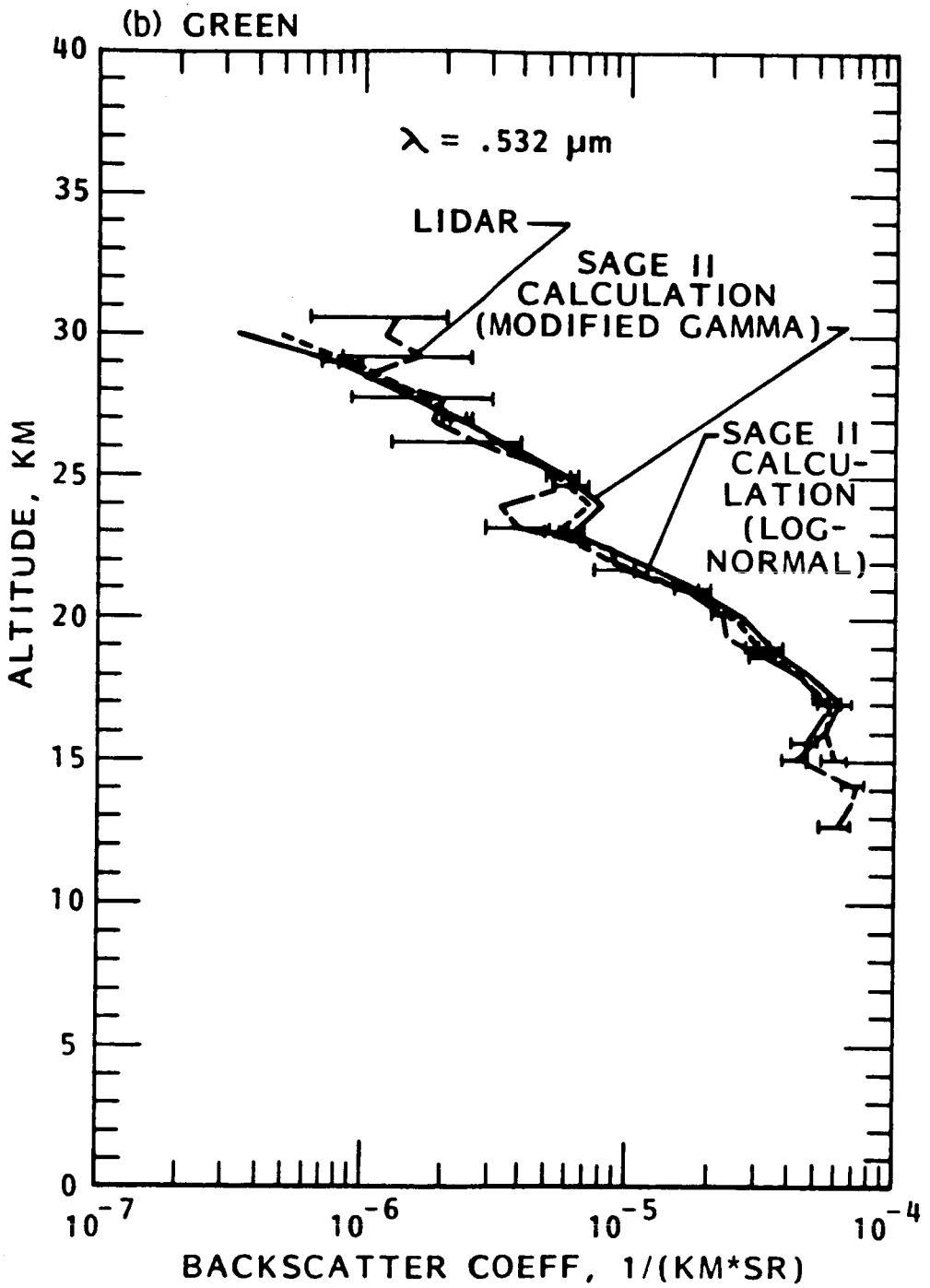


Figure 6.4b. Comparison of the backscatter coefficients obtained from lidar observations and from calculations based on aerosol size distributions retrieved from SAGE II aerosol extinctions.

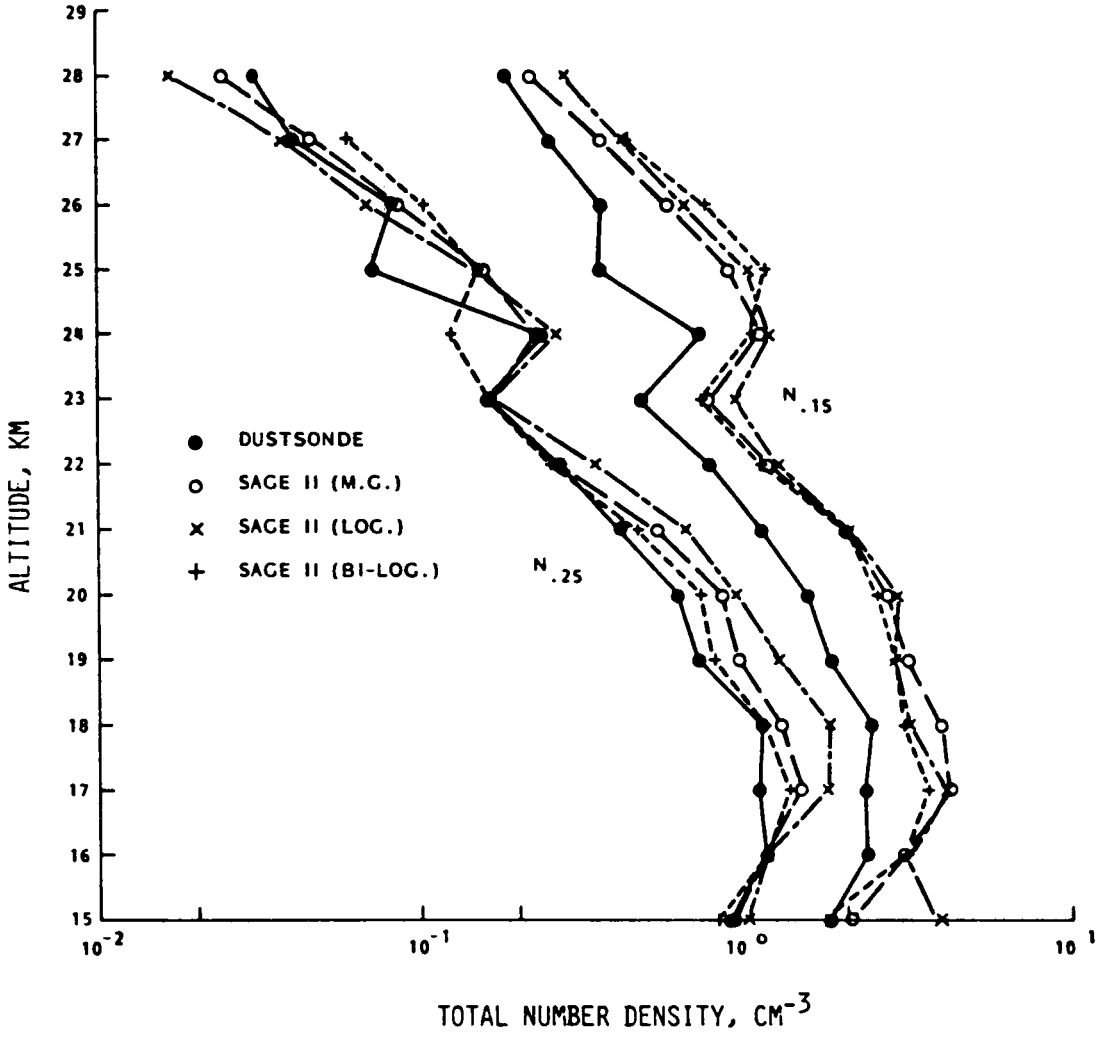


Figure 6.5. Comparison of $N_{.15}$ and $N_{.25}$ obtained from dustsonde measurements and calculated results based on retrieved aerosol size distribution using SAGE II aerosol extinctions.

January 9, 1985 (Laramie, Wyoming)

Figure 6.6a to 6.6c are the same as Figure 6.3, except that they are for data obtained at altitudes of 15.2, 18.3, and 21 km, and that the dustsonde measurements of $N_{.01}$, $N_{.15}$, and $N_{.25}$ were used together with SAGE II aerosol extinctions to derive a bi-modal size distribution. In Figure 6.6, the dots show wire-impactor data obtained by V. Overbeck of NASA Ames Research Center. Again, Figure 6.6 indicates the general agreement among the three different model size distributions in the radius range between approximately 0.3 μm and 1.0 μm, especially at an altitude of 15.2 km. In addition, at an altitude of 15.2 km, the model size distributions agree well with the results of the wire impactor, except at r = .05 μm.

## 6.2 Lidar Measurements in the Upper Stratosphere and Mesosphere

The NASA-Langley 48" lidar system has been used for routine ground-correlative measurements in association with both the SAGE I and SAGE II satellites. The long term data set on stratospheric aerosol backscatter obtained with this instrument, which extends back to 1974, is a unique source of information on the long-term climatology of the aerosol in the northern hemisphere. Current use of the system is mainly confined to the region of the atmosphere below 30 km in altitude. This concentration of effort owes much to the fact that the stratospheric aerosol layer lies almost entirely within this region. The 48" lidar system was nevertheless designed with the inherent capability of being used to probe much higher in the stratosphere,

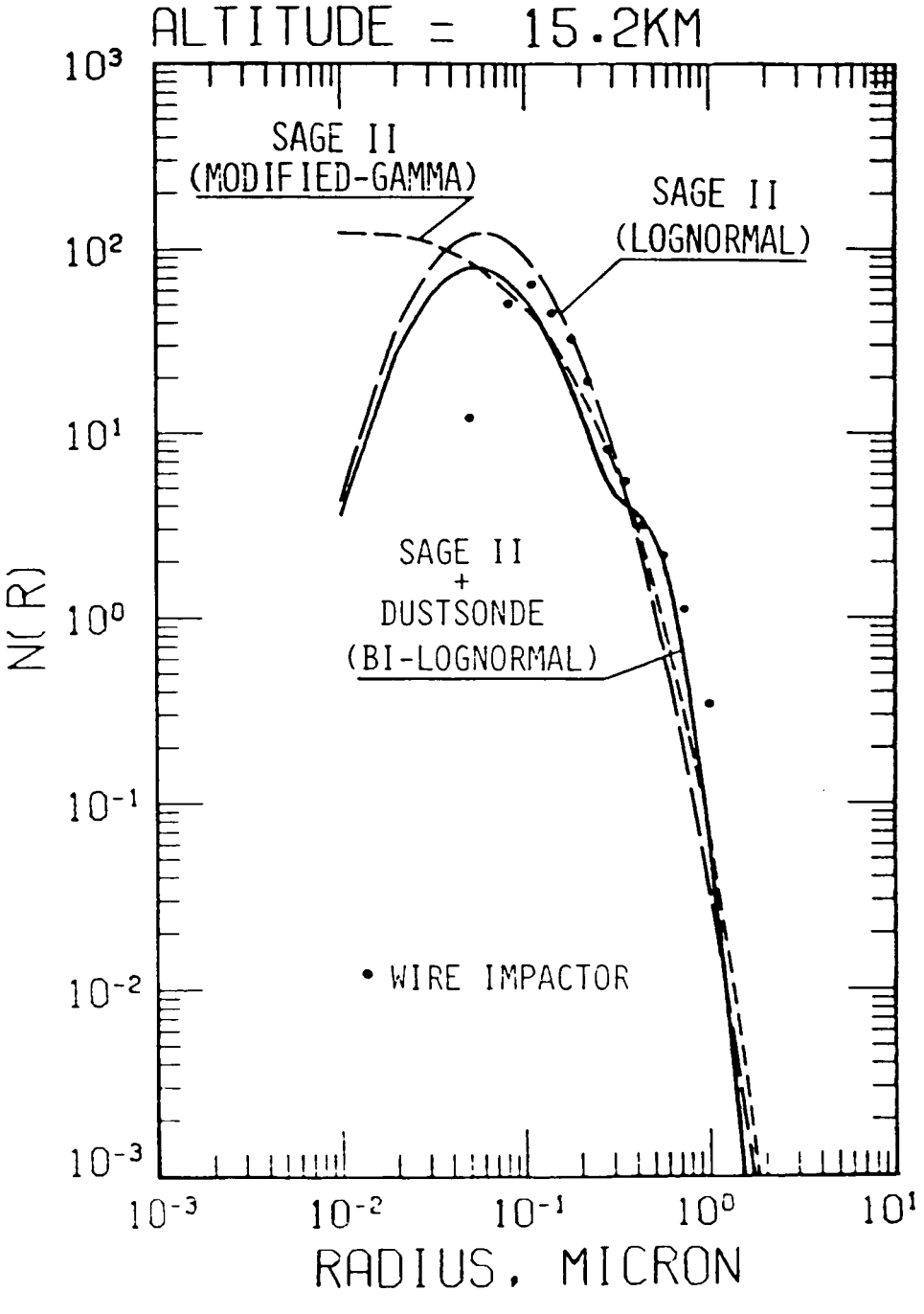


Figure 6.6a. Stratospheric aerosol size distributions derived from SAGE II aerosol extinctions at 15.2 km altitude.

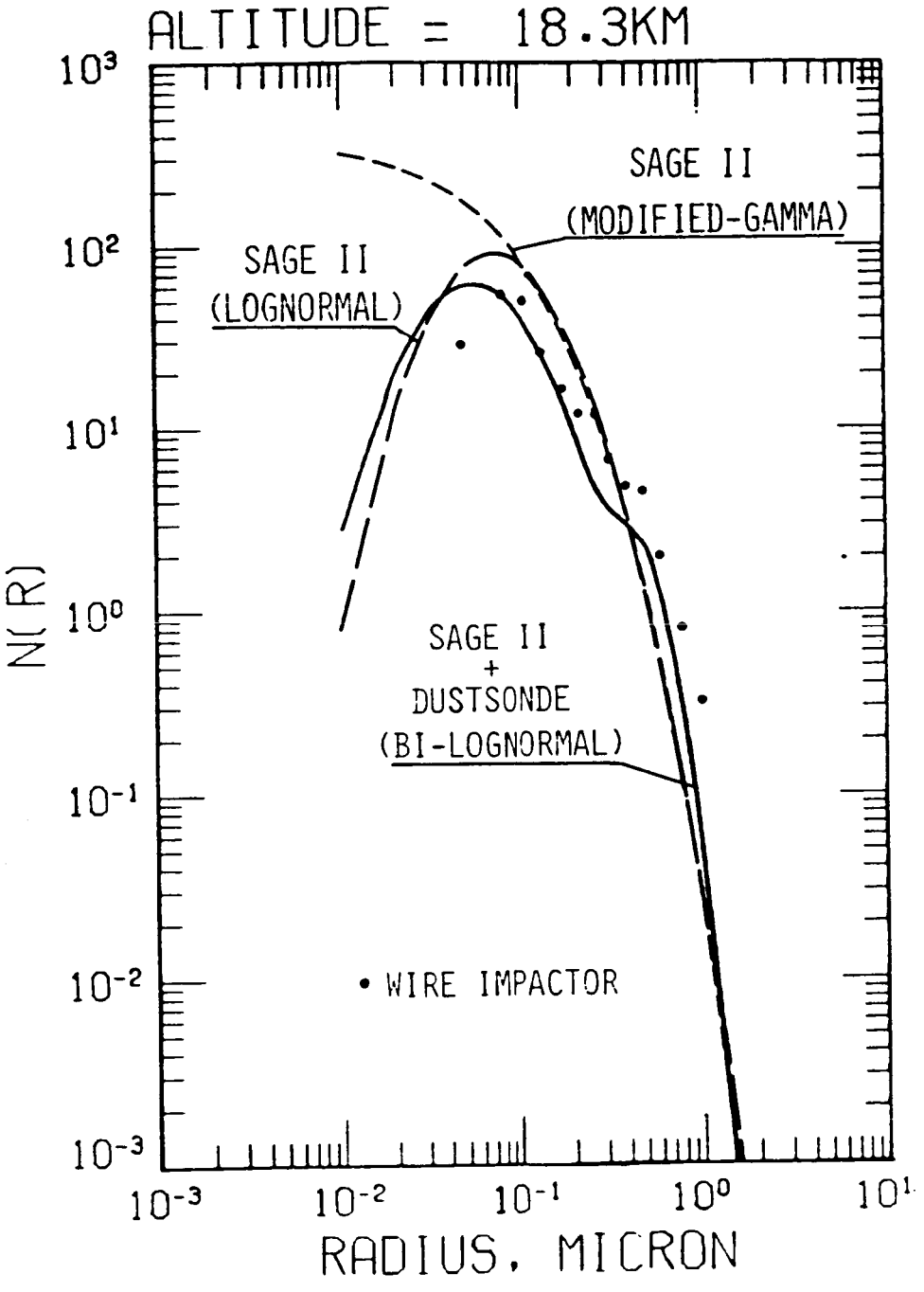


Figure 6.6b. Stratospheric aerosol size distributions derived from SAGE II aerosol extinctions at 18.3 km altitude.

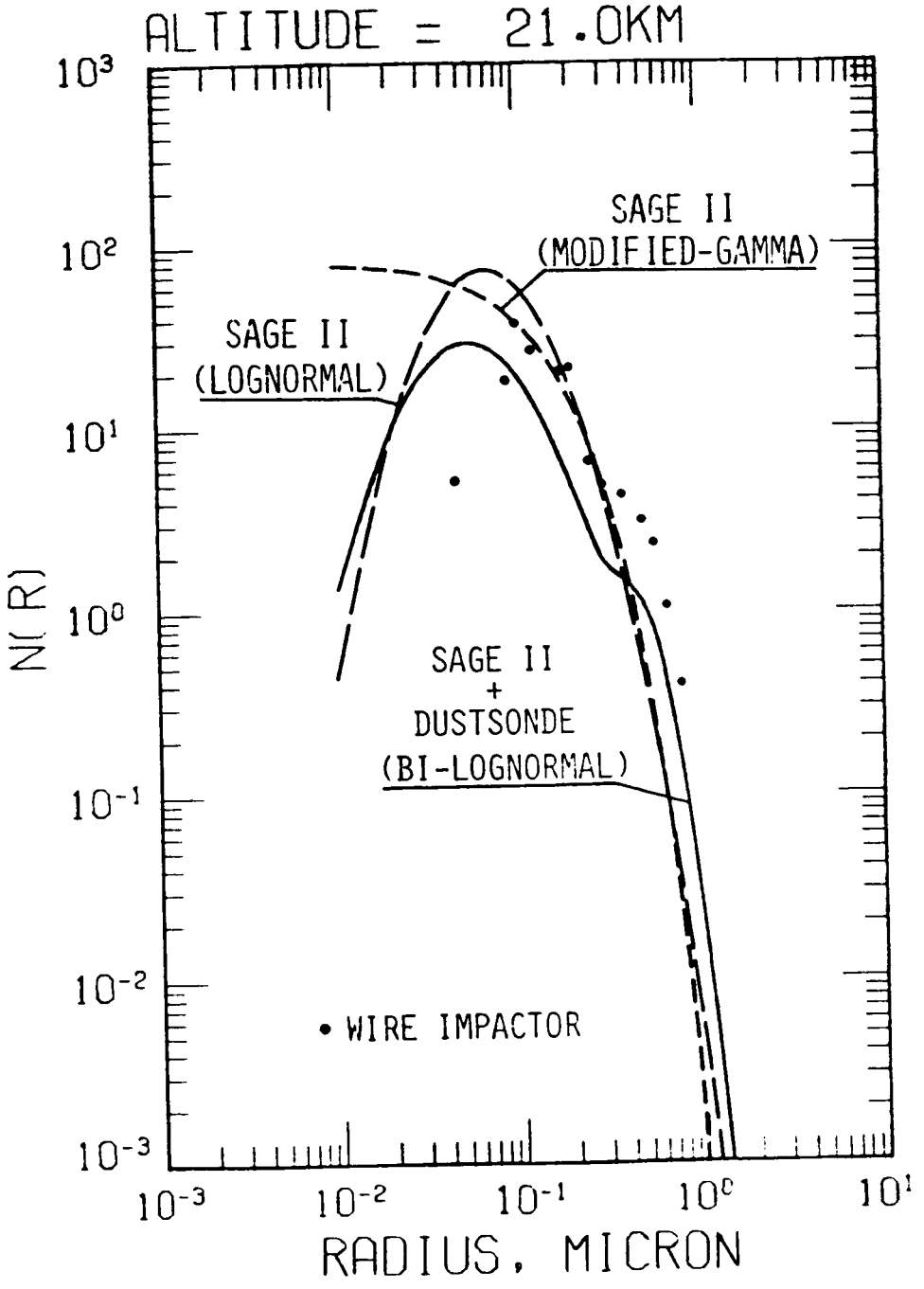


Figure 6.6c. Stratospheric aerosol size distributions derived from SAGE II aerosol extinctions at 21.0 km altitude.

with a measurable backscattered signal potentially obtainable from the mesosphere and even the lower part of the thermosphere. Although aerosols, in the form of noctilucent clouds, are known to exist in these higher regions, the main interest is in the variations in the molecular air density. These variations occur on a seasonal basis but, more importantly, are associated with the passage of atmospheric gravity waves, as well as tidal oscillations and turbulence.

As presently constituted, the 48" lidar system cannot achieve its maximum potential for high altitude measurements. It is desirable to incorporate a more powerful laser and also to convert the current analog measurements of backscattered light intensity to photon counting. In order to assist with the instrument upgrade, the science requirements for high altitude work have been examined and simulations have been made of potential system performance. As a basis for quantifying the science requirements, literature pertaining to atmospheric structure and changes in the height range 30-90 km has been reviewed. This information has been obtained by lidar (Kent et al., 1972; Kent & Keenliside, 1974; 1975; Chanin & Hauchecorne, 1981; Hauchecorne and Chanin, 1982; Chanin and Hauchecorne, 1984), rocket-borne instruments (Philbrick et al., 1980, 1983), and from Shuttle re-entry (Price, 1983). These techniques show large density excursions to be common, particularly in the upper part of the indicated height range. Based on this information, two levels of desirable system performance were defined for the lidar system. These are shown in Table 6.1. The first level is that which is necessary in order to demonstrate the lidar system capability and to resolve the largest atmospheric changes occurring within the mesosphere. The second

TABLE 6.1. Science Requirements for High Altitude Lidar

A. Minimum to Demonstrate Capability and Potential

Lidar system must be able to make density measurements to the following specifications:

| | |
|---|---|
| Height Range | 30-70 km |
| Vertical Resolution | 2 km |
| Integration Time | $\leq$ 1 hr |

| Altitude (km) | Required Accuracy |
|---|---|
| 30 | 1% |
| 40 | 1% |
| 50 | 2% |
| 60 | 5% |
| 70 | 10% |

B. Minimum for Useful Scientific Measurements

| | |
|---|---|
| Height Range | 30-90 km |
| Vertical Resolution | 1.5 km |
| Integration Time | $\leq$ 15 min |

| Altitude (km) | Required Accuracy |
|---|---|
| 30 | 1% |
| 40 | 1% |
| 50 | 1% |
| 60 | 1% |
| 70 | 2% |
| 80 | 3% |
| 90 | 5% |

level is that required for routine scientific measurements to improve our understanding of atmospheric dynamics at these altitudes. It should be noted that not only do the two tables differ in the measurement accuracy required, but also in the altitude resolution and, in particular, the integration time. Short integration times of the order of 15 minutes are required to resolve the higher frequency gravity wave oscillations. It is also desirable that measurements should be made throughout a 24-hour period but limitations to present lidar technology will almost certainly restrict the highest altitude measurements to night-time only.

Simulations of potential lidar performance have been carried out using the characteristics of the 48" lidar receiver, assuming photon counting, used together with one of two existing lasers or a third more powerful but potentially available laser. The results of these simulations are shown in Table 6.2 (using the existing Nd/YAG laser), Table 6.3 (using the existing Ruby laser), and Table 6.4 (using a more powerful Nd/YAG laser). Both Nd/YAG lasers are used at their second harmonics (0.53 μm) because of the much higher photomultiplier quantum efficiency available at that wavelength. Vertical resolution has been set at 2.0 km and integration times are either 600 or 3600 seconds. The levels of system performance shown in Tables 6.2, 6.3, and 6.4 may be compared to the science requirements shown in Table 6.1.

If we first examine Tables 6.2 and 6.3, we may compare the relative merits of two existing lasers. Although the single shot performance of the Nd/YAG system is not as good as that of the Ruby lidar, the integrated performance is superior at all altitudes. The only caveat to be applied to

TABLE 6.2. High Altitude Lidar Simulation

(A) SYSTEM PARAMETERS

Receiving Mirror Area - 1.00 $m^2$
Full Angle Beam Divergence - 0.100E-02 r
Wavelength - 0.6943E-06 m
Overall Efficiency - 0.02
Pulse Energy - 1.50 J
Firing Rate - 0.13 Hz
Filter Bandwidth - 0.100E-08 m
Photomultiplier Noise - 50.0 $s^{-1}$

(B) ATMOSPHERIC PARAMETERS

Atmospheric Transmission - 0.80
Sky Brightness = 0.70E+00 $R.A^{-1}$

(C) OPERATIONAL PARAMETERS

Height Increment - 1.0 km
Integration Time - 3600.0 s

System Constant - 0.224E+21 Sky Background = 0.117E-02

PM Background - 0.667E-03

| HEIGHT (KM) | SIGNAL COUNT | NOISE COUNT | % UNCERTNTY (ONE SHOT) | % UNCERTNTY (INTEGRATED |
|---|---|---|---|---|
| 5 | .274E+07 | .183E-02 | .060 | .003 |
| 10 | .385E+06 | .183E-02 | .161 | .008 |
| 15 | .806E+05 | .183E-02 | .352 | .017 |
| 20 | .150E+05 | .183E-02 | .816 | .038 |
| 25 | .597E+04 | .183E-02 | 1.294 | .061 |
| 30 | .190E+04 | .183E-02 | 2.292 | .108 |
| 35 | .643E+03 | .183E-02 | 3.943 | .186 |
| 40 | .232E+03 | .183E-02 | 6.559 | .309 |
| 45 | .904E+02 | .183E-02 | 10.519 | .496 |
| 50 | .382E+02 | .183E-02 | 16.174 | .762 |
| 55 | .175E+02 | .183E-02 | 23.922 | 1.128 |
| 60 | .801E+01 | .183E-02 | 35.346 | 1.666 |
| 65 | .359E+01 | .183E-02 | 52.757 | 2.487 |
| 70 | .157E+01 | .183E-02 | 79.777 | 3.761 |
| 75 | .660E+00 | .183E-02 | 123.217 | 5.809 |
| 80 | .268E+00 | .183E-02 | 193.670 | 9.130 |
| 85 | .106E+00 | .183E-02 | 309.973 | 14.612 |
| 90 | .393E-01 | .183E-02 | 515.907 | 24.320 |
| 95 | .145E-01 | .183E-02 | 882.017 | 41.579 |
| 100 | .532E-02 | .183E-02 | 1589.526 | 74.931 |

TABLE 6.3. High Altitude Lidar Simulation

(A) SYSTEM PARAMETERS

Receiving Mirror Area - 1.00 $m^2$
Full Angle Beam Divergence - 0.100E-02 r
Wavelength - 0.5300E-06 m
Overall Efficiency - 0.08
Pulse Energy - 0.15 J
Firing Rate - 2.50 Hz
Filter Bandwidth - 0.100E-08 m
Photomultiplier Noise - 50.0 $s^{-1}$

(B) ATMOSPHERIC PARAMETERS

Atmospheric Transmission - 0.70
Sky Brightness - 0.70E+00 $R.A^{-1}$

(C) OPERATIONAL PARAMETERS

Height Increment - 2.0 km
Integration Time - 3600.0 s

System Constant - 0.314E+20 Sky Background - 0.467E-02

PM Background - 0.667E-03

| HEIGHT (KM) | SIGNAL COUNT | NOISE COUNT | % UNCERTNTY (ONE SHOT) | % UNCERTNTY (INTEGRATED |
|---|---|---|---|---|
| 5 | .113E+07 | .534E-02 | .094 | .001 |
| 10 | .159E+06 | .534E-02 | .251 | .003 |
| 15 | .333E+05 | .534E-02 | .548 | .006 |
| 20 | .620E+04 | .534E-02 | 1.270 | .013 |
| 25 | .247E+04 | .534E-02 | 2.014 | .021 |
| 30 | .786E+03 | .534E-02 | 3.566 | .038 |
| 35 | .266E+03 | .534E-02 | 6.135 | .065 |
| 40 | .960E+02 | .534E-02 | 10.206 | .108 |
| 45 | .373E+02 | .534E-02 | 16.367 | .173 |
| 50 | .158E+02 | .534E-02 | 25.169 | .265 |
| 55 | .722E+01 | .534E-02 | 37.233 | .392 |
| 60 | .331E+01 | .534E-02 | 55.032 | .580 |
| 65 | .148E+01 | .534E-02 | 82.210 | .867 |
| 70 | .650E+00 | .534E-02 | 124.561 | 1.313 |
| 75 | .273E+00 | .534E-02 | 193.310 | 2.038 |
| 80 | .111E+00 | .534E-02 | 307.447 | 3.241 |
| 85 | .437E-01 | .534E-02 | 506.493 | 5.339 |
| 90 | .162E-01 | .534E-02 | 904.351 | 9.533 |
| 95 | .598E-02 | .534E-02 | 1778.390 | 18.746 |
| 100 | .220E-02 | .534E-02 | 3948.409 | 41.620 |

TABLE 6.4.High Altitude Lidar Simulation

(A) SYSTEM PARAMETERS

Receiving Mirror Area - 1.00 $m^2$
Full Angle Beam Divergence - 0.100E-02 r
Wavelength - 0.5300E-06 m
Overall Efficiency - 0.08
Pulse Energy - 0.40 J
Firing Rate - 10.00 Hz
Filter Bandwidth - 0.100E-08 m
Photomultiplier Noise - 50.0 $s^{-1}$

(B) ATMOSPHERIC PARAMETERS

Atmospheric Transmission - 0.70
Sky Brightness - 0.70E+00 $R.A^{-1}$

(C) OPERATIONAL PARAMETERS

Height Increment - 2.0 km
Integration Time - 600.0 s

System Constant - 0.837E+20  Sky Background - 0.467E-02

PM Background - 0.667E-03

| HEIGHT (KM) | SIGNAL COUNT | NOISE COUNT | % UNCERTNTY (ONE SHOT) | % UNCERTNTY (INTEGRATED |
|---|---|---|---|---|
| 5 | .302E+07 | .534E-02 | .058 | .001 |
| 10 | .424E+06 | .534E-02 | .154 | .002 |
| 15 | .888E+05 | .534E-02 | .336 | .004 |
| 20 | .165E+05 | .534E-02 | .778 | .010 |
| 25 | .658E+04 | .534E-02 | 1.233 | .016 |
| 30 | .210E+04 | .534E-02 | 2.184 | .028 |
| 35 | .708E+03 | .534E-02 | 3.757 | .049 |
| 40 | .256E+03 | .534E-02 | 6.250 | .081 |
| 45 | .996E+02 | .534E-02 | 10.022 | .129 |
| 50 | .421E+02 | .534E-02 | 15.411 | .199 |
| 55 | .193E+02 | .534E-02 | 22.795 | .294 |
| 60 | .882E+01 | .534E-02 | 33.683 | .435 |
| 65 | .396E+01 | .534E-02 | 50.287 | .649 |
| 70 | .173E+01 | .534E-02 | 76.083 | .982 |
| 75 | .728E+00 | .534E-02 | 117.666 | 1.519 |
| 80 | .296E+00 | .534E-02 | 185.551 | 2.395 |
| 85 | .117E+00 | .534E-02 | 299.436 | 3.866 |
| 90 | .433E-01 | .534E-02 | 509.207 | 6.574 |
| 95 | .160E-01 | .534E-02 | 914.612 | 11.808 |
| 100 | .586E-02 | .534E-02 | 1805.101 | 23.304 |

these results is in connection with the atmospheric transmission and, in particular, the background sky brightness. The values assumed correspond to good, low-light seeing conditions. Local measurements of these quantities at the 48" lidar site do not exist and may well not approach these optimum values. The performance figures for the Nd/YAG system may also be compared to the science requirement figures given in Table 6.1. It can be seen that level A (minimum to demonstrate capability and potential) is easily attained with a considerable safety factor. Level B (minimum for useful scientific measurements) is not attained (allow for different integration times), indicating the desirability of replacing the existing Nd/YAG laser by a more powerful model. Table 6.4, based on the performance of a better Nd/YAG laser may be compared with the figures for required accuracy in the second part of Table 6.1. The two tables have slightly different spatial and temporal integration widths (1.5 km versus 2 km and 600 S versus 900 S), the overall effect of this is, however, fairly minor. It can be seen that an upgraded 48" system will meet the science requirements at all altitudes up to 80 km and comes close to the requirement at 90 km altitude (6.6% versus 5.0% accuracy). Once again, the caveat concerning atmospheric transmission and sky brightness must be considered. It should also be noted that these science requirements do not address the subject of daytime measurements. These are desirable scientifically and are possible up to a somewhat lower altitude given substantial modifications to the receiving optics of the 48" lidar system. Work carried out under a separate contract (NAS1-17072) shows that on upgraded systems, using an interference filter to reject unwanted sky background, could make measurements with 10% accuracy (for 10-minute

integration period) up to about 60 km. Use of a narrow-band Fabry-Perot etalon might enable this limit to be extended up to about 75 km.

### 6.3 Forty-eight Inch Lidar Receiver Modification

As part of the work of modifying the 48" lidar receiver for the high altitude studies discussed in Section 6.2, a detailed analysis was made of the lidar receiver optics. The basic purpose of the analysis was to find a suitable way to incorporate a photon counting photomultiplier together with a high-speed rotating shutter. The latter is required to reduce, or eliminate, the signal induced noise in the photomultiplier caused by the initial, high intensity, backscattered signal from the lower atmosphere. The shutter, which screens the photomultiplier during the first 100-200 microseconds after the laser is fired is driven by a high-speed synchronous motor. Figure 6.7 shows part of the existing optical system of the laser receiver, together with the proposed shutter/photon counting assembly. Collimating lens A is part of the existing system, lens B is required to focus the beam to a small diameter at the shutter itself. Figure 6.8 shows a scale drawing of a possible design for the shutter assembly. Final dimensions may change slightly, contingent upon the choice of shutter motor and any other changes made to the optical system.

In the course of examining the optical system, it was noticed that the collimating lens (lens A in Fig. 6.7) was not of sufficient diameter to pass all nonaxial rays. Its diameter is 1.75", exactly the same as that of the telescope exit pupil. Loss of light at this lens occurs (shown by the two outlying rays in Fig. 6.7) becoming increasingly serious for greater beam

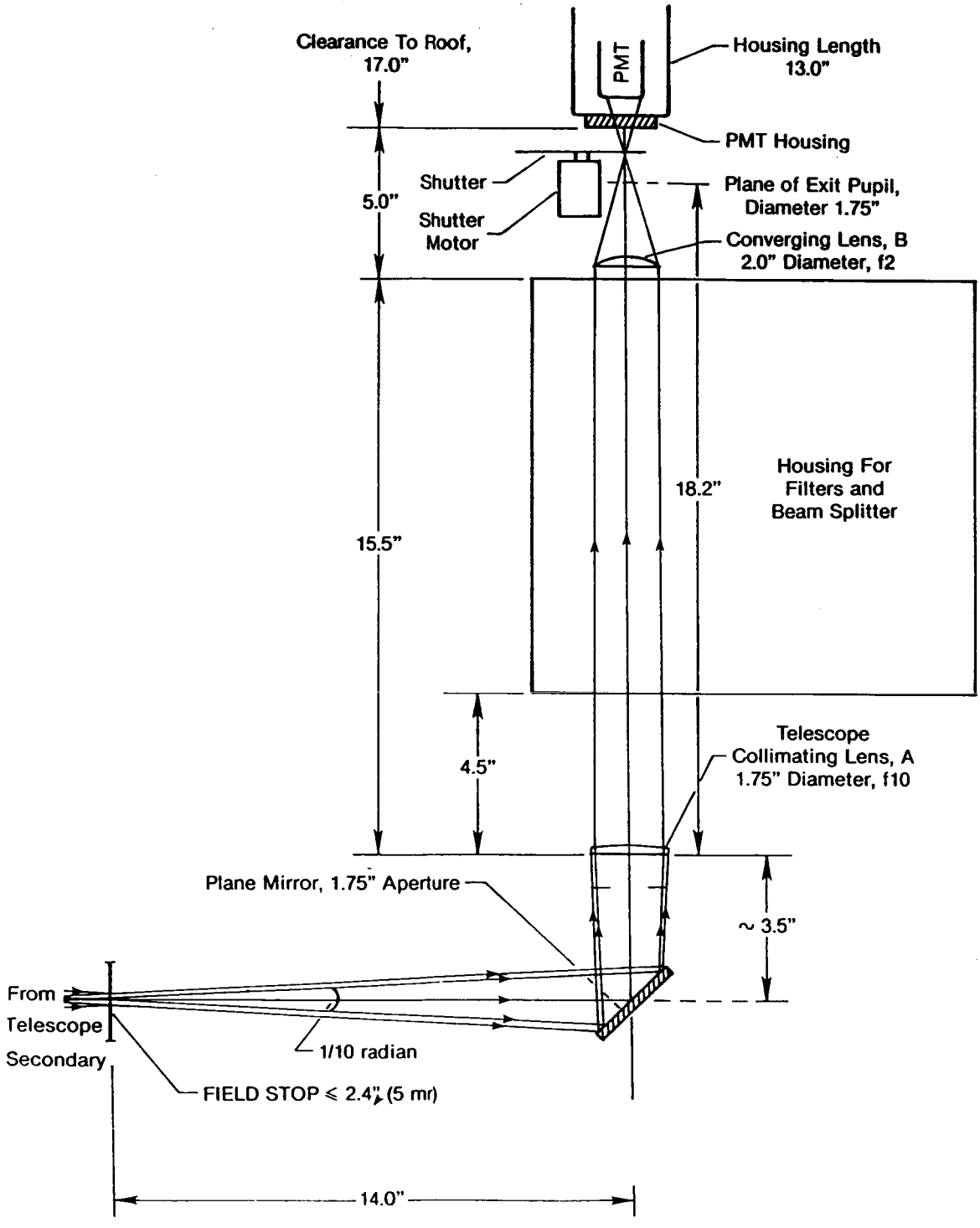


Figure 6.7. Optical diagram of part of the receiver optics of the 48" lidar system. The shutter and photon counting assembly are planned additions to the system.

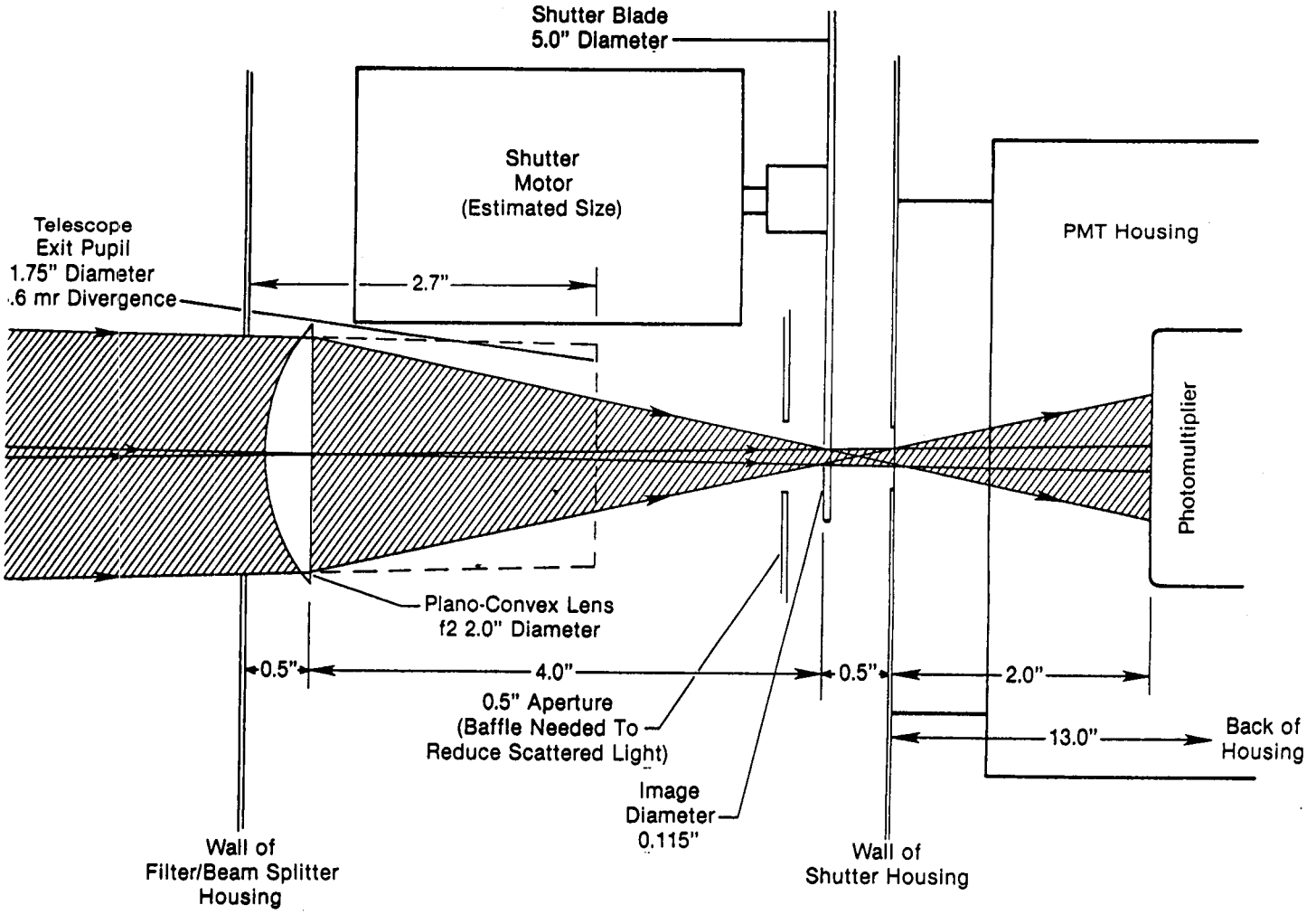


Figure 6.8. Diagram of a possible arrangement for the high speed shutter/photon counting assembly.

divergencies. That this loss actually took place was confirmed by measurement of the beam diameter on the telescope itself using the sun as a source and varying the size of the aperture stop. Correction of this fault appears at first sight to be simply a matter of replacing the collimating lens by one of equal focal length and larger diameter. This, although theoretically correct, raises other practical problems. The first is that the turning mirror would also have to be replaced by one of greater diameter. The second and more important problem is that, after passing the collimating lens, the beam passes through one or more interference filters. The standard diameter for these is 2.0". For angular divergences greater than about 0.5 mr, these filters will also vignette the beam. A simple lens of shorter focal length placed closer to the field stop would solve these problems but the optimum location is at or very close to the turning mirror making the solution practically difficult. The solution chosen is to replace the collimating lens by two lenses as shown in Fig. 6.9. In this figure, the two new lenses and the path of an edge beam is shown as an overlay on the original diagram (Fig. 6.7). In the new optical arrangement, the system will pass all the light out to a beam divergence (total angle) of 2.0 mr. The collimating lenses have diameters of 2.0" and focal lengths of 20.0" and 27.5", respectively. The turning mirror does not need to be replaced and the second collimating lens is placed at the location of the current collimating lens. The resultant beam following the collimater is sufficiently narrow to pass through the interference filters and the entrance lens of the proposed shutter assembly.

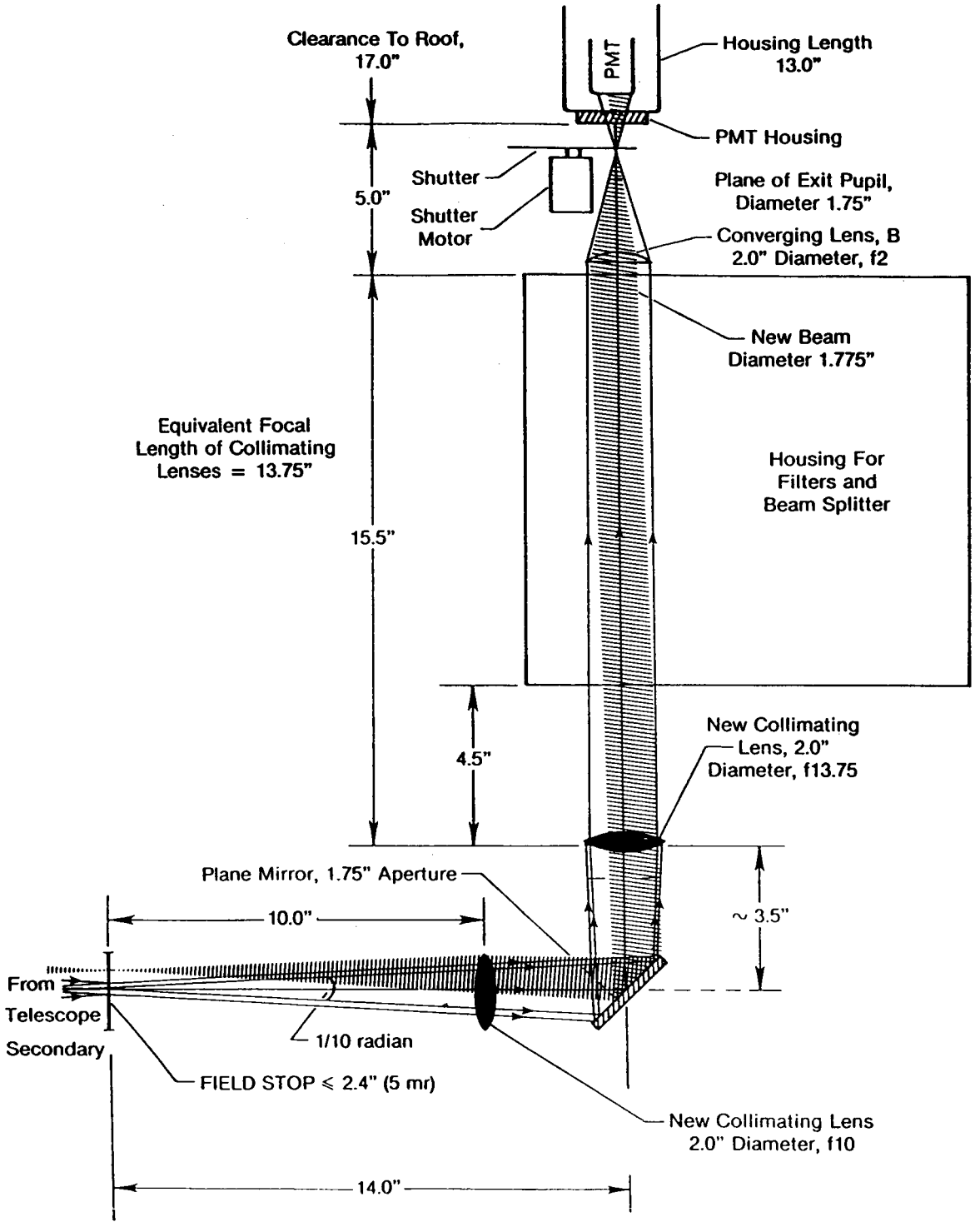


Figure 6.9. Diagram showing possible modification to the 48" lidar receiver to correct for loss of radiation. Two new lenses are shown in black, the path of an edge ray by cross-hatching.



C-2

# 7. TASK 6--INVESTIGATE STRATOSPHERIC PLANETARY WAVES AND THEIR EFFECT ON TRANSPORT OF AEROSOLS, $O_3$, WATER VAPOR AND $NO_2$

## 7.1 Aerosols As Dynamic Tracers and Association with Planetary Wave Activity

Previous work carried out by Kent et al. (1985), has shown how the SAM II 1 μm extinction ratio may be used as a tracer for atmospheric movements associated with the north polar vortex. A similar study has been made on the use of the corresponding extinction ratios obtained from SAGE I and preliminary SAGE II data. Examination of extinction ratio profiles from different latitudes show that it is, in general, possible to classify these as a low-latitude type (layer maximum at about 25 km or above) or a middle or high latitude type (layer maximum at 15-20 km). At certain times of the year, however, some low latitude-type profiles are observed at high latitudes. Examples of these profiles obtained with the SAGE I satellite are shown in Figure 7.1. Figure 7.1(a) is an example of a "normal" middle or high latitude extinction ratio profile. Figure 7.1(b) shows a quite different profile, although it was obtained at the same latitude and on the same day. The latter profile is, in fact, similar to profiles normally seen within about $20^{o}$ of the equator. Examination of 11 months of SAGE I data, taken prior to major volcanic eruptions, shows a very clear seasonal cycle in the occurrence of "low-latitude type" layers outside the equatorial belt. Table 7.1 shows how the frequency of occurrence varies in both hemispheres with season. The occurrence is clearly a winter-time phenomenon; in summer, in both hemispheres, very few cases are observed. The most obvious explanation for this happening is that we are observing transport of low latitude aerosol

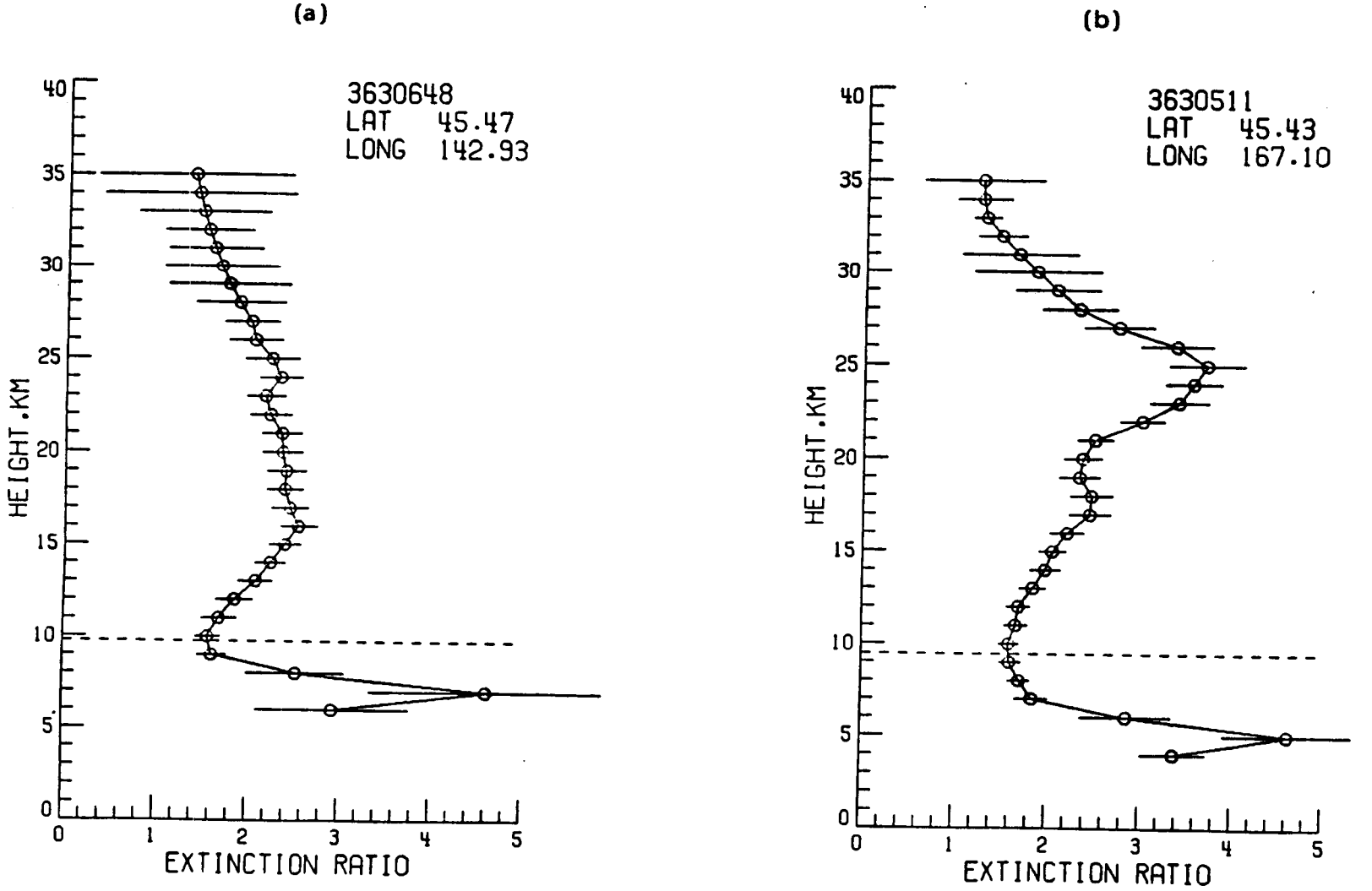


Figure 7.1. Extinction ratio profiles observed by SAGE I in December 1979 at a wavelength of 1 um.

(a) Normal, middle or high latitude profile

(b) "Low latitude type" profile

TABLE 7.1. Frequency of Observation of "Low Latitude Type" Extinction Ratio Profiles: February - December 1979, SAGE I Data.

| Month | Latitude Band | | |
|---|---|---|---|
| | 90°S - 30°S | 30°S - 30°N | 30°N - 90°N |
| January 1979 | – | – | – |
| February 1979 | 2.2% | – | 18.0% |
| March 1979 | 6.2% | 74.6% | 13.9% |
| April 1979 | 5.5% | 87.4% | 15.4% |
| May 1979 | 14.0% | 75.3% | 0.4% |
| June 1979 | 31.8% | 79.1% | 0.0% |
| July 1979 | 27.7% | 100.0% | 0.0% |
| August 1979 | – | 95.6% | 5.1% |
| September 1979 | 10.9% | 61.0% | – |
| October 1979 | – | 87.0% | 5.0% |
| November 1979 | 4.3% | 100.0% | 16.7% |
| December 1979 | 1.2% | 82.1% | 25.4% |

A dash indicates that no data are available.

into the winter hemisphere; this is a time of planetary wave activity and of the existence of the polar night vortex with its associated subsidence.

The same phenomenon manifests itself in a similar form in the SAGE II data. The basic SAGE II extinction ratio profiles show much higher values of the extinction ratio due to the presence of material from the El Chichon eruptions. The "normal" layer at high latitudes has a peak extinction ratio of about 10 and a fairly flat layer top between 20 and 25 km. An example of this is shown in Figure 7.2(a). As in the case of SAGE I, anomolous layers also appear during the winter season. A typical example is shown in Figure 7.2(b) where a secondary peak occurs at an altitude of about 27 km. These layers are observed in both hemisphere and, in as far as it is possible to see in the limited preliminary SAGE II data set, have a seasonal cycle similar to that observed with SAGE I. A detailed study has been made of the preliminary SAGE II extinction data between October 1984 and May 1985 and the following general characteristics of these anomalous layers determined. Part of this work has been presented at the Sixth Conference on Atmospheric Radiation, Williamsburg, Virginia May 12-16, 1986 (Kent, 1986).

**1. Altitude of Occurrence**

The effects are most visible at altitudes of 24-27 km. This is determined mostly by the relative shapes of the high latitude aerosol layer, where the "anomalies" appear, and the low latitude aerosol layer from which they are supposed to be derived. The exact altitude range is still uncertain, but there appears to be a change in behavior at an altitude of around 22 km. In order to illustrate this change, Figure 7.3 shows mean

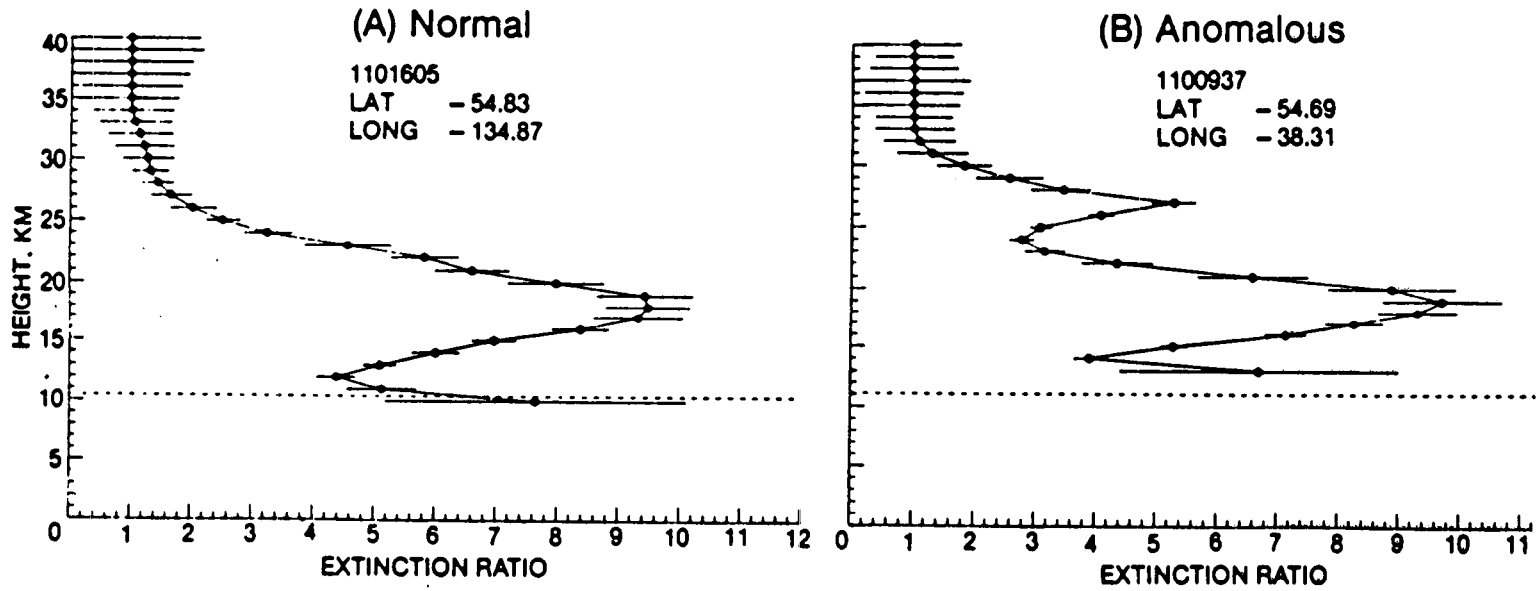


Figure 7.2. High latitude SAGE II extinction ratio profiles, April 20, 1985.

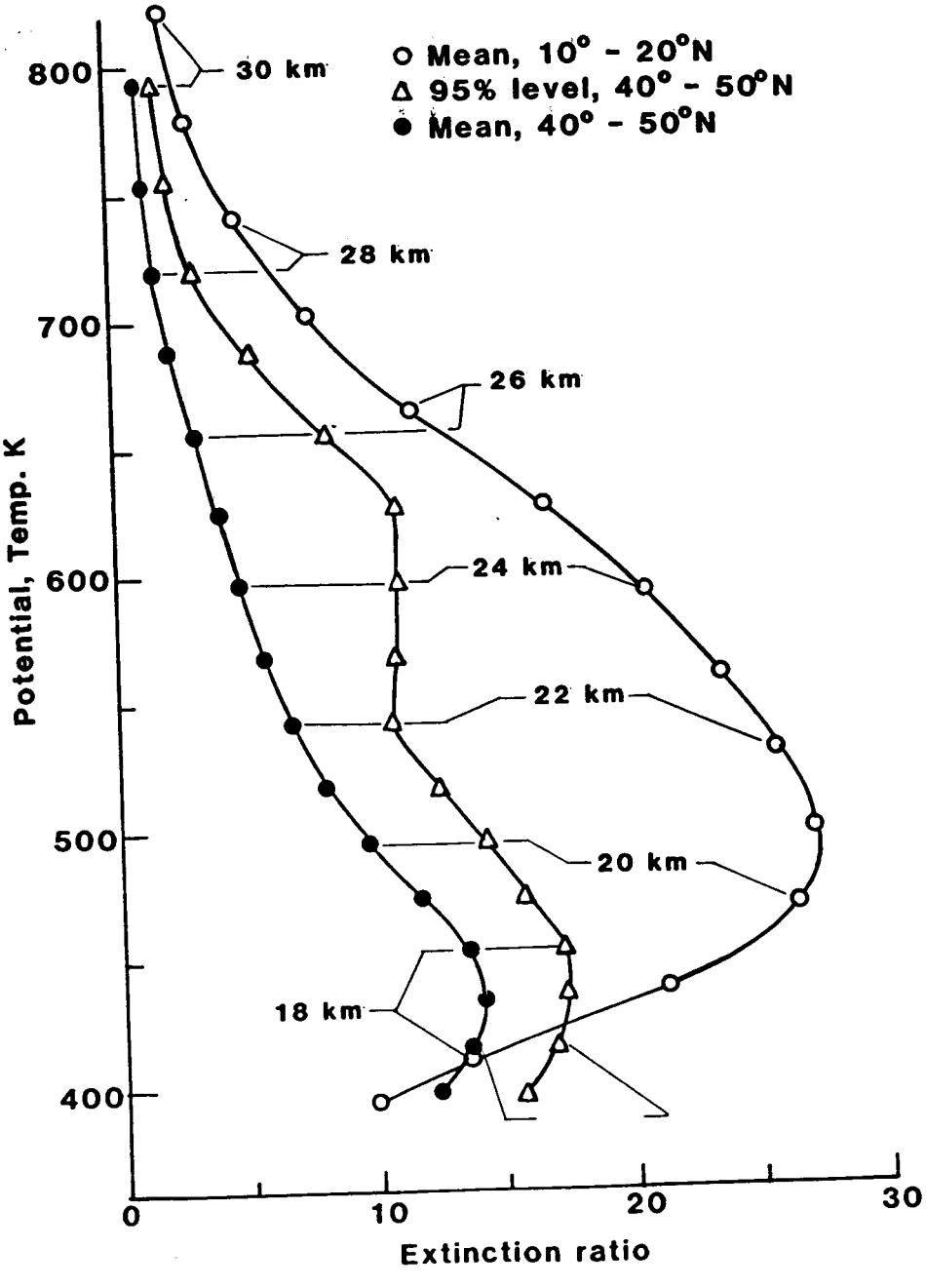


Figure 7.3. SAGE II extinction ratio profiles, November 4 - December 6, 1984.

aerosol extinction ratio profiles for two separate latitude bands during the period November 4 - December 6, 1984. The extinction ratio profiles are plotted in terms of potential temperature rather than altitude (the altitudes are marked on the figure). It can be seen that at all altitudes above about 16 km, the low latitude aerosol has a much higher mean extinction ratio. The figure also shows a third curve derived from the spread in aerosol characteristics at $40^{\circ}$-$50^{\circ}$. The meaning of this third curve is best explained by reference to Figure 7.4. This figure shows the probability distribution of extinction ratio values at an altitude of 25 km, the same latitude band of $40^{\circ}$-$50^{\circ}$N and for the period November 9-20, 1984. Most extinction ratios have a value of 4 or less, but there is a "tail" of high values extending up to an extinction ratio of 16. These values are the ones attributable to material transported from low latitudes. In order to describe this tail, we have chosen the 95 percent probability level as a representative value. This is shown in Figure 7.4 and also in Figure 7.3, as a function of potential temperature (and altitude). The interesting feature in Figure 7.3 is the slope discontinuity between 22 and 25 km. Two possible explanations exist for this change.

a. Less material is transported from low to high latitudes at altitudes below 22 km as compared to the higher altitudes, or

b. Material is transported at all levels but is more rapidly mixed into the background below about 22 km.

**2. Longitudinal Characteristics**

At or near 25 km, the occurrence of high extinction ratios is periodic with longitude. Wave 1 and Wave 2 structure is clearly evident and this is

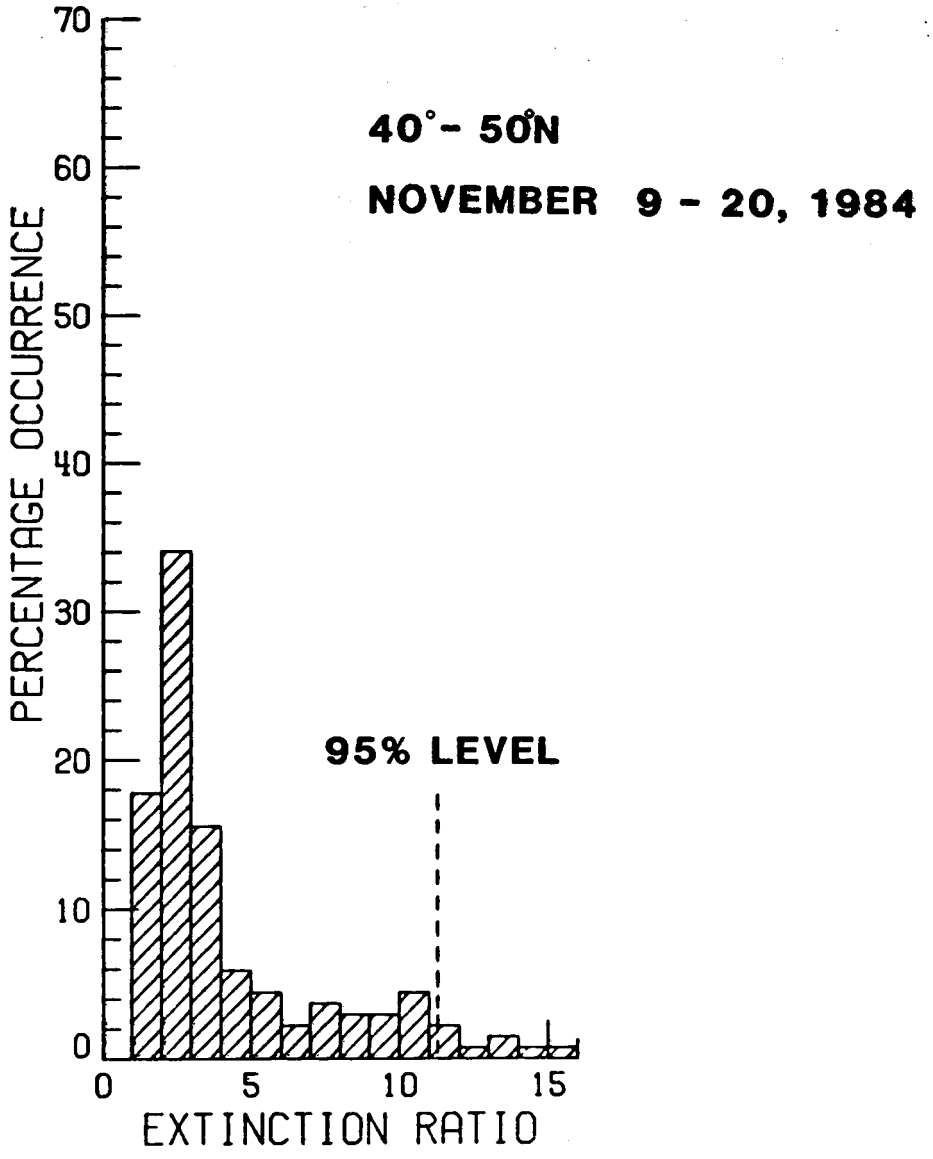


Figure 7.4. Probability distribution of extinction ratios at an altitude of 25 km.

correlated with the structure in the 30 mb pressure-altitude field. An example of the correlation is shown in Figure 7.5(a) and (b). Figure 7.5(a) shows the location of SAGE II measurements on November 13-15, 1984. The location of the largest extinction ratios is shown in black, the smallest by clear open circles. Figure 7.5(b) shows the 30 mb meteorological analysis map for November 14, 1984. The dominant features are the polar low and an elongated high pressure region over Japan. Comparison of 7.5(a) with 7.5(b) shows that the anomalously high values of extinction ratio occur to the north of the high pressure region where one might expect to find them on the theory of transport from low latitudes. This correlation is also evident over a longer period, as is shown in Figure 7.6. This figure shows the mean cross-correlation between the 24 km extinction ratio and the 30 mb pressure altitude for a period of about one month. The latitude range is approximately $30^{\circ}$ to $50^{\circ}$N. Maximum correlation of about 0.5 occurs at zero longitudinal shift. The periodic nature of the function is evident as is also a bias to a westerly longitudinal shift. Figure 7.6 shows the correlation function transformed to give the cross-spectral power density; almost all the power is in the first three planetary wave numbers. For the first two, there is a phase shift to the west. This is consistent with the occurrence of a net eddy transport of material from low to high latitudes by these waves.

### 3. The Magnitude of the Extinction Ratios

At the 25 km level between October and December 1984, the normal extinction ratio between $40^{\circ}$ and $50^{\circ}$N was 4 or less. Anomalous values up to 19 were observed. Such values are commonly observed at the same altitude in

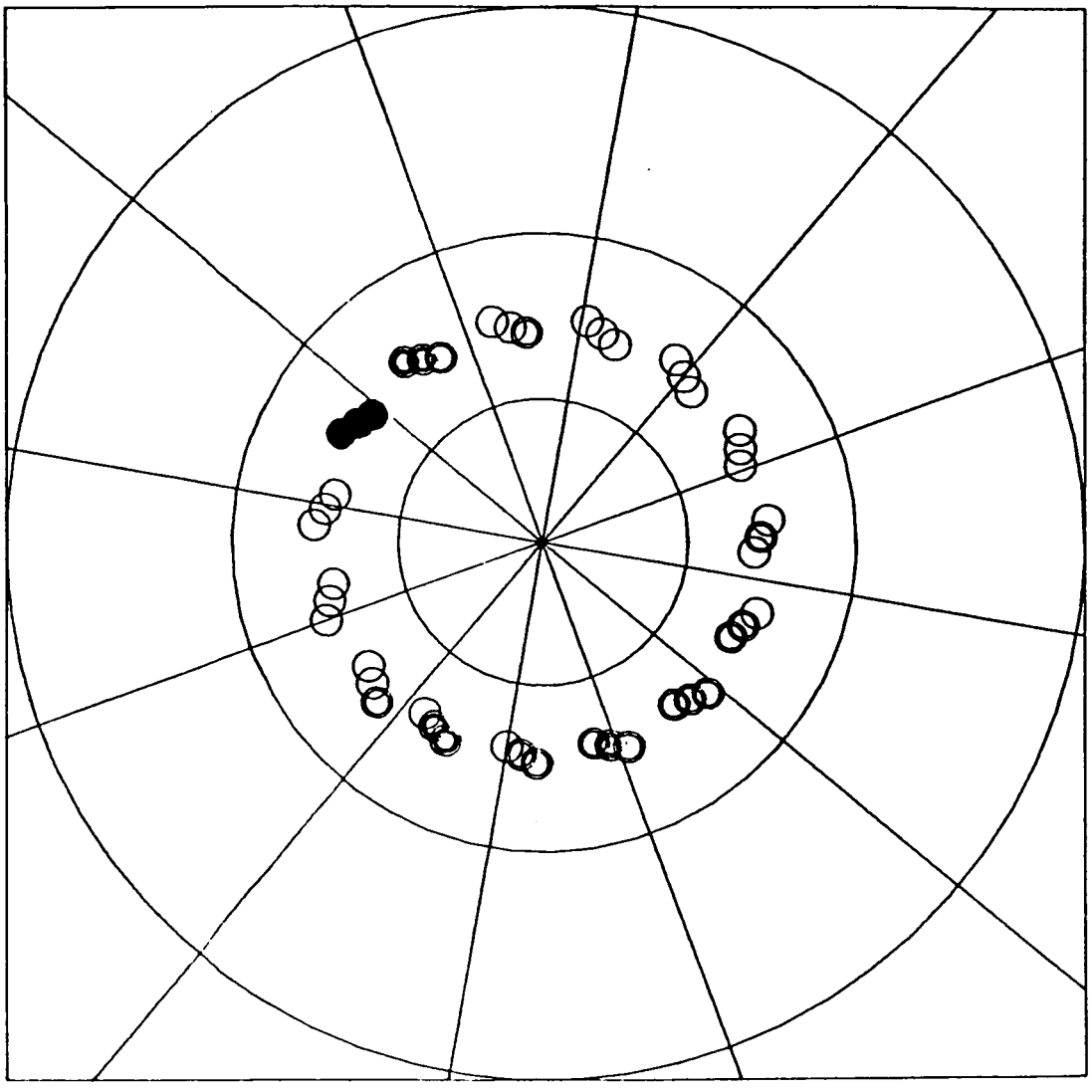

Figure 7.5a. SAGE II extinction ratios, 24 km altitude, November 13-15, 1984.

Extinction Ratio Key: <4, 4-8, 8-12, >12

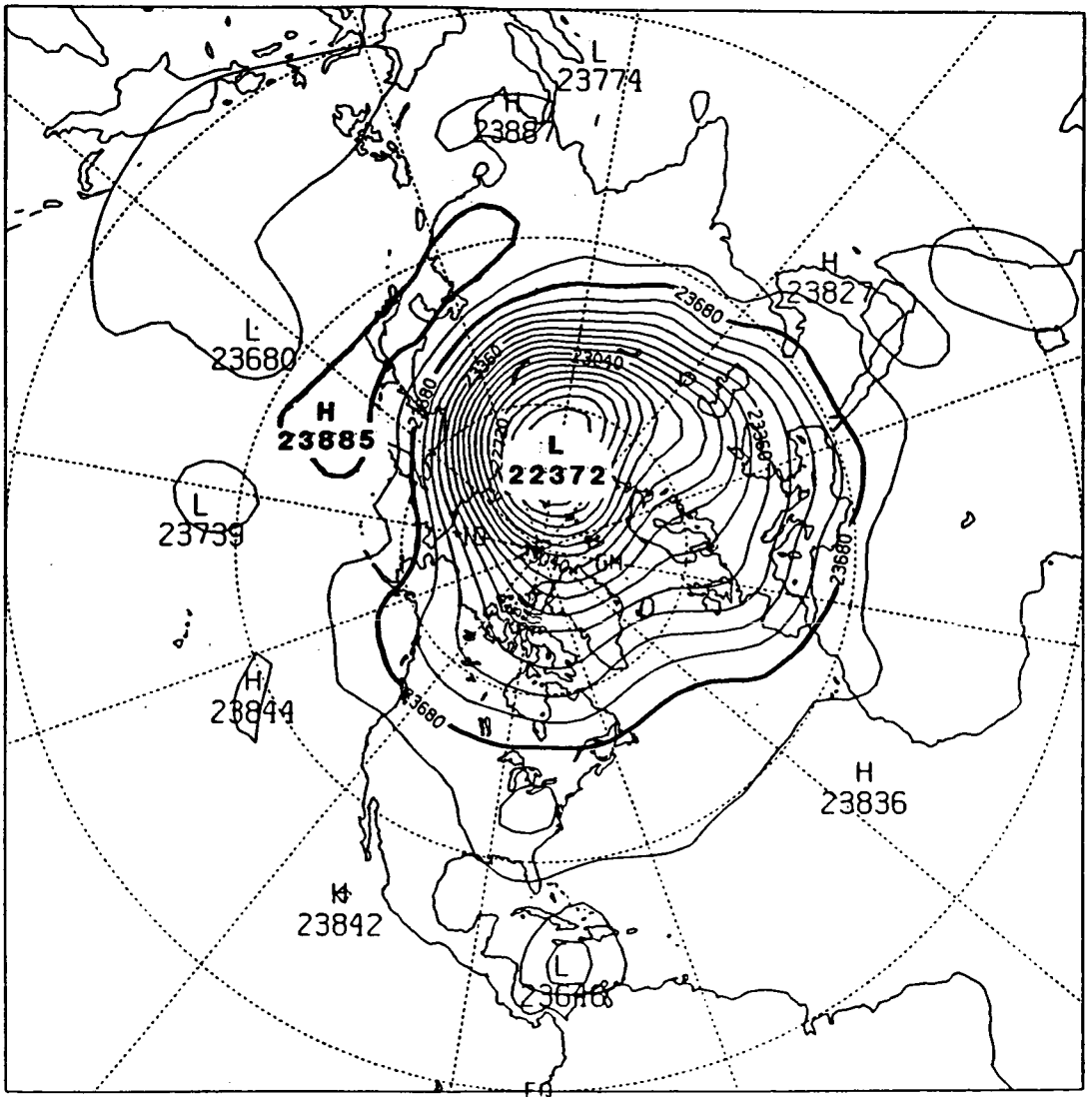


Figure 7.5b. 30 mb meteorological analysis map, November 14, 1984

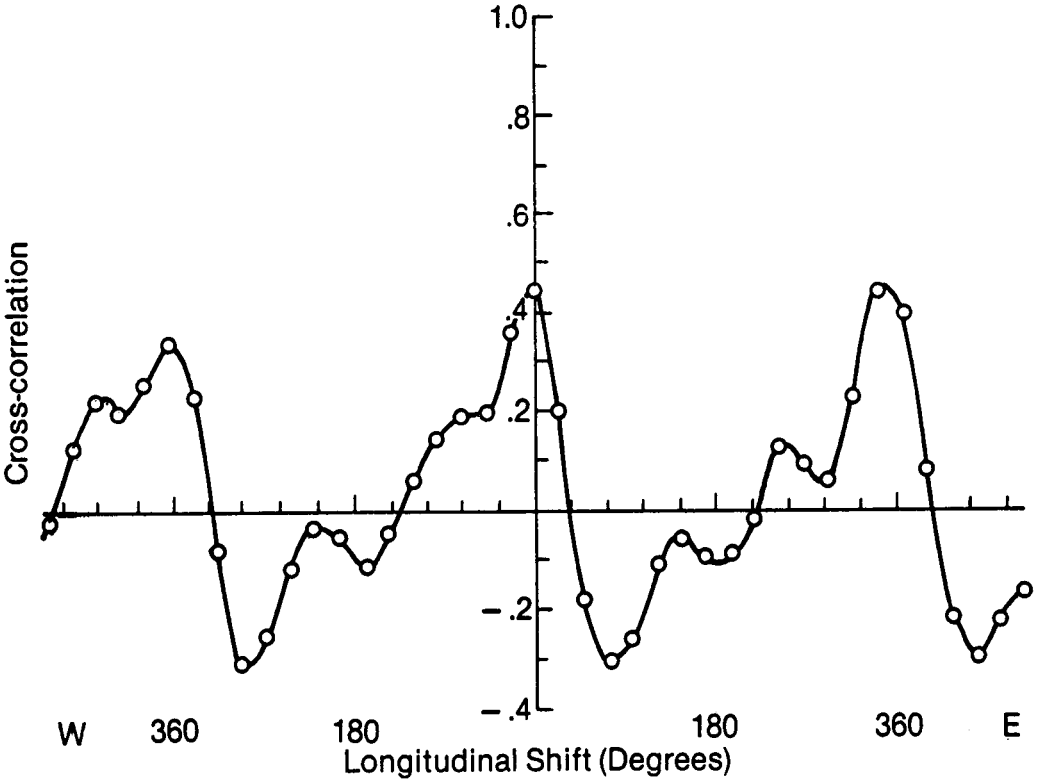


Longitudinal shift is that of the extinction ratio sampling location relative to that of the pressure altitude sampling location.

Figure 7.6(a). Mean cross-correlation, November 7 - December 3, 1984 (24 km extinction ratio vs. 30 mb pressure altitude).

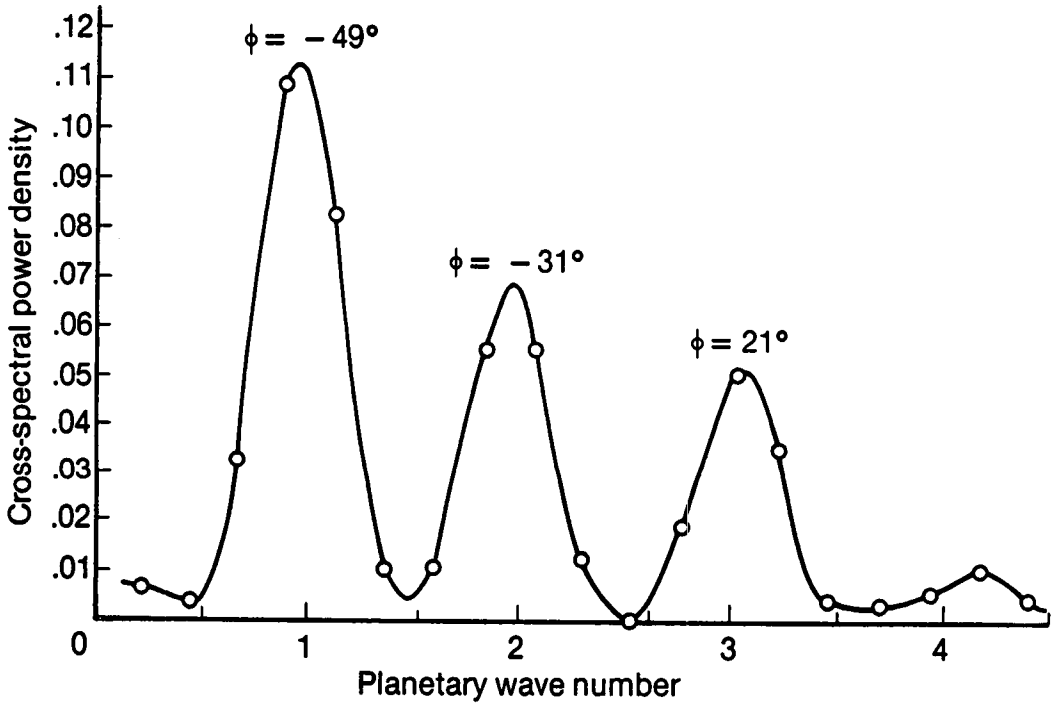


Phase values give the longitudinal shift (degrees East) of the extinction ratio relative to the pressure altitude.

Figure 7.6(b). Cross-spectral power density, November 7 - December 3, 1984 (24 km extinction ratio vs. 30 mb pressure altitude).

low latitudes (10-20°N) during the same time period. (See Figures 7.3 and 7.4.)

**4. Slope of Isentropic Surfaces**

Assuming that material is transported from low latitudes by planetary wave activity, it is likely that it will remain on a surface of contrast potential temperature. Thus, material origination at 20 km at 15°N will reach 45°N at an altitude of about 19 km, material at 25 km will suffer little height change, while material originating at 30 km will ascend to an altitude of about 31 km. The detailed relationship has already been shown in Figure 7.3.

**5. Seasonal Characteristics**

In the northern hemisphere, the phenomenon is limited to the period October 1984 - March 1985, the aerosol layer returning to normal in April, May, 1985. This agrees with the SAGE I data. In the southern hemisphere, the seasonal variation is similar but the period of absence of anomalous layers is much shorter, extending only from January through March, 1985. Again, this is in agreement with the SAGE I data and reflects the longer period of planetary wave activity in the southern hemisphere. It may be noted that SAGE I data indicate that there can be considerable year-to-year variation in both hemispheres.

**6. Relationship to Planetary Wave Activity**

A study has been made of the amount of aerosol transport as a function of time in the northern hemisphere from October 1984 - May 1985. Figure 7.7

shows histograms of the extinction ratio values for the latitude band 40-50°N for each satellite crossing period. Anomalous values, corresponding to extinction ratios of 4.0 or greater, are shown in black. The build up in activity from October to early January is clear; this was followed by a completely clear period, then a minor reoccurrence and a final disappearance in April 1985. The clear period in January is unexpected and corresponds to the time period following an unusual major sudden warming. A preliminary analysis of the variation in eddy transport during this period, made by Labitzke and co-workers at the Free University of Berlin (Labitzke et al., 1985), shows a disappearance of planetary wave activity in the second part of January followed by a weak reestablishment of the polar vortex in February-March, 1985. This behavior, which is shown in Figure 7.8, corresponds very well with that of the satellite extinction data.

## 7. Other Effects

The recently discovered height error in the preliminary SAGE II sunrise data has injected an altitude uncertainty of the order of 1 km into that half of the analyzed data set. Re-analysis of this portion will be required after this error is corrected.

Apart from the above, which is an error, there appears to have been an altitude change taking place over much of the northern hemisphere in the height of the top-side of the aerosol layers. This results in a steady drop, from October 1984 to January 1985, of the aerosol concentration at altitudes near 30 km. This effect requires further study.

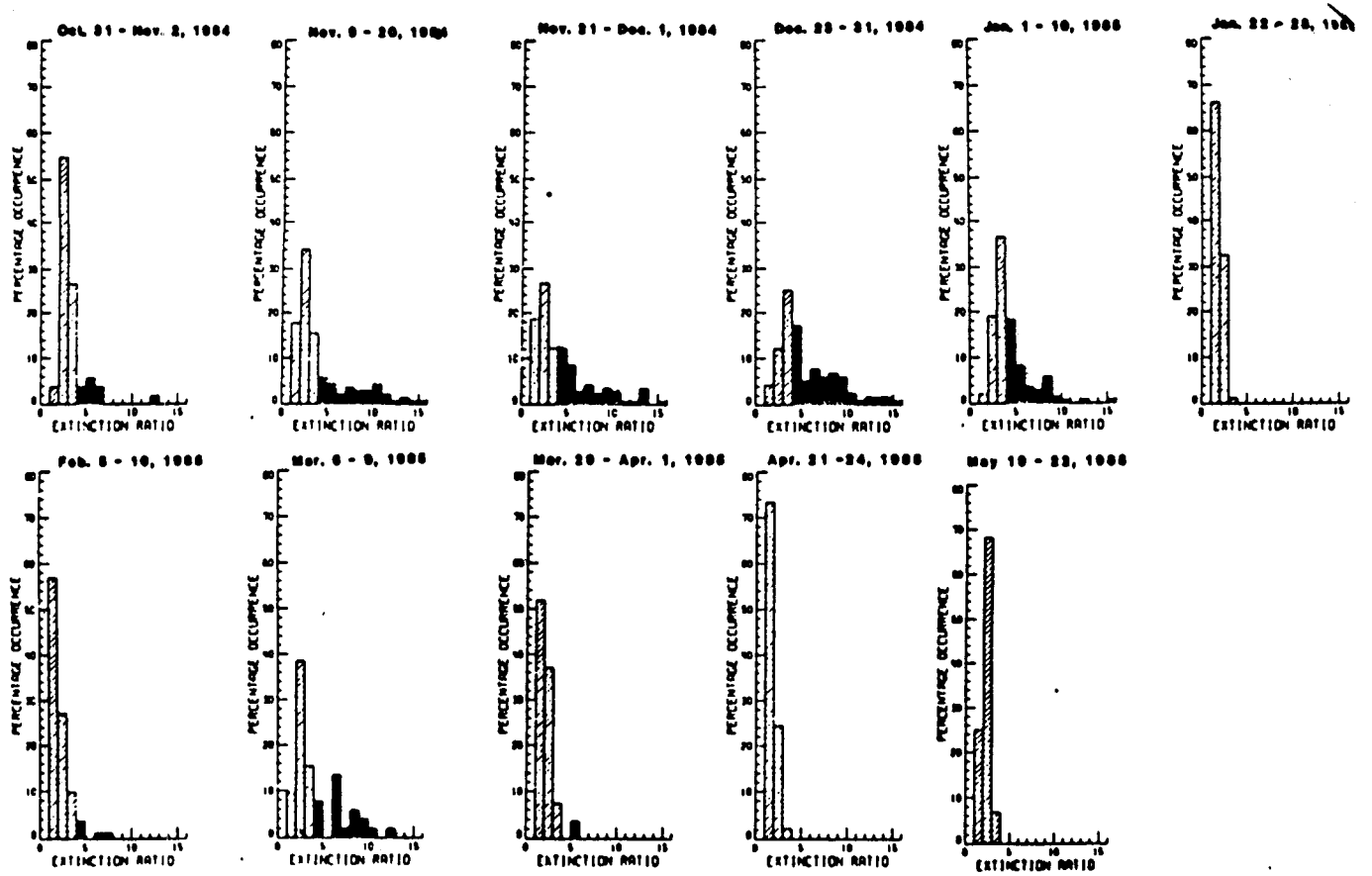


Figure 7.7. Probability distribution of 1 μm extinction ratios at an altitude of 25 km and 40° - 50°N, October 1984 - April 1985. Anomalous values (extinction ratios >4) are shown in black.

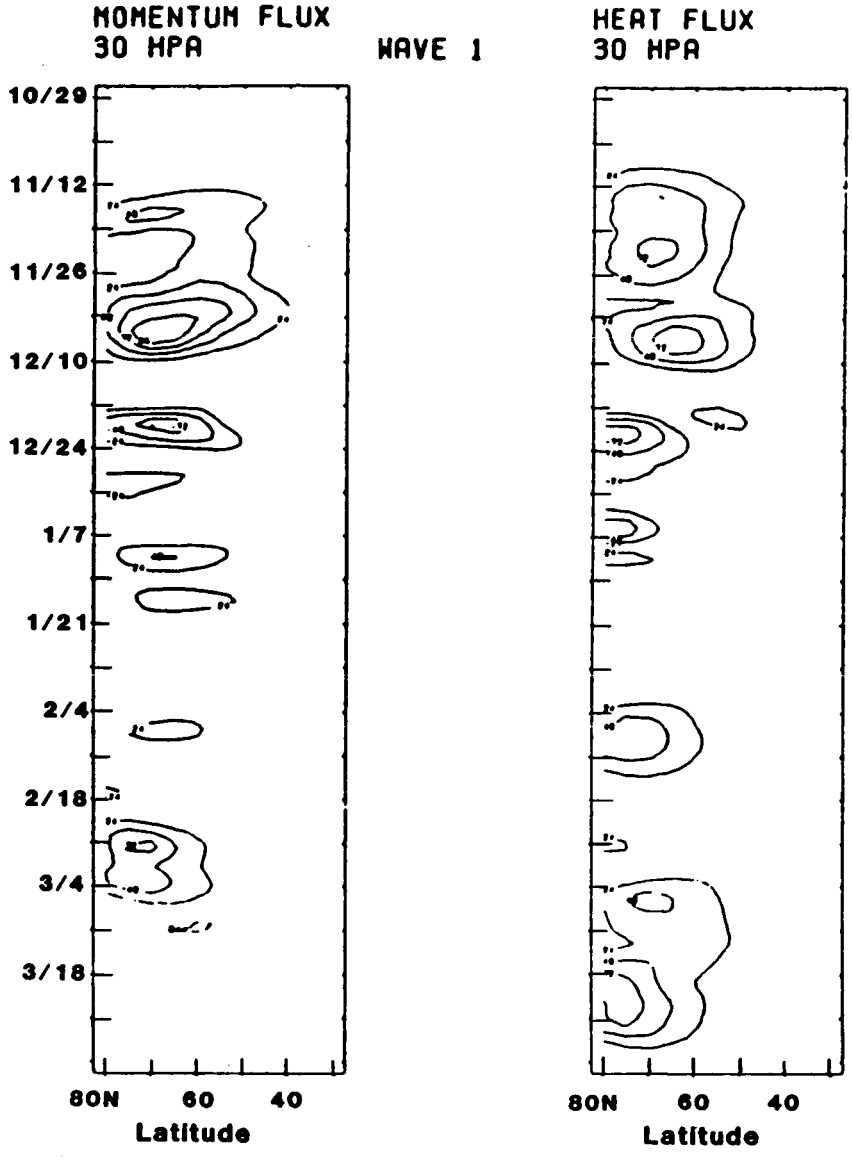


Figure 7.8. Meridional time sections from November 1984 to March 1985 of zonally averaged eddy momentum transport ($m^2/s^2$) and eddy heat transport (Km/s) by planetary wave 1. (Labitzke et al., 1985.)

# 8. TASK 7--INVESTIGATE THE CONNECTION BETWEEN THE VARIATION OF AEROSOL BACKSCATTER AND LOCAL MICROPHYSICAL CONDITIONS

## 8.1 Analysis of Data from the Airborne Lidar Flights of January 1984

An important feature of the global stratospheric aerosol climatology is the occurrence of polar stratospheric clouds (PSCs) at high latitudes in winter. These were initially detected in data from the SAM II satellite (McCormick et al., 1982) and are also visible on occasion in SAGE I and SAGE II data. A limitation of the satellite extinction measurements is the restriction of the measurement location to the sunrise and sunset boundaries. It is thus not possible to study conditions within the polar night region where temperatures are colder and theoretical analysis (Steele and Hamill, 1981), leads us to expect a greater likelihood of PSC occurrence. In January 1984, the NASA-LaRC airborne lidar system made a special mission to high northern latitudes. The purpose of this mission was

a. to make correlative measurements with the SAM II satellite,
b. to map the volcanic aerosol injected by the eruption of El Chichon in April 1982, and
c. to observe polar stratospheric clouds should arctic temperatures be low enough to permit their formation.

Following a series of correlative measurements on January 23, 1984, three flights were made to the north of Thule, Greenland, including one to the north pole. Polar stratospheric clouds were seen on all three occasions,

on one occasion extending from bout 80°N to the pole. As part of the general analysis of stratospheric aerosol properties carried out in conjunction with the analysis of SAGE II data, a detailed study has been made of the lidar data from these flights. This work has been documented in the form of a research paper which has recently been accepted by the Journal of Atmospheric Sciences for publication. A copy of the abstract of this paper is attached to this report as Appendix 3 (Kent et al., 1986).

## 9. CONCLUSIONS

A detailed study has been made of the preliminary SAGE II satellite data set, together with available associated data sets. The SAGE II data set extends from October, 1984 to May, 1985. Correlative data obtained during two measurement series made respectively on November 30, 1984 in Laramie, Wyoming, and on August 7, 1985 at Fairbanks, Alaska, have been analyzed in detail. In addition, climatological data on the stratospheric aerosol have been available from the SAGE I and SAM II satellite as well as ground-based and airborne lidar.

In general, the SAGE II data set has been found to be both internally self-consistent and in good agreement with the results of other experiments. It is clearly a data set of great potential value. During the course of the study, various anomalies and inconsistencies in the data set have been found and removed from successive editions. Some still remain, although it is anticipated that these will be removed from the next version of the data set which should have archival status. Among those errors still remaining in the current preliminary data set are (1) an altitude error in the sunrise data, (2) anomalous values at low altitudes in the 0.525 μm aerosol channel, and (3) contamination from aerosol in the water vapor channel. The latter effect is clearly decreasing as the residual aerosol from El Chichon is removed from the stratosphere. The sources of these anomalies have been identified in the data inversion procedure and their correction is currently under study.

In the course of examination of the SAGE II data, various climatological studies have been made in which the SAGE II data have been examined in the

context of other data sets. The agreement here is excellent. Detailed studies have also been made on the retrieval of the aerosol size distribution from the SAGE II multiwavelength aerosol data and its use in conjunction with the SAGE II water vapor channel to study the aerosol microphysics.

Although the current study has been made on a preliminary data set and from that aspect should not be regarded as final, the general data quality appears extremely good. Known anomalies will be corrected in the next data version which will then be suitable for general scientific use and, as such, of unique value to many atmospheric studies.

## 10. REFERENCES


Chanin, M-L., and A. Hauchecorne, 1981: Lidar observations of gravity and tidal waves in the stratosphere and mesosphere, J. Geophys. Res., 86, 9715-9721.

Chanin, M-L., and A. Hauchecorne, 1984: Possibilities of a lidar using Rayleigh scattering to sound the middle atmosphere between 30 and 100 km. Summary of the geophysical results obtained at the Observatory of Haute-Provence, 12th International Laser Radar Conference, Aix en Provence, 13-17 August 1984, Conference Abstracts, p. 221, 1983.

Chu, W. P., and M. P. McCormick, 1979: Inversion of stratospheric aerosol and gaseous constituents from spacecraft solar extinction data in the 0.38-1.0 μm wavelength region, Appl. Opt., 18, 1404-1413.

Chu, W. P.. 1986: Inversion of SAGE II measurements, presented at the 6th Conference on Atmospheric Radiation, Williamsburg, Virginia, May 13-16, 1986. (Extended Abstracts, pp. J49-J51.)

Chu, W. P., and M. P. McCormick, 1986: SAGE observations of stratospheric nitrogen dioxide, J. Geophys. Res., 91, 5465-5476.

Gmitro, J. I., and T. Vermeulen, 1964: Vapor-liquid equilibria for aqueous sulfuric acid, A.I.Ch.E. Journal, 10, 1308-1315.

Hauchecorne, A., and M-L. Chanin, 1982: A mid-latitude ground-based lidar study of stratospheric warmings and planetary wave propagation, J. Atmos. Terr. Phys., 44, 577-583.

Kent, G.S., W. Keenliside, M. C. W. Sandford, and R. W. H. Wright, 1972: Laser radar observations of atmospheric tides in the 70-100 km height region, J. Atmos. Terr. Phys., 34, 373-386.

Kent, G. S., and W. Keenliside, 1974: Laser radar observations of seasonal changes in atmospheric density in the mesosphere and lower thermosphere, J. Atmos. Sci., 31, 1409-1412.

Kent, G. S., and W. Keenliside, 1975: Laser radar observations of the $\Theta_3^{\omega,1}$ diurnal atmospheric tidal mode above Kingston, Jamaica, J. Atmos. Sci., 32, 1663-1666.

Kent, G. S., and M. P. McCormick, 1984: SAGE and SAM II measurements of global stratospheric aerosol optical depth and mass loading, J. Geophys. Res., 89, 5303-5314.

Kent, G. S., and M. P. McCormick, 1985a: Global stratospheric aerosol climatology from satellite occultation and lidar measurements, presented at the Symposium on Radiation in the Middle Atmosphere at the IAGA-IAMAP meeting in Prague, Czechoslovakia, August 5-17, 1985.

Kent, G.S., and M. P. McCormick, 1985b: Stratospheric aerosol observations following the eruption of El chichon, presented at the Workshop on Ozone Variations on Climatological Time Scales: Observations and Theory and Perturbations by UV Flux Variations and the Eruption of El Chichon, Salzburg, Austria, August 19-22, 1985.

Kent, G.S., 1986: Dispersion characteristics of volcanically injected aerosol as seen by SAGE I, SAM II, presented at the Conference on Atmospheric Radiation, Williamsburg, VA, May 13-16, 1986. (Extended Abstracts, pp. J54-55.)

Kent, G. S., L. R. Poole, and M. P. McCormick, 1986: Characteristics of arctic polar stratospheric clouds as measured by airborne lidar, J. Atmos. Sci., 43, 2149-2161, 1986.

Kent, G.S., C. R. Trepte, U. O. Farrukh, and M. P. McCormick, 1985: Variation in the stratospheric aerosol associated with the north cyclonic polar vortex as measured by the SAM II satellite sensor, J. Atmos. Sci., 42, 1536-1551.

Labitzke, K., B. Naujoket, R. Lenschow, K. Petzolet, B. Rajewski, and R. C. Wohlfart, 1985: The third winter of MAP--Dynamics, 1984/85. Beilage zur Berliner Wetterkarte, Institute for Meteorology, Free University of Berlin, July 7, 1985.

Lenoble, L., P. Prevost, and C. Brogniez, 1984: SAGE satellite observations of stratospheric aerosols from Mount St. Helens eruption: A two wavelength analysis, J. Geophys. Res., 89, 11666-11676.

Longhurst, R. S., 1964: Geometrical and Physical Optics, Longmans, London, pp. 423.

McClatchey, R. E., H. J. Bolle, and K.Ya. Kondratiev, 1980: Report of the ZAMAP Radiation Atmosphere, 33pp., WMO/ZAMAP, Geneva, 1980. (Available from Air Force Geophysics Laboratory, Hanscom AFB, MA 01731.)

McCormick, M. P., P. Hamill, T. J. Pepin, W. P. Chu, T. J. Swissler, and L. R. McMaster, 1979: Satellite studies of the stratospheric aerosol, Bull. Amer. Meteor. Soc., 60, 1038-1046.

McCormick, M. P., H. M. Steele, P. Hamill, W. P. Chu, and T. J. Swissler, 1982: Polar stratospheric cloud sightings by SAM II, J. Atmos. Sci., 39, 1387-1397.

McMaster, L. R., 1986: Stratospheric Aerosol and Gas Experiment (SAGE II), presented at the 6th Conference on Atmospheric Radiation, Williamsubrg, VA, May 13-16, 1986. (Extended Abstracts, pp. J46-J48.)

Mauldin III, L. E., N. H. Zaun, M. P. McCormick, J. H. Guy, and W. R. Vaughan, 1985: Stratospheric Aerosol and Gas Experiment II instrument: A functional description, Opt. Engr., 24, 307-312.

Philbrick, C. R., K. U. Grossmann, R. Hennig, G. Long, D. Kranhousky, D. Offernam, F. J. Schmidlin, and U. von Zahn, 1983: Adv. Space Res., 2, 121-124.

Pinnick, R. G., J. M. Rosen, and D. J. Hofmann, 1976: Stratospheric aerosol measurements III: Optical model calculations, J. Atmos. Sci., 33, 304-314.

Price, J. M., 1983: Atmospheric definition for shuttle aerodynamic investigations, J. Spacecraft, 20, 133-140.

Russell, P. B., T. J. Swissler, M. P. McCormick, W. P. Chu, J. M. Livingston, and T. J. Pepin, 1981; Satellite and correlative measurements of the stratospheric aerosol. I: An optical model for data conversions, J. Atmos. Sci., 38, 1279-1294.

Steele, H. M., and P. Hamill, 1981: Effects of temperature and humidity on the growth and optical properties of sulpheric acid-water droplets in the stratosphere, J. Aerosol Sci., 12, 517-528.

Steele, H. M., P. Hamill, M. P. McCormick, and T. J. Swissler, 1983: The formation of polar stratospheric clouds, J. Amos. Sci., 40, 2055-2067.

Wang, P.-H., G. K. Yue, A. Deepak, and R. J. Kurzeja, 1980: A model study of the diurnal variation of mesospheric O., Proceedings of the Quadrennial International Ozone Symposium, Ed. J. London, 876-883.

Wang, P.-H., M. P. McCormick, T. J. Swissler, and G. K. Yue, 1986: A study of the stratospheric aerosol size distribution utilizing preliminary data from SAGE II and correlative measurements, presented at the 6th Conference on Atmospheric Radiation, Williamsburg, VA, May 13-16, 1986. (Extended Abstracts, pp. J84-J87.)

Woodbury, G. E., and M. P. McCormick, 1983: Global distributions of cirrus clouds determined from SAGE data, Geophys. Res. Lett., 10, 1180-1183.

Woodbury, G. E., and M. P. McCormick, 1986: Zonal and geographical distributions of cirrus clouds determined from SAGE data, J. Geophys. Res., 91, 2775-2785.

Yue, G. K., and A. Deepak, 1983: Retrieval of stratospheric aerosol size distribution from atmospheric extinction of solar radiation at two wavelengths, Appl. Opt., 22, 1639-1645.

Yue, G. K., and A. Deepak, 1984: Latitudinal and altitudinal variation of size distribution of stratospheric aerosols inferred from SAGE aerosol extinction coefficient measurements at two wavelengths, Geophys. Res. Lett., 999-1002.

Yue, G. K., and A. Deepak, 1984: Latitudinal and altitudinal variation of size distribution of stratospheric aerosols inferred from SAGE aerosol extinction coefficient measurements at two wavelengths, Geophys. Res. Lett., 999-1002.

APPENDIX 1

# GLOBAL STRATOSPHERIC AEROSOL CLIMATOLOGY FROM SATELLITE OCCULTATION AND LIDAR MEASUREMENTS

by

G. S. Kent
Science and Technology Corporation, Hampton, VA 23666

and

M. P. McCormick
NASA Langley Research Center, Hampton, VA 23665

(An invited review paper presented at the Symposium on Radiation in the Middle Atmosphere at the IAGA-IAMAP Meeting in Prague, Czechoslovakia, August 5-17, 1985.)

ABSTRACT

Satellite occultation measurements (SAGE I, SAGE II, and SAM II), and the results from recent airborne lidar expeditions, have led to a greatly improved understanding of stratospheric aerosol climatology. Marked seasonal and latitudinal variations are observed, particularly in the polar winter where polar stratospheric clouds occur and the polar vortex modifies the aerosol distribution. Several volcanic eruptions since 1979 have produced major changes in the aerosol concentrations.





PRECEDING PAGE BLANK NOT FILMED

APPENDIX 2

# STRATOSPHERIC AEROSOL OBSERVATIONS FOLLOWING THE ERUPTION OF EL CHICHON

G. S. Kent

Science and Technology Corporation
Hampton, Virginia 23661

M. P. McCormick

NASA-Langley Research Center
Hampton, Virginia 23665

An invited paper presented at the Workshop on Ozone Variations on Climatological Time Scales: Observations and Theory and Perturbations by UV Flux Variations and the Eruption of El Chichon, held in Salzburg, Austria, August 19-22, 1985.

## ABSTRACT

Several eruptions of the El Chichon volcano between March 28 and April 4, 1982 produced a global enhancement of the stratospheric aerosol content which seriously affected satellite measurements of properties of the earth and its atmosphere. This enhancement, possibly the largest in the past seventy years, has since been monitored by in situ, as well as, satellite and ground-based remote sensing techniques. The injected material, at latitude 17°N and at altitudes up to 30 km, spread rapidly zonally and more slowly meridionally. Airborne lidar measurements showed that the maximum global mass loading of about $1.2 \times 10^7$ tonnes occurred 3-6 months after the eruptions. By May 1983, the aerosol was well distributed globally, with peak concentrations within a rather broad equatorial band and between 40° and 60°N and S. The altitude of the peak aerosol mixing ratio, initially at about 27 km in the equatorial zone, had decreased by 5-6 km by May 1983. Midlatitude lidar measurements showed a similar decrease, accompanied by loss of material from the stratosphere into the troposphere. Estimates of the 1/e decay time for the aerosol mass loading vary between 5 and 14 months, depending upon latitude and measurement techniques, with a northern hemisphere average of about 10 months.

APPENDIX 3

# CHARACTERISTICS OF ARCTIC POLAR STRATOSPHERIC CLOUDS AS MEASURED BY AIRBORNE LIDAR

by

G. S. Kent
Science and Technology Corporation, Hampton, VA 23666

and
L. R. Poole and M. P. McCormick
Atmospheric Sciences Division
NASA-Langley Research Center, Hampton, VA 23665

(Published in the Journal of the Atmospheric Sciences, October 1986)

ABSTRACT

Airborne lidar measurements of backscattering at 0.6943 um from polar stratospheric clouds, made in January 1984, are reported. The clouds, whose altitudes and geographical locations coincided with ambient atmospheric temperatures below about 193 K, were observed to cover a greater area of the polar cap than had previously been apparent from satellite measurements. They were seen on three separate flights north of Thule, Greenland (76.5°N, 68.7°W), on one occasion extending continuously from approximately 80°N to the North Pole. Pronounced layering of the clouds was observed and the maximum backscatter enhancement, relative to that from the background aerosol, was between 100 and 200. These values occurred at an altitude of about 20 km, close to the region of minimum stratospheric temperature. Depolarization of the order of 20-50% in the backscattered signal was measured, in support of the hypothesis that the aerosols forming the clouds are frozen. Comparison of the experimentally determined backscattering-temperature relationship with a theoretical model, based on a volcanic aerosol and using best available estimates for water vapor concentration, shows good agreement at the 100 mb and 70 mb pressure levels. A small systematic error at the 50 mb and 30 mb levels may be due to inaccurate characterization of the temperature field at these altitudes and locations.

## Standard Bibliographic Page

| 1. Report No. | 2. Government Accession No. | 3. Recipient's Catalog No. |
|---|---|---|
| NASA CR-178189 | | |

| 4. Title and Subtitle | 5. Report Date |
|---|---|
| SAGE II Satellite Data Set Validation | November 1986 |
| | 6. Performing Organization Code |

| 7. Author(s) | 8. Performing Organization Report No. |
|---|---|
| Geoffrey S. Kent<br>Pi-Huan Wang | STC TR 2108 |

| 9. Performing Organization Name and Address | 10. Work Unit No. |
|---|---|
| Science and Technology Corporation<br>101 Research Drive<br>Hampton, Virginia 23666 | 11. Contract or Grant No.<br>NAS1-17959 |

| 12. Sponsoring Agency Name and Address | 13. Type of Report and Period Covered |
|---|---|
| National Aeronautics and Space Administration<br>Washington, DC 20546 | Contractor Report |
| | 14. Sponsoring Agency Code |

15. Supplementary Notes

Technical Monitor: Leonard R. McMaster, NASA Langley Research Center, Hampton, Virginia.
Final Report

16. Abstract

This report presents the results of a validation study of data obtained by the Stratospheric Aerosol and Gas Experiment II Satellite Experiment (SAGE II). Preliminary SAGE II data have been available for the period October, 1984 to May, 1985. In addition, the results of two correlative experimental measurement series have been studied in detail, as well as climatological data obtained by other techniques, including ground-based and airborne lidar. The study shows the SAGE II data to be of great potential value to studies of the microphysics of stratospheric aerosols, the chemistry of trace gases and stratospheric dynamics. A small number of unidentified errors in the current preliminary data set are described. These will be removed from the next version of the data set which is anticipated to be of archival quality.

| 17. Key Words (Suggested by Authors(s)) | 18. Distribution Statement |
|---|---|
| SAGE II<br>Satellite radiometry<br>Validation<br>Stratosphere<br>Aerosols<br>Ozone | Unclassified - Unlimited<br><br>Subject Category 46 |

| 19. Security Classif.(of this report) | 20. Security Classif.(of this page) | 21. No. of Pages | 22. Price |
|---|---|---|---|
| Unclassified | Unclassified | 138 | A07 |

For sale by the National Technical Information Service, Springfield, Virginia 22161